DESIGN AND EVALUATION OF A TRANSCUTANEOUS ENERGY TRANSFER SYSTEM

by

Chad Bossetti

Department of Biomedical Engineering
Duke University

Date: _____

Approved:

_____
Patrick D. Wolf, Supervisor

_____
Warren M. Grill

_____
Craig S. Henriquez

_____
Steven A. Cummer

_____
Dennis A. Turner

Dissertation submitted in partial fulfillment of the
requirements for the degree of Doctor of Philosophy
in the Department of Biomedical Engineering
in the Graduate School of
Duke University

2009

ABSTRACT

DESIGN AND EVALUATION OF A TRANSCUTANEOUS ENERGY TRANSFER SYSTEM

by

Chad Bossetti

Department of Biomedical Engineering
Duke University

Date: _____

Approved:

_____
Patrick D. Wolf, Supervisor

_____
Warren M. Grill

_____
Craig S. Henriquez

_____
Steven A. Cummer

_____
Dennis A. Turner

An abstract of a dissertation submitted in partial fulfillment of the
requirements for the degree of Doctor of Philosophy
in the Department of Biomedical Engineering
in the Graduate School of
Duke University

2009

Abstract

A clinically viable brain-machine interface (BMI) requires a fully-implanted wireless neural acquisition system to limit the impediments of percutaneous connections. For an implanted system with an appreciable telemetry range, and where significant neural signal processing is performed continuously, a major obstacle for clinical application is the need for a power source. Existing battery technology and wireless power delivery systems have not addressed the need for a mid-range power supply, capable of 1-3 W delivery, that limits both induced noise and temperature rise. These factors are crucial for the succesful operation of a fully-implanted neural acquisition system. This work seeks to fill this void, and presents both a wireless power solution suitable for a neural recording device, and a system capable of real time monitoring of tissue temperature rise.

During this research, a 2 W transcutaneous energy transfer system (TETS) was designed, built and tested. The TETS was designed specifically for a 96-channel implanted neural data acquisition system, which requires continuous power. The major design constraints were tolerance to coil misalignment, low induced noise, and reasonable efficiency. The design of the primary circuit consists of an H-bridge switching network driving a planar spiral Litz wire primary coil. The primary also incoporates a novel circuit for detecting the presence of the secondary. The implanted secondary components include a complimentary planar spiral coil connected to a voltage doubling rectifier. The key approach to mitigating axial coil misalignments was the use of step-down switching regulators in the secondary. With this approach, link efficiency remained nearly constant at 40%, for axial coil displacements of up to 2 cm.

Noise in the recorded neural signals was minimized using two techniques. First, the 250 kHz operating frequency of the system was tuned, such that the aliased harmonics of the switching frequency lay above the bandwidth of the amplifier used for neural recording. The second approach was to limit the impact of induced displacement currents in the body by physically separating the recording front end from the power supply components. A large titanium enclosure was used to house some of the secondary electronics, and provided a low impedance return path for further reduction of current-induced noise.

Limiting the temperature rise of internal components was also a critical design constraint. The need for real time temperature information led to the design of a six channel temperature measurement system and incorporation of the temperature data into the acquisition system data transmission scheme. This system consisted of bead thermistor temperature transducers, and an off-the-shelf microcontroller with a built-in instrumentation amplifier.

The TETS and temperature system was fully tested in an ovine model during several acute studies. Recorded temperature rise was limited to approximately 5.5°C when the system was implanted at an adequate depth in muscle. The TETS was able to successfully power the 2 W neural acquisition system during a data processing task. Received rectified voltage in the secondary ranged from 14.86 V to 20.2 V, while link efficiency remained virtually constant. Acquired neural data was examined for TETS switching noise. The measured RMS noise increased by less than 1 μV, averaged over several experiments. These results demonstrate the first mid-range TETS solution for powering a fully implanted neural acquisition system.

Contents

List of Figures

List of Tables

Acknowledgements

As I reflect on my career as a graduate student, I am reminded of the phrase "It takes a village..." My expectations upon entering grad school were that it was a place of intellectual solitude; where every academic challenge must be overcome by the individual, and that it was the individual who made great contributions to his field. I now know that it take a relatively large population of quality people to raise a good researcher. That it is collaboration that allows contributions to be made at all. It is now that I would like to thank the many talented individuals with whom I have had the pleasure of working with and learning from. It is these individuals, more than I, who have produced this contribution.

I begin with my advisor, Dr. Patrick Wolf, for whom I cannot find the words to fully express the depths of my gratitude. Never have I encountered someone so fluent in the language of engineering and experimental design. Dr. Wolf has a natural ability to find the root of a problem and conceptualize solutions to it; he does so with uncanny (if not annoying) speed. Although I may not posses this trait, I have learned so much about how to approach engineering problem solving because of him. I have no doubt that my abilities as an engineer have improved by an order of magnitude having studied under him. On a personal level, after the birth of our first, then second, daughter, I found myself questioning whether I would be able to complete this journey with the added duties of fatherhood. I have no doubt that had I been in any other lab, I may well have left research for the security of employment. With Dr. Wolf having a similar experience in his early research career, I felt motivated to continue in my own research (I would sometimes tell myself, "Dr. Wolf did it with three"). His understanding and words of encouragement meant so much to me. I will never forget the support he gave me. I cannot thank him enough.

I am also thankful for having such a supportive committee. Thank you Drs. Craig Henriquez, Warren Grill, Steve Cummer, and Dennis Turner. I greatly appreciate your guidance, and the use of your time, during my studies at Duke.

Turning to my lab mates, I would first like to thank those grad student mentors who have preceded me, and who have given me so much thoughtful advice on a number levels. Dr. Iyad Obeid was a strong influence in my early grad school days. I am thankful to have had him as a friend and mentor, and I continue to admire and respect him. Drs. Amy Goodman, Kit Yee Auyeung, Debbie Won, Ninita Brown, and Himanshu Arora made life in the lab enjoyable. Thank you all.

I owe a huge debt of gratitude to those I worked with during the TETS design and on the 96-channel system. I must begin by offering my sincerest thanks to Tom Jochum. He is my all-time analog consigliere. Tom has a level of circuit knowledge that may be unmatched. He has been so gracious in taking time out of his two jobs to answer my endless array of questions. I really appreciate his generosity in helping me understand circuit parasitics, and for being willing to suggest and talk about a variety of circuit topologies (I ended up falling in love with the H-bridge topology after he suggested it as a candidate). I also appreciate our discussions about research, and the nature of engineering and medicine. He shaped my thinking in a number of ways, and I greatly appreciate it.

I also owe a huge thank you to Steve Callender. I want to adopt Steve as my life coach. No one made life in the lab brighter. Whether it be with a positive attitude, a perpetual smile, a god-awful engineering joke, or his musical proclivities, Steve was always a pleasure to be around. We used to say that you knew Steve was having a bad day because instead of whistling a cheery song, he would be whistling an angry song. From a technical stand point, Steve is an awesome utility engineer. He knows everything. He knows digital, he knows analog, he knows how to use *any* tool (many

of which I'd never heard of), he can do board layout, he can work on headstages, he knows about glue, he can show you how to use just about any feature on a logic analyzer. It goes on and on. Without question, our group's progress towards a fully-implanted neural acquisition system would have been significantly hampered had it not been for Steve. He helped me in so many ways, and I will always be grateful for it.

Finally, Dr. Michael Rizk. What can I say, you will never meet a nicer, more thoughtful intellect than Michael. Pound-for-pound he is one of the best engineers in the lab. His computer and software engineering skills are amazing. At some point, he has helped me with just about every piece of software I've used at Duke. Whether it be LaTeX, writing firmware for the temperature system, or Linux questions, he has always graciously accepted my requests for help. As one of the remaining grad students in the office, he also bore the brunt of my recurring chattiness, as well as my complaining. I'm sure his productivity increased markedly after my departure. I'm so thankful to have had him as a colleague during my time in the lab.

Apart from my fellow grad students, I would also like to thank Ned Danieley. Ned may have one of the toughest jobs around, keeping the network running while the rest of us try to break it. His email reminders about getting rid of big, unused files always brought a defiant smile to my face (and a head shake). I promise Ned, I'll finally clear out my aiki account. I would also like to thank Ellen Dixon-Tulloch for her help with the animal studies. Most of the time it seemed like she was the hardest working person in the OR. I can't imagine what those experiments would have been like without her in the room. Thank you Ellen.

I'm not done yet, we're almost there. I'd also like to thank the many people outside of the lab who made our time in North Carolina enjoyable. We definitely owe our sanity to the Harrises, the Duffys, and the Birdnos. It was great hanging

out with everyone and having our kids share this young part of their lives together. Thank you. I also owe a big thanks to Joe Tulleners. Our five hour political diatribes always provided a needed fix for my obsession with politics. Talking with Joe was always a highlight for me (and it remains so today).

And at last, I cannot conclude without expressing my sincerest appreciation to my and Charity's families. My sister, Tina, has always been an important figure to me on so many levels. I appreciated her detours to North Carolina, and our conversations. Likewise, I would like to thank my sister Teresa and her family for their words of encouragement. Charity's sister Kimberly was also very supportive, and I appreciated getting to see and hang out with her during her visits out East. I would like to thank my parents, Connie and Tom Bossetti, and my mother, Carol, for their constant love and support (and patience). Charity's parents, Michele and Gerritt Dunn have been incredible in the level they've supported us. I am so appreciative of their thoughts, prayers, and well wishes.

I also want to express my solemn appreciation to the members of our family who are no longer with us. In our waning weeks at Duke, our dog Franko passed away. Franko was a loyal friend, who had been with us for 11 years. We all miss his presence in our home. During my first year of grad school, Charity's father, Roy, passed away. This shocking loss was a sober reminder about the importance of living each day to the fullest. I'm thankful to have known him. Later in my career my grandmother, Norma, passed away. She was one of the most important people to me, and losing her was an utterly devastating event in my life. I would give anything to be able to share this accomplishment with her. I love and miss her so very much.

I also want to thank my daughters Madison and Elliott. They are an absolute joy, and we are so grateful that they are a part of our lives. I hope someday they read these pages and find them inspiring, if even in some small way, in their own lives.

They should know that they have inspired me to work hard every single day, and that I will always love them. And finally, this work would not have been possible had it not been for my loving wife, Charity. Her encouragement never wavered. She was a constant source of optimism throughout this work. She may have single-handedly willed this research to completion through her steadfast support. I appreciate what she sacrificed for me to complete this work. I love her very much.

Chapter 1

Introduction

A brain-machine interface (BMI) maps recorded neural signals into a set of commands for controlling a motorized or computer-based prosthesis. The goal of a BMI is to restore lost motor function to patients suffering from amputation, paralysis, or other motor-neural impairment. Recording techniques like EEG and ECOG have recently been shown to provide a basic means of extracting the neural information required by a BMI [1, 2]. However, a very common approach for collecting neural data remains recording from individual neurons at the cortical level. Acquiring and processing cortical neural data requires a wide array of electronics, including electrode arrays, analog amplifiers and filters, analog-to-digital converters, and several layers of digital signal processing [3, 4, 5]. One of the most widely cited limitations for chronic clinical use of existing cortical BMI technology in humans, is the percutaneous connection required by the electronics [6, 7, 8]. This connection significantly increases the risk of infection and reduces patient mobility.

To address this limitation, a fully-implanted, 96-channel wireless neural data acquisition system has been developed. This system is capable of amplifying, digitizing, and processing the acquired neural data, then transmitting it out of the body [9]. A major obstacle to the successful development of this wireless acquisition system was the availability of electrical power. As designed, the system requires approximately 2 W of continuous power. This requirement presents a substantial challenge to both battery-based power supplies commonly used in other implanted medical devices, and to existing wireless power supply techniques.

The research outlined in this dissertation presents a new class of transcutaneous

energy transfer system (TETS) for wirelessly powering the 96-channel acquisition system. The concept of using a TETS to power a medical implant is not new. However, a mid-range solution for providing 1-3 W has not been previously described. Before we present this solution, we first discuss why battery technology is inadequate for this application. We then review the major contributions of previous TETS research, and cover the limitations of existing TETS designs. Next, we outline the specific challenges that apply uniquely to 1-3 W neural recording systems. Finally, we briefly present the 96-channel system for which the TETS was designed.

1.1 Implantable Batteries

1.1.1 Primary Cells

A primary cell is a battery designed for a single discharge cycle. It is not designed to be recharged. Although a wide variety of battery chemistries are available, the most common implanted batteries are lithium-based. This particular chemistry is so widely used because high energy densities can be obtained. As of this writing, Wilson Greatbatch's QMR technology, and Quallion's CFx technology, have both achieved an energy density of approximately 1050 Wh/L [10, 11], the greatest on the market. If this technology were to be used for the 2 W neural acquisition system, a 1 L battery operated for 8 h per day would last for a little more than 2 months. Quite obviously, a primary cell constructed from even the best technology cannot support the power demands of the implanted system in a realistic application.

1.1.2 Secondary Cells

A secondary cell is a battery designed to be repeatably charged and discharged. Rechargeable battery technology generally has a unique set of limitations when compared to primary cell technology. The energy density tends to be around half that

of primary cells. As a result, the capacity is limited to around 200 mAh or less, in currently available batteries [12, 13]. A 2 W system operated from 3-5 V requires several hundred milliamps of continuous current. With this battery capacity, a system could operate for less than approximately 1 h before needing to be recharged. Considering the application, a 1 h duty cycle would be inadequate.

However, the eventual use of secondary cells in this application should not be completely dismissed. Because these cells can be recharged more than 1000 times, the longevity problem presented by primary cells is potentially removed. If rechargeable technology were improved or the power requirement reduced such that the battery would only need to be recharged every day or every other day, such a system could last for years.

If contemporary rechargeable technology was found adequate, a method for rapid wireless charging of high capacity batteries does not currently exist. What is interesting about the general use of batteries in the implanted medical device field, is that while they have been used in this application for decades, little research has been published on wireless recharging techniques for secondary cells [14, 15]. To understand the limitations involved, the basic approach to battery charging must first be understood. A good primer on the subject is available in [16, 17, 18], and is summarized in the following section.

Battery Charging Principles

The most general rule for charging a battery is to supply constant current to it at a rate of 0.1C, where C is the capacity of the battery in mAh. So a 1000 mAh battery would be charged at 100 mA, following the 0.1C rule. This method is referred to as slow charging, and theoretically requires at least 10 hours to fully charge the battery. Again, whether a 10 h charge time is practical for a clinical device depends on the

application.

Another technique for charging batteries is fast charging, where charge times are less than 3 h. This charge time is much more practical for an implanted device application. The ability to fast charge a battery depends very much on the chemistry of the battery. Most common technologies (e.g., NiMH or Li-Ion) can be charged at rates greater than 1C. In this case, the limiting factor is not the ability of the battery to be charged quickly, it is the ability of a wireless power supply to provide adequate current, and the requirement that the temperature increase of the implanted recharging circuitry remain within established limits. As will be discussed in the sections below, a need exists for a supply capable of sourcing the levels of current that would be sufficient to wirelessly recharge a secondary cell.

1.2 Introduction to Transcutaneous Energy Transfer

A system capable of wireless power delivery is now commonly referred to as a transcutaneous energy transfer system (TETS). This method allows an implanted system to be continually powered, without the constraints presented by implanted batteries. A basic block diagram of a TETS is shown in figure 1.1.

Although TETS design can be quite complex, the principles behind this power delivery method are easy to understand. A DC source provides power to an oscillator, which energizes a primary coil. Magnetic flux is linked through the implanted secondary coil, which is energized. The induced current and voltage are then modified as needed by a rectifier and regulator, to provide the particular power requirements of the implanted device. In nearly every practical TETS application, the primary coil is worn against the skin, above the implanted secondary coil. Depending on the design, the secondary coil will be implanted anywhere from several millimeters to

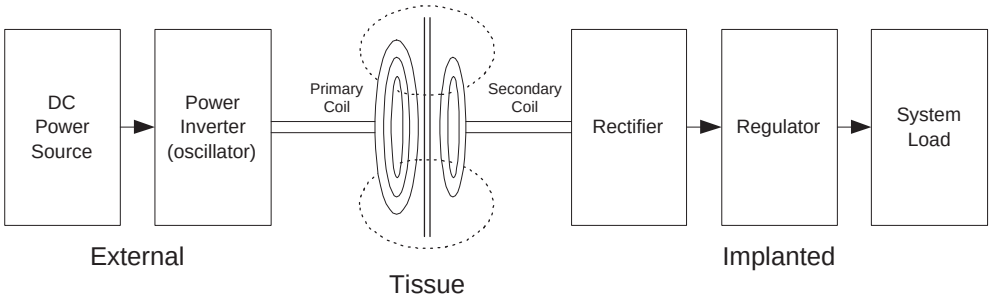

Figure 1.1: Basic block diagram of the common subsystems of a transcutaneous energy transfer system (TETS) subsystems. A DC source provides power to an oscillator, which energizes a primary coil. Magnetic flux is linked through the implanted secondary coil, which is energized. The induced current and voltage are then modified as needed by a rectifier and regulator, to provide the particular power requirements of the implanted device.

several centimeters beneath the surface of the skin. Although the coils are not linked through a fixed common core, and although they can become displaced during movement by the test subject, the two coils form a loosely-coupled transformer. Thus, the terms "primary" and "secondary" are carried over from transformer theory.

1.3 TETS History and Utility

As indicated above, the concept of inductively powered medical devices, itself, is not new. This area of biomedical research has been established for decades, with contributions made by a number of research groups, and for a wide variety of implantable systems. While TETS were originally conceived as a method for powering systems with continuous high-power demands, they have since become the preferred method for powering a range of fully-implanted, low-power medical devices. This section discusses both the high-power ($\sim$ 10W) and low-power ($\leq$ 100mW) solutions that have been presented in the literature. What is conspicuously absent from the literature is a mid-range TETS solution for providing approximately 1-3 W to a neural acquisition

system. Although it's tempting to believe that if a TETS solution exists for a 10 W system, then surely one can be engineered for a mid-range application. Indeed, some of the design principles are similar. But as will be shown, there are considerations, such as noise and temperature, that are not major factors in high-power TETS design.

1.3.1 Cardiac Devices

The advent of the total artificial heart is what first led researchers to consider wireless power transfer. Toward that end, in 1960 the first TETS was experimentally evaluated in a canine model [19]. This system consisted of the basic components described in figure 1.1, but rather than being fully-implanted, percutaneous wires were used to bring the delivered load back out of the animal. This configuration allowed the researchers to vary the load for testing purposes (and was a fine methodology, given the technology at the time). The group was able to demonstrate power transfers of 50 W and 69 W, and they were able to drive a rotary pump capable of providing the circulatory output for a small test subject. This same research group later reported power transfers of up to 1 kW [20]. However, because the transferred power was dissipated outside the body, the impact of temperature rise was not fully apparent. In the later study, the researchers did measure a temperature rise of approximately 3.1°C at the surface of the implanted coil. Calculations and experimental methods revealed that this rise resulted from secondary coil losses of approximately 5 W. As will be shown later in this chapter, more recent studies have demonstrated the effects of tissue temperature rise, and have proposed power density limits to avoid tissue damage. Such considerations were not fully addressed by these early TETS studies.

Since the development of this first system, this high power application has continued to be a major research focus for TETS development. Reported results from

other experimental systems include the successful transmission of 20-25 W [21, 22], 12-48 W [23], and up to 60 W of power [24]. In addition, electrohydraulic ventricular assist devices (VAD) have been powered by TETS, with systems transmitting 5-70 W [25, 26, 27, 28]. The research group at The Pennsylvania State University [27, 28, 29] have also tested both VAD and total artificial heart (TAH) systems *in vivo*, with an average implant power consumption of approximately 15 W. Again, temperature rise was not a major factor in these designs.

1.3.2 Implanted Stimulators

Another major application of TETS is in low-power, implanted electrical stimulators. TETS have seen increased clinical utilization in functional electrical stimulation (FES) and pain control devices, in addition to being used for battery recharging in hybrid versions of these prostheses [Medtronic, Inc., Minneapolis, MN], [30]. By far, The most prolific clinical device application of TETS is in cochlear implants. These devices have been implanted in more than 60,000 patients worldwide since the 1980's, and have employed inductively coupled power delivery techniques since the early 1990's [31].

1.3.3 Implanted Neural Recording Devices

Very few neural recording systems have encorporated a wireless power feature. Several low-power systems (requiring no more than 100 mW) have been reported, but results are nebulous and significant work remains [32, 33, 34]. Two of the more competent systems that have been developed include the Michigan Probe [8] and the wireless smart implant reported in [35]. Both devices include more than 100 channels, and require less than 100 mW. Operating currents are limited to less than 5 mA. However, neither of these devices have been demonstrated *in vivo*.

One of the more promising systems for wireless neural data acquisition was recently described in [6]. Here, a 100-channel, single chip solution that integrates all implanted components on one IC was tested with both prerecorded and real-time neural data. The system consumed approximately 13.5 mW, and was able to extract neural action potentials and transmit them off-chip at a rate of 330 kbps. Alternatively, the system could transmit the raw neural data from a single digitized channel. While this performance is impressive, interference issues plagued the system. Digital crosstalk was a significant hurdle, requiring another revision of the full IC. More importantly, the TETS portion of the design could not be tested with the configuration described in the paper. Thus, the effects of this major source of interference remain unknown.

To summarize, of the few recording systems that use an inductive link for continuous power, all are low power systems. In addition, none of the above systems have been successfully demonstrated in a realistic test environment. To date, a high channel-count neural acquisition system requiring spike processing, bi-directional telemetry, and power levels in excess of 1 W has not been successfully developed.

1.4 Heating Mechanisms

A major consideration for the design of any active, implantable medical device is the potential of the device to heat tissue during operation. Temperature rise in tissue has been widely studied, and is known to cause cell death if not limited. There are several heating mechanisms associated with the operation of a wireless implanted device [36]. This section outlines these mechanisms, and presents the specific limitations associated with TETS operation.

1.4.1 Electronic Heating

By far, the biggest contributor to tissue temperature rise is the heat generated by the device electronics. Because of the health risks associated with implanted devices, in general, the Food and Drug Administration (FDA) regulates the US industry by evaluating devices against nationally recognized safety standards. One particular standards organization that is commonly cited by the FDA is the International Organization for Standardization (ISO). According to ISO 14708-1 part 17, the outer surface of any part of an implantable device should not exceed 2°C above the normal body temperature of 37°C, as a result of normal operation or any single fault condition [37].

One question that may arise during the design of the implanted electronics is: how can the designer tell whether device power consumption will bring about a temperature rise that exceeds the FDA mandate? This question was addressed by a series of in-depth studies published by a research group at Case Western Reserve University [38, 39, 40, 41, 42]. The authors presented key findings about how tissue responds to temperature rise, and provided experimental data that established a link between power consumption and surface temperature increases. These studies were carried out by implanting a controlled heating unit in a bovine animal model, and applying specific amounts of power to heat the tissue. Both temperature and power density were recorded in dozens of animals over a period of weeks to months. For muscle, the results indicated that power densities of 60 mW/cm^2 and 80 mW/cm^2 increased the baseline tissue temperature by 4-7°C. Absolute temperatures ranged from 43-46°C, with necrosis occurring at the upper end of this range. For a power density of 40 mW/cm^2, the tissue temperature increase was limited to a range of 2-3°C, with absolute temperatures remaining below 42°C. These data points provide insight into how to select an appropriately-sized enclosure, based on expected device

power consumption.

1.4.2 Eddy Current Heating

The gold standard for durable implanted medical device packaging is titanium alloy. One risk in using conductive material as an enclosure is that magnetic fields can induce circular, or eddy, currents in the metal as they pass through. These currents would result in increased heating, through I^2R losses. This effect has been studied specifically for the case of TETS coils in close proximity to such an enclosure [43]. In the study, the primary coil had an inner diameter of 4.5 cm; the secondary coil had an inner diameter of around 2 cm; the TETS operating frequency was approximately 160 kHz; and the peak current on the primary was on the order of 10 A. As we will see in chapter 2, these physical parameters are remarkably similar to those of the system designed during this research.

A key finding of the study was that when the primary and secondary coils were brought within approximately 4-5 cm of the conductive sheets (aluminum and titanium alloy), the equivalent series resistance (ESR) of the coils increased by around 10 mΩ. The effect was less pronounced for thicker sheets. From basic transformer theory, the increase in resistance represents the impedance of the sheets being reflected into the coils. Any power consumed by this resistance, would be dissipated in the sheet. For a peak primary current on the order of 10 A, a 10 mΩ increase in the ESR of the primary would result in an additional power loss of 1 W. As discussed in the previous section, even small increases in power density can cause potentially harmful increases in temperature.

An important conclusion from the above study, was that when the coils were kept more than 12 cm from the conductive enclosure, increases in ESR were negligible. In a human application, maintaining this distance may not be physically possible,

depending on the patient. Thus, the potential exists to heat the tissue.

1.4.3 Electromagnetic Heating

Tissue temperature can also increase through direct absorption of electromagnetic energy. A common measure of absorption is the specific absorption rate (SAR). The SAR is expressed in units of energy per unit time per unit mass, or W/kg. It is formally defined as [44]:

$$SAR = \frac{d}{dt}\left(\frac{dW}{dm}\right) = \frac{d}{dt}\left(\frac{dW}{\rho dV}\right) \tag{1.1}$$

This description provides a qualitative understanding of SAR, but does facilitate measurement or calculation. It is more helpful to write the above expressions in terms of either temperature rise [45], or the material parameters and induced electric field [46, 47].

$$SAR = \left(\frac{dT}{dt}\right) c = \frac{\sigma |E|^2}{\rho} \ \text{ W/kg} \tag{1.2}$$

Where c is the specific heat of the tissue, σ is the electrical conductivity, and ρ is the density. Values for these parameters are given by [48].

As in the case for the heated surface, safety standards have been developed for electromagnetic heating. Rather than the FDA, the Federal Communications Commission (FCC) regulates exposure to electromagnetic energy radiation. At present, there is no federally mandated safety standard for RF exposure. However, the FCC has relied extensively on the Institute of Electrical and Electronics Engineers (IEEE), the American National Standards Institute (ANSI), other radiation protection organizations, and other federal regulatory bodies for determining appropriate guidelines.

While the IEEE outlines maximum permissible exposures for frequencies as low as 3kHz, the FCC has implemented guidelines for frequencies greater than 300kHz. According to IEEE Std C95.1 and the FCC, exposure should be limited to an electric field strength of 614 V/m for frequencies up to 1.34 Mhz. The magnetic field exposure should be limited to 163 A/m up to 100 kHz, 16.3/f(MHz) A/m from 100-300 kHz, and 1.63 A/m up to 1.34 MHz. These field strengths are the spatially averaged rms values, where the average is taken over the vertical cross section of the human body. The SAR should be limited to 0.08 W/kg, also averaged over the whole body. These guidelines pertain to the general population, receiving whole-body exposure.

For partial-body exposure, the recommendations are somewhat relaxed. The spatial peak SAR should not exceed 1.6 W/kg, as averaged over any 1 g of tissue. For frequencies up to 300 MHz, the peak value of the electric and magnetic fields are limited to 20 times the square of the rms values listed above for whole-body exposure [44, 49].

1.4.4 Summary of Temperature Constraints

In this section, several mechanisms for heating the tissue were described, and established limits on power density and temperature rise were discussed. The most serious constraint on the operation of a fully implanted 2 W neural acquisition system is that the electronics may heat the biocompatible packaging. The enclosure that houses the electronics must have enough surface area to keep the power density low, but must be small enough to safely implant. Because titanium alloy is the preferred packaging solution, there is the additional risk that eddy currents may develop and further heat the enclosure. This risk may vary from patient to patient, depending on surgical constraints. In order to determine whether the 2 W system can be operated for prolonged periods, a technique for monitoring temperature *in vivo* is needed. This

method should be an integral part of the implanted system, so that this important physiologic signal can be monitored, regardless of the particular application or test subject.

1.5 Switching Topologies

In addition to the noise and temperature challenges discussed so far, design of the TETS primary circuit also presents a challenge. In this section, several of the most commonly used primary coil drivers are discussed, and the fundamental operating principles of each is briefly described. It should be noted that all of the switching topologies discussed here are classified as power inverters. The job of an inverter is to convert a DC power source into an AC power source, so that a transformer can alter the source's voltage and current characteristics. The AC power received by the transformer secondary is then converted back into DC, at new voltage and current levels that are appropriate for downstream circuitry.

1.5.1 Class E

The most popular experimental method for energizing the primary coil is the class-E amplifier. This class of amplifiers was invented in 1975, by the Sokals [50]; detailed mathematical analysis was later provided in [51]. Although there are a number of circuit topologies that can be categorized as members of this class, the basic circuit consists of a single power transistor that switches current through an LC network. A number of variations of the base circuit are shown in are shown in [52, 53, 54, 21, 22, 55, 56]. To be categorized as members of the class-E amplifier family, each of these circuits exhibits the following three characteristics [53, 50]:

1. The active device drops minimal (preferably zero) voltage while current is flowing through it.

2. The active device is switched on when the voltage across it is zero, and switched off when the current through it is zero.

3. The active device must switch fast enough to minimize the time when there is simultaneous existence of current through the device and significant voltage across it.

Essentially, these characteristics are strictly focused on minimizing switching losses. Experimental systems employing this technique include the Michigan array [8], the BION system [30], the wireless endoscope [57], and a number of other recording and stimulation devices [34, 32, 58].

One reason the class-E amplifier is utilized so frequently is because of its high efficiency. Theoretically, this topology can achieve 100% efficiency. When the effects of parasitic components are taken into account, the efficiency has been reported to be as high as 80% [52]. This range of efficiencies can be alluring, especially to the designer of low-power, implanted medical devices. However, there are several reasons why the class-E switching topology may not be the best choice for driving the primary coil.

First, efficiency is an important factor in any application where portability is required. For systems whose implanted components require no more than 100-200 mW, such a device could be supplied by an external battery that is quite small, or easily concealed. A cochlear implant is a good example. In applications with power demands on the order of several watts, continuous operation requires batteries that, while still portable, are substantial in size and mass. The ability of the patient to easily conceal such a supply is of secondary importance. An inductive link with even a reasonable efficiency (of say 30-50%) would not significantly alter the physicality of the required batteries.

Another important consideration is the need for a back-telemetry scheme for tuning the received voltage in the secondary. Because linear series regulators are used to supply the implanted electronics, the received voltage must be kept just above the dropout voltage of the regulator to avoid wasting significant power. To accomplish this task, a voltage reading is taken in the secondary and fed back to the primary, where the information is used to adjust the input DC voltage. All of the systems mentioned above require such a feedback mechanism to achieve high efficiency. One of the more telling papers written about a successful class-E design shows that without the feedback channel, the efficiency is cut by nearly 50% [56]. What is also revealed by this study is the complexity involved in adding a low bandwidth telemetry channel for providing this feedback to the primary switching circuit. All designs use some form of load shift keying (LSK), in which information is encoded by briefly shorting the secondary load. This temporary short is sensed in the primary, where special circuitry is used for decoding. What makes this approach challenging for the class-E amplifier is its sensitivity to rapid load variations. In fact, a special control system must be designed to maintain amplifier stability during telemetry operation [56]. If stability can be maintained, the designer is rewarded with a bandwidth on the order of 100 kbps. Considering these challenges, the class-E circuit topology was not chosen for this research.

1.5.2 Class-D with Stagger Tuning

In contrast to the class-E amplifier, the class-D inductive link has not gained broad acceptance in implanted applications. A class-D amplifier consists of a pulse width modulator, a power transistor half-bridge, and a low pass filter. What is most innovative about the use of the class-D topology, and the reason it is briefly mentioned here, is the concept of combining it with stagger tuning to provide increased tolerance

to coil displacements. This design approach was introduced by Galbraith, Soma, and White in a pair of papers [59, 60]. It consists of choosing an operating frequency and coil design using the techniques described in [60]. This design is then integrated with stagger tuning [59]. In stagger tuning, a capacitor is used to cancel the leakage inductance in the secondary at a particular coupling factor. (The coupling factor is affected by the coil separation, so the LC pole also changes with coil separation.) Another capacitor is used in the primary to cancel the leakage inductance of the primary coil at a different coupling factor. The LC poles are chosen so that one of the poles is below the operating frequency, and the other is above it. As the coils become displaced, either the primary or secondary pole moves towards a more favorable operating frequency. In this fashion, the received voltage stays relatively constant during coil displacements, and the efficiency is roughly maintained. A wider transmission bandwidth is also supported by this link because its poles are spread across the spectrum.

Although more efficient, a class-E amplifier cannot be used to drive such an arrangement because it is very sensitive to the load variation. Since the primary LC network is not switched at resonance, class-E operation cannot be maintained. On the other hand, a class-D amplifier can be used because its operation does not require primary resonance. This topology is capable of driving resistive, capacitive, or inductive loads, and its operation can handle the load variations associated with the stagger tuned network.

To summarize, the class-D, stagger tuned link has the distinct advantage of having a wide bandwidth (up to 1 Mbps) for transmitting data into the implant [59]. Like the class-E, it is also able to maintain a relatively uniform voltage transfer characteristic over variable coil separations. However, there are several disadvantages that may explain why this topology has not seen wide-spread utilization. First, the topology was

designed specifically for use with an implanted stimulator being designed at Stanford. While having a 1 Mbps link for data transmission into the body is enviable, having a wireless link for getting data out of the body should be considered as a standard feature for any implanted device. In this case, a design approach for such a feature is not apparent, other than constructing a separate transmitter. Second, the stagger tuned design results in a maximum axial coil separation tolerance of approximately 1 cm. The authors also report a maximum overall efficiency of 35% over this distance. Compared to the class-E design, this performance may lead researchers to consider other design approaches. Finally, the authors hold a patent on this design approach [59]. Considering these factors, the class-D, stagger tuned link was not considered for this research.

1.5.3 H-bridge

Another method for controlled current switching of the primary coil is through the H-bridge topology. Only one research group, B.H. Cho's group, has proposed using this topology for a TETS application [23, 61]. (Another group mentions the H-bridge topology in passing, but focus their research efforts on a rectifying scheme [62].) The basic H-bridge circuit consists of 4 power MOSFETs and a coil, as shown in figure 1.2. A DC power source is connected at the top of the bridge. To convert DC to AC, the H-bridge inverter switches on anti-parallel pairs of MOSFETS, 180°out of phase (Q1 and Q3, then Q2 and Q4). This switching regime presents a square wave of voltage to the inductor, which integrates, to produces a triangle wave of current.

An interesting operating property of the H-bridge is its reliance on the built-in diodes in each MOSFET. In a practical H-bridge implementation, there must exist some finite period of time between when one anti-parallel pair of switches turns off and the other pair turns on. The delay prevents the condition where both and upper

and lower MOSFETs are on simultaneously (thereby shorting the power rails). This condition is called shoot-through. In an inductive H-bridge, however, the current flowing through the inductor cannot change instantaneously, regardless of whether the switches are off. Thus, during the on-off delay, the current continues to flow, but it does so through the built-in diodes of the MOSFETS waiting to turn on.

This concept is best understood through example. Assume that switches Q2 and Q4 in figure 1.2 are conducting, so that current is flowing between V+ and ground. When these devices are switched off, there is a delay before Q1 and Q3 turn on. Current must continue to flow in the same direction through L1. At this moment, the polarity of L1 reverses, and the device acts as a current source. The voltage will climb instantaneously to whatever level is needed to maintain the current. This effect turns on the diodes in Q1 and Q3. If the built-in diodes were not present, or if external flyback diodes were not included, the voltage would continue to climb until one of the MOSFETs was destroyed. The built-in diodes are a product of the way the MOSFETs are constructed. This concept is described further in section 2.1.1. Although not shown in the figure, large capacitors are required between V+ and ground, to handle to the large AC currents.

Though few systems use this technique, [61] shows that efficient, high power transfer is realizable. The H-bridge has the advantages of reduced circuit complexity, reduced component count, and operation that is nearly load-independent for regulated loads. Some disadvantages are that significant power can be wasted through switching losses, and that the switches can degrade with prolonged use. However, the advantages of this topology warrant its use for this application.

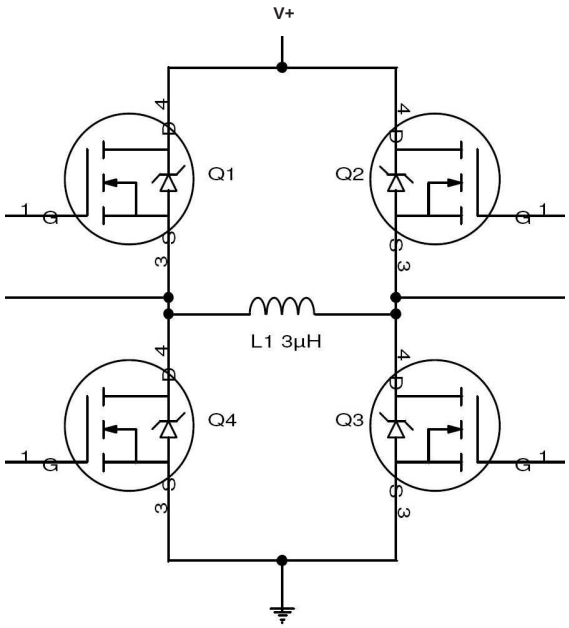

Figure 1.2: Schematic representation of an inductive H-bridge. A controller (not shown) alternately turns on MOSFETs Q1 and Q3 together, then Q2 and Q4 together. This action converts the DC power source V+ into an AC source, so that the primary coil, L1, is energized.

1.6 96-Channel Neural Data Acquisition System

As part of a multi-laboratory brain-machine interface (BMI) project, a 96-channel wireless neural data acquisition system has been developed. The function of the system is to record motor neuron activity, and wirelessly transmit this information out of the body. The data is relayed to an external processor, which maps the neural activity into a set of commands for driving an electromechanical device. A complete description of the 96-channel system, including the TETS described in the remainder of this dissertation, is available in the literature [9].

The acquisition system consists of both implanted and externally worn components. The implanted portion of the system consists of three Digitizing Head-Stage Modules (DHSMs), and an Implanted Central Communications Module (ICCM). Each DHSM collects neural data from thirty-two chronically implanted, cortical electrodes. The analog signals are conditioned and digitized, then sent to the ICCM. Depending on user input, the ICCM can process the data using a spike detection algorithm or other data reduction methods. The data is then packetized and transmitted out of the body over a wireless link. A Wireless Communications Module (WCM) receives the transmission, unpacks the data, and relays the information to other processors for further analysis. A detailed description of the data processing algorithms and wireless protocol can be found in [63]. For prototyping and system development, a graphical user interface was designed for viewing the collected data and other system status information. A block diagram of the acquisition system, along with the TETS, is illustrated in Figure 1.3.

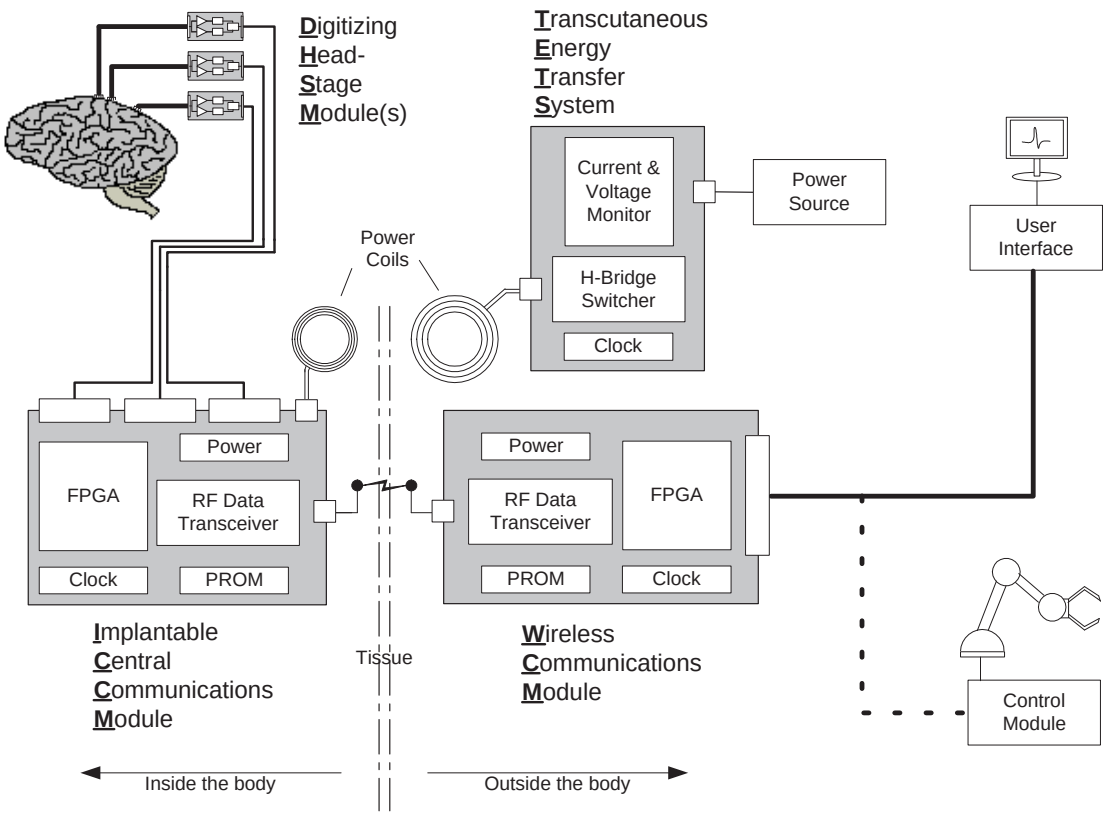

Figure 1.3: Block diagram of the fully-implantable, 96-channel wireless system. Ninety-six microwire electrodes are surgically implanted in the brain. Three, 32-channel digitizing headstage modules (DHSMs) are connected to the electrodes. Digitized data is sent to the Implantable Central Communications Module, where data reduction algorithms are executed. Neural data is passed out of the body via a 916.5 Mhz, 1 Mbps AM transceiver, where it is received by the Wireless Communications Module (WCM). The received data is processed for downstream transmission, to either a prosthetic controller, or to a user interface for viewing. The implanted portion of the system is powered by a transcutaneous energy transfer system (TETS), which supplies approximately 2 W.

The TETS presented in this work was designed along with this 96-channel system. One major system requirement was the need for four regulated power supplies: 5 V, 3.3 V, 2.5 V, and 1.5 V. The electronics that make up the TETS secondary had to be prototyped per this requirement. The technical details concerning power regulation are discussed in chapter 2. As will be shown, significant inefficiencies can accrue depending on the type of regulator. Another obstacle to TETS design is the ability to provide these voltages while maintaining efficiency.

A unique approach taken during acquisition system design was to distribute the implanted components within the body. This approach was taken because of the physical size of the components, in addition to the desire to distance the TETS from the sensitive analog lines on the DHSMs. As a result, the DHSMs were designed to be implanted near the electrode craniotomy, while the ICCM and secondary TETS coil were designed to be implanted in the upper torso.

1.7 Summary and Overview

To summarize the concepts introduced in this chapter, a mid-range TETS design (1-3 W) has yet to be developed for the implanted medical device field. Unlike a high power TETS ($\geq$ 10W), any mid-range application requiring low-noise analog and digital circuitry (i.e., virtually any type of implanted recording system) also requires voltage regulation. Unlike low power systems ($\leq$ 100mW) which can rely on classic linear regulators, a mid-range power supply cannot rely on such an inefficient type of regulator. The technical aspects of this consideration are discussed in detail in chapter 2. Thus, a novel regulation scheme is required that can efficiently supply four voltages, and that can compensate for voltage variability in the secondary, as a result of coil displacements.

Additionally, unlike high power TETS applications, the neural acquisition system

is sensitive to noise. As described above, one approach to mitigating induced noise was the distributed architecture of the implanted components. However, induced noise may still be problematic. Specifically, since the neural data is digitized, aliasing may occur. Each DHSM samples at 31.25 kHz, so frequency multiples of 250 kHz may be aliased into the digitized data. To determine whether the 96-channel system can acquire usable neural data while being powered by the TETS, *in vivo* testing is required.

Another challenge presented in this chapter is temperature. The FDA limits tissue temperature rise to less than 2°C. Studies have shown that power densities on the order of 40 mW/cm^2 would result in a device barely exceeding this limit. For a 2 W application, the surface area of the device would have to be greater than 80 cm^2. This surface area approaches the upper limit of what is reasonably implantable in a human. Thus, a mid-range TETS solution will have to contend with packaging constraints, as well as the need for real-time temperature monitoring.

This dissertation is centered around overcoming these challenges. A 2 W TETS is designed and tested specifically for the implanted neural data acquisition system. A novel regulation scheme is presented, in which switching regulators are used to both mitigate coil misalignment, and increase efficiency in a system requiring four regulated voltages. A custom, 6-channel digital thermometer for real-time temperature monitoring is also designed, built, and tested. The following section outlines the presentation of this work.

1.7.1 Outline

Chapter 2 formally presents the design of the transcutaneous energy transfer system. The H-bridge driver, regulation scheme, and device performance on the test bench are all described in detail. In chapter 3, the electromagnetic field generated by the

primary coil is simulated, and the results analyzed. The results are compared against the safety limits described above. Chapter 4 describes the design of the implanted digital thermometer, as well as the techniques used to calibrate it. Chapter 5 describes a set of six acute *in vivo* studies in an ovine model, in which both the TETS and temperature system are successfully tested. Finally, chapter 6 briefly summarizes the findings and unique contributions of this work.

Chapter 2

Transcutaneous Energy Transfer System Design

To power the 2 W, 96-channel wireless neural acquisition system, a transcutaneous energy transfer system (TETS) was developed, based on the H-bridge circuit topology. This chapter provides a detailed description of the design, as well as the results from *in vitro* testing. As an aid in understanding some of the design considerations, this chapter opens with a background primer on several of the most commonly used power supply components. Once the relevant components are understood, the underlying design goals are stated and the design concepts are described. Following this description, the specific circuit design for the TETS primary and secondary is provided. Finally, the results from testing are presented and discussed.

2.1 Common Power Supply Components and Subcircuits

2.1.1 Power MOSFETs

Metal-oxide-semiconductor field-effect transistors (MOSFETs) are commonly used in electronics, and are well-understood by a general electrical engineering audience. However, in power supply applications, specialty MOSFETs are heavily utilized. One such device is the vertical, double-diffused MOSFET (vertical DMOS or VDMOS). This device has been used for decades because of its useful operating characteristics. Because these characteristics may not be obvious, and because they are important in

this research, a brief discussion is appropriate.

A cross-section through the active region of the VDMOS is shown in figure 2.1. Unlike a standard MOSFET, the drain is located across the substrate from the source. This allows the device to support higher drain-source voltages than typical lateral MOSFETs.

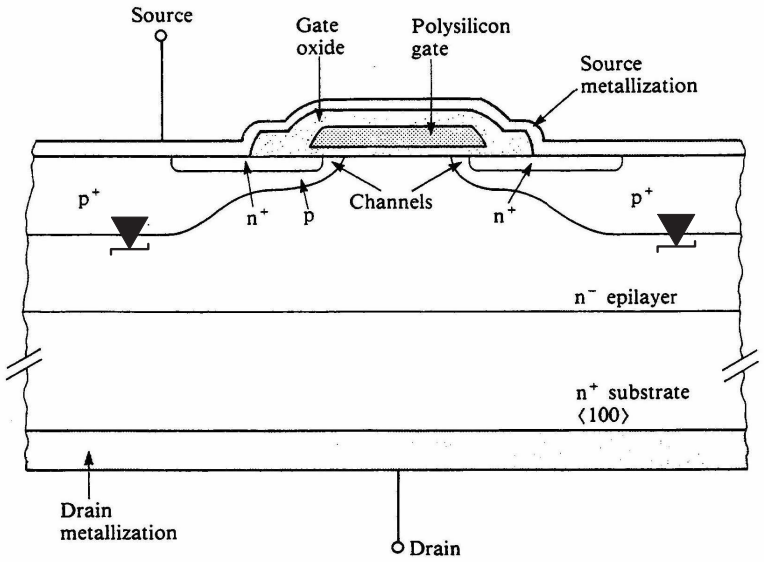

Figure 2.1: Cross-section through the active region of a power MOSFET (adapted from [64]). The parasitic diode between the p^+ body region and the epitaxial layer is shown.

Another very useful feature is that the VDMOS contains a built-in diode between the p^+ region and the drain. The p^+ region is referred to as the "body." Because source metalization contacts the body, the body-drain diode connects the source and drain, allowing for reverse conduction through the device. The current rating for this diode is very similar to the forward current rating of the MOSFET. The diode is also important in that its reverse avalanche-breakdown characteristics determine the voltage rating of the MOSFET [64]. Because the diode can operate in breakdown, schematically, it is given the symbol of a zener diode. It is usually included in the schematic symbol of the MOSFET.

2.1.2 Resonant Capacitors

Many of the TETS discussed in chapter 1 make use of resonant capacitors for either the primary or secondary coils, or both. The purpose of constructing a resonant supply is that the impedance presented by the coil is removed, so that losses are minimized. What makes achieving resonance difficult for a TETS is that the resonant frequency is not fixed. Recall that a transformer is represented as a mutual inductance and two leakage inductances (one for the primary and one for the secondary). The leakage inductance is expressed as $L_{leak} = L(1 - k^2)$. Note that this inductance is dependent on the coupling factor, k, which in turn depends on the mutual inductance of the two coils. It is well-established that the mutual inductance of the coils depends on their positions. For a TETS, the inter-coil spacing is variable, since the coils are displaced when the patient moves. Thus, exactly canceling the leakage inductance with a fixed-value capacitor becomes impossible. Some of the class-E systems combat the shifting inductance by changing the switching frequency of the driver [21, 25]. Again, this approach increases circuit complexity, and is a challenge to maintaining stability and efficient operation. As mentioned above, stagger tuning is another, simpler, method for dealing with shifting resonance.

2.1.3 Voltage Rectifiers

The conversion of an AC voltage into a well-regulated DC voltage is especially crucial for both the analog conditioning and low-voltage digital circuitry of a neural acquisition system. In addition to their potential as noise generators, the rectification and regulation stages can represent one of the biggest sources of power loss [21, 22]. For a 2 W system operating from 3-5 V, peak currents are on the order of hundreds of milliamps. Rectifiers typically employ diodes with voltage drops ranging from 0.32-0.7 V. Thus, hundreds of milliwatts could be wasted. For an application where

temperature rise is crucial, this amount of power loss becomes excessive. The typical full bridge rectifier should absolutely be avoided, since the diode power losses are doubled. Generally, rectifier topologies are not overly complicated, and are widely available in circuit "cook books" [16].

2.1.4 Linear Regulators

A linear regulator is an IC that converts a variable input voltage to a fixed output voltage. A basic diagram is depicted in figure 2.2. Because the device requires very little current to run the internal circuitry (i.e., $I_{out} \gg I_{reg}$), it is considered to have constant current ($I_{in} = I_{out}$) during regulation. For a linear regulator to enter regulation, its characteristic input "dropout voltage" must be exceeded. The dropout voltage is the minimum required input voltage needed to obtain the desired output voltage, and varies from device to device. Low-dropout regulators are available for applications requiring greater efficiency.

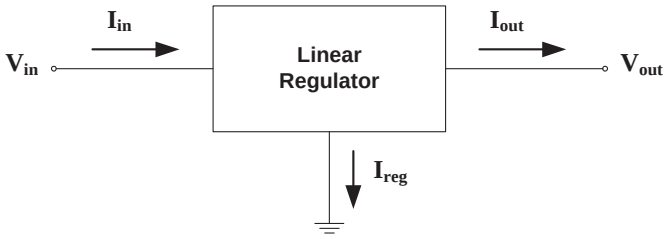

Figure 2.2: Diagram of a basic series linear regulator. Current is essentially constant through the regulator IC ($I_{in} = I_{out}$). Internal electronics drop the voltage difference between the input and output. The power loss is the product of the device current and the input-output voltage difference. As a result, these types of regulators are poorly-suited to receive input voltages that vary, or that are considerably higher than the dropout voltage.

The linear regulator has several advantages over other types of regulators. It is low noise (EMI), has a fast response to changes in input voltage, has low output ripple voltage, and is easy to employ, as it requires minimal external components. It

also provides very tight regulation for changes in the output current (load regulation) [65, 66].

However, there is one significant disadvantage to using this type of regulator: it is quite inefficient. Since current is essentially constant through the device, the internal electronics have to drop the voltage difference between the input and output. For applications requiring large amounts of current, or a large input/output voltage differential, the linear regulator consumes a substantial amount of power. It is not unusual for linear regulators to have efficiencies on the order of 40-55% [65]. Thus, these devices also have high thermal dissipation. While the effects of these characteristics will vary between high and low power systems, they can dramatically reduce overall system power efficiency. Some designers have tried to bypass these issues by either eliminating traditional regulation [21, 25], or by designing an application specific integrated circuit (ASIC) to implement both rectifying and regulation stages [67, 68]. In general, linear regulators are not well-suited to receive the variable voltage input provided the secondary coil. However, these devices could be used downstream from the input stage to help reduce noise, if the input voltage could be kept relatively near dropout. In this case, commercially available IC regulators offer a practical solution in terms of development time, cost, and performance.

2.1.5 Switching Regulators

Like linear regulators, switching regulators convert a variable input voltage to a fixed output voltage. Other than this commonality, the two types of regulators are wildly different. Switching regulators are classically divided into four topologies: buck (step-down), boost (step-up), buck-boost (step-up or step-down), or Cúk (zero output current ripple) [69, 70]. In general, regulators are classified as a type of power converter. There are three major types of converters, into which each of the above

regulator topologies may be categorized: flyback, forward, or push-pull [66]. Because of its simplicity, low component-count, high-efficiency (60-90% [65]), and method of operation, this discussion will be limited to the forward buck regulator. The circuit topology is presented in figure 2.3.

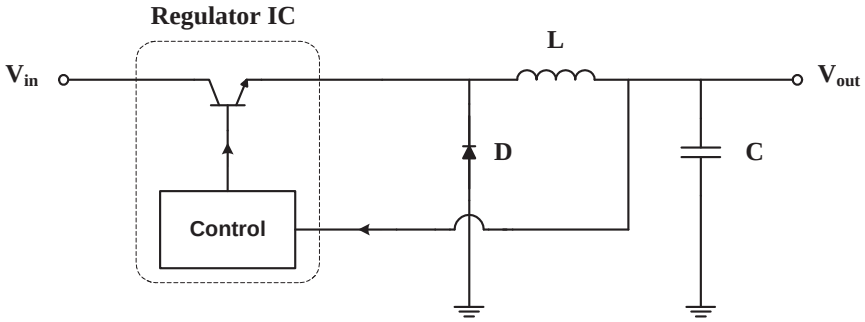

Figure 2.3: Diagram of a basic step-down "buck" regulator. Unlike linear regulators which simply dissipate excess input power, the buck regulator exchanges voltage and current to maintain constant power across the IC. A feedback sense line ensures that the internal transistor is switched only as needed, to maintain the proper output voltage.

Unlike linear regulators which simply dissipate excess input power, the buck regulator exchanges voltage and current to maintain constant power across the IC. When the transistor switch is closed, current flows through the inductor, to produce a voltage at the output. When the switch opens, current must remain continuous through the inductor. The voltage polarity of the inductor reverses, forward biasing the flyback diode, and allowing the current to ramp down through the DLC freewheel path. During this phase of operation, the inductor transfers its energy to the capacitor. A sense line at the LC node allows the IC to vary the switching time to maintain the appropriate output voltage, depending on the input voltage. A nice feature of the buck regulator is that with higher input voltages, the input current is reduced. Essentially, this negative impedance characteristic means that when the input voltage is low, the impedance presented to the source is reduced, allowing the regulator

to compensate for the change in drive strength. Such a feature is invaluable in an inductively-powered system, where the drive strength will vary with coil separation.

2.2 Construction of Spiral Inductors

Generally, the primary and secondary coils are composed of different gauges of Litz wire. The word 'Litz' is derived from the German word 'Litzendraht,' meaning 'woven wire.' It consists of individually insulated copper strands that are twisted together to form a single wire. Each strand takes all possible positions in the cross section of the wire, which equalizes flux linkage, thereby equalizing the current in each strand. The benefit of using Litz wire is that AC resistance is minimized at higher frequencies, in spite of decreases in skin depth.

Proper coil design is critical for coil misalignment tolerance and heat minimization. Typically, a flat, spiral-shaped single-layer coil is preferred, with the outer diameter of the secondary coil being smaller than that of the primary coil. This geometry mitigates the reduced coupling brought on by radial coil misalignments, since radially distributed turns ensures that the flux linkage is approximately maintained during a radial displacement [71].

Another feature of the spiral geometry is that it results in coils that are somewhat flexible. Because discomfort and tissue damage can result from a rigid coil, particularly the implanted coil, some degree of flexibility is needed. The outer coatings of the coils will also have a large impact on flexibility. Encapsulating materials have included Pellathane [72] and Dacron velour [27], but the most common encapsulation is either medical-grade silicone rubber or Silastic [25, 28]. Silicone-based materials offer tremendous flexibility and superior biocompatibility.

The most prominent feature of a coil is its inductive characteristics. The self and mutual inductances of planar spiral coils have been analytically derived. Closed

form expressions for this geometry are not available. However, several computational techniques have been suggested. These methods are based on variations of Neumann's formula or have been derived from Maxwell's equations [73, 74, 75]. One disadvantage to these methods, is that inductance is related to coil size in a convoluted way. Another widely cited solution technique is outlined in [76]. In this case, inductance is determined using the coil dimensions and data from a look-up table. Although some interpolation is required, the relationship between inductance and coil size is more readily apparent.

2.3 TETS Design Concepts

The overall design goal was to construct a TETS whose primary circuit can operate relatively independent of the secondary load, and that achieves axial coil separation tolerance by dramatically exceeding the minimum input voltage of a secondary regulator. This approach takes advantage of the higher efficiency and input voltage tolerance of switching regulators. These fundamentals have been discussed, and in this section, the high level TETS design is presented. The concept of reflected impedance is also introduced, and a description of link efficiency is provided.

2.3.1 System Overview

A block diagram of the TETS primary and the secondary is shown in figure 2.4. This system features a tunable switching frequency, electronic circuit breaker protections, and a novel current sense circuit for detecting the secondary load.

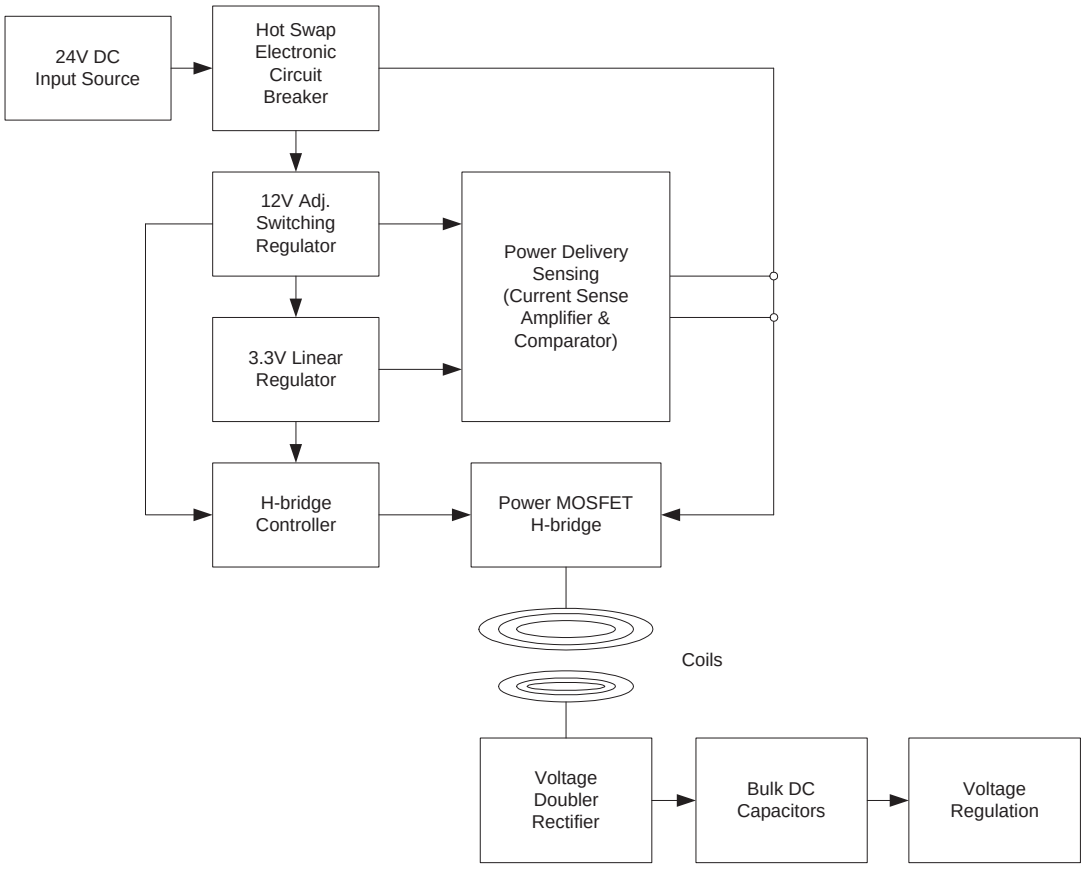

Figure 2.4: Block diagram of TETS primary and secondary circuits. The primary operates from a single 24 VDC power source (batteries or other supply). A hot swap electronic circuit breaker monitors for overvoltage, undervoltage and overcurrent conditions in the primary. The 12V and 3.3V regulators supply local power to the circuits of the TETS primary. An H-bridge controller switches power MOSFETS, converting 24 VDC power into AC power, and energizing the primary coil. A power delivery sensing circuit detects the proximity of the secondary by observing an increase in delivered current. In the secondary, a voltage doubler rectifier feeds a pair of bulk DC caps, which smooth the voltage and provide temporary power during periods of brief coil misalignment. The most crucial components for tolerating coil displacement are two step-down switching regulators. These devices provide power to a set of linear regulators, which ultimately power the implanted neural acquisition system.

The TETS primary can operate from external DC power sources ranging from 9 V to 45 V, with minimal hardware modification. Typically, a 24 V DC source is used. A high voltage hot swap controller provides resistor programmable over- and under-voltage protection, and surge current protection. Input power is delivered to onboard 3.3 V and adjustable 12 V regulators, which in turn provide power to the current sense and H-bridge control circuitry. The current sense circuit consists of a commercial current sense amplifier integrated circuit (IC), and comparator. The H-bridge controller consists of a full-bridge driver IC and a low power, potentiometer-adjusted oscillator. This controller switches the power MOSFETs in the H-bridge to control current through the custom-wound primary coil. The H-bridge consists of four of these MOSFETs, and is powered by the external DC power source (24 V). Because of the operating characteristics of the H-bridge, a wide range of primary coil geometries and inductances can be driven by the TETS.

The secondary coil is energized through the linked magnetic flux established by the primary coil. The implant site of this smaller coil is located away from the Implanted Central Communications Module (ICCM) to avoid induced eddy currents in the ICCM enclosure. The coil is positioned by feeding it through a subdermal tunnel. On the ICCM, the coil leads connect to a voltage doubling rectifier. The output of the rectifier feeds a pair of bulk capacitors that stabilize the voltage during transient coil misalignments. Finally, power is delivered to a series of regulator ICs that produce the voltages required by the implanted acquisition system. The first in the cascade are a pair of high input voltage switching regulators, which efficiently step-down the rectified voltage. Following the switching regulators are the linear regulators that deliver power to the rest of the acquisition system.

2.3.2 Reflected Impedance

To demonstrate that a TETS based on the H-bridge topology operates relatively independent of the load, the reflected impedance of the secondary, into the primary, must be examined. In addition, determining the reflected impedance is useful as a way of formally showing how the secondary circuit can be detected in the primary circuit (a novel feature of the TETS design). A very nice review of the circuit analysis for calculating reflected impedance is given in [53]. The analysis presented here follows from their results, and is shown graphically in figure 2.5.

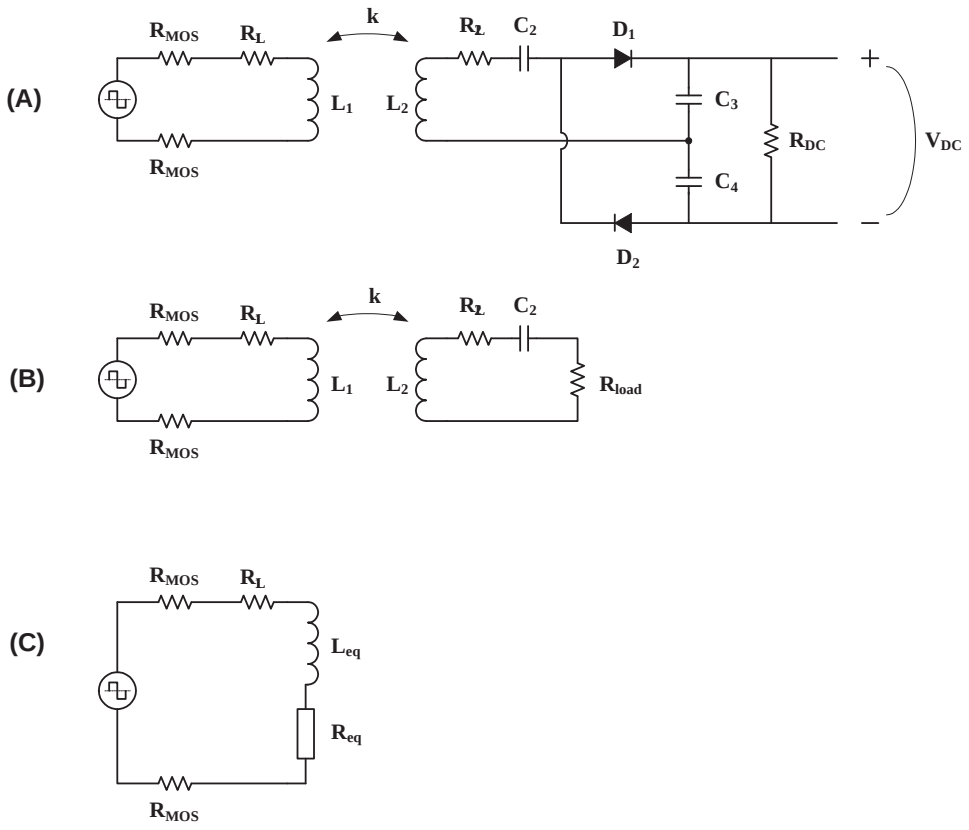

Figure 2.5: Schematic representation of reflected impedance. (A) The power MOSFET H-bridge is represented as a square wave voltage source. Two resistors, R_{MOS}, are the on-resistance on the MOSFETs. Resistor R_{L1} is the equivalent series resistance (ESR) of the primary coil, L_1. The secondary coil, L_2 also has an associated ESR represented by R_{L2}. A voltage doubler rectifier (discussed in section 2.6.2) is formed by D_1, D_2, C_3, and C_4. The regulators that are downstream from the rectifier are represented as a single resistor, R_{DC}. (B) Using eqn. 2.1, the rectifier and R_{DC} are transformed into a load resistance, R_{load}, seen by the reactive components of the secondary. (C) Finally, using eqn. 2.3, the complete secondary is reflected into the primary, and is represented by a single resistance, R_{eq}.

First, the equivalent DC resistance of the regulators is determined (R_{DC} in figure 2.5 (A)). Note that this resistance is dynamic; it changes as a function of the input voltage. Once in regulation, buck switching converters typically demonstrate a negative impedance characteristic with increasing input voltage. Because the regulator input voltage is a function of coil position, the range of values of the equivalent DC resistance can be determined experimentally, by varying the coil separation. (The resistance can also be determined by simply connecting a power supply to the regulator input, and sweeping the voltage.)

Once this resistance is known, equation 2.1 is used to determine the equivalent AC load resistor seen by the reactive portion of the secondary [53].

$$R_{load} = \frac{R_{DC}}{8}\left(1 + \frac{2V_{diode}}{V_{DC}}\right) \tag{2.1}$$

In this equation, V_{diode} is the voltage drop associated with the conducting diode. The equivalent circuit is shown in figure 2.5 (B). The reflected impedance is then combined with the primary circuit to produce an equivalent impedance (figure 2.5 (C)).

$$Z_{eq} = \frac{\omega^3 k^2 L_1 L_2 C_2 \left[\omega C_2 (R_{load} + R_{L_2}) + j(1 - \omega^2 L_2 C_2)\right]}{\omega^2 C_2^2 (R_{load} + R_{L_2})^2 + (1 - \omega^2 L_2 C_2)} \tag{2.2}$$

At the resonance frequency, the imaginary (reactive) part vanishes. The remaining real part is given by:

$$R_{eq} = \frac{k^2 L_1}{C_2 (R_{load} + R_{L_2})} \tag{2.3}$$

The results from this equation will be compared against predicted and measured values, in a later section.

2.3.3 Efficiency

An important measure in any energy transfer system is efficiency. What is interesting about efficiency measures, with respect to the field of inductive power links, is that overall DC-DC efficiency is rarely presented. More often, the link efficiency is calculated. The link efficiency represents the amount of power that is put into the inductive portion of the link, versus the amount of power received by the load resistor. Absent from this measure is the power required to operate the control circuitry of the primary. Neglecting this power may result in a substantial reduction in the efficiency. However, in order to compare the present design with other TETS, the link efficiency is calculated according to [53]. With this method, the efficiencies of the primary and secondary are combined to produce the total link efficiency. The primary efficiency is given by:

$$\eta_{primary} = \frac{R_{eq}}{R_{eq} + (R_{L_1} + 2R_{MOS})} \tag{2.4}$$

The efficiency of the secondary is given by:

$$\eta_{secondary} = \frac{R_{load}}{R_{load} + R_{L_2}} \tag{2.5}$$

The total link efficiency is the product of the primary and secondary efficiencies.

$$\eta_{link} = (\eta_{primary})(\eta_{secondary}) = \frac{k^2 Q_{L_1} \omega C_2 R_{load}}{\left(1 + k^2 Q_{L_1} + \frac{1}{Q_{L_2}}\right)\left(\omega C_2 R_{load} + \frac{1}{Q_{L_2}}\right)} \tag{2.6}$$

Note that η_{link} can be also be calculated from the primary and secondary coil Qs, as indicated in the equation. Each Q must take R_{MOS} into account. In addition to

the above efficiency measure, the overall DC-DC efficiency is reported later in this chapter, for thoroughness.

2.4 TETS Primary Circuit

This section is a description of the components used to construct the primary TETS circuit. Component tolerances and other specifications that are applicable to TETS operation are provided. It should be noted that this section, along with the following two sections, are not organized as a guide, or chronology, on how the TETS was designed. Rather, they are a description of the system that was built and the results from testing it. This description roughly follows from figure 1.1. The primary circuit, coils, and secondary circuit are described in that order. As is typical, the actual design was a recursive process involving multiple trade-offs, and which alternated between trial-and-error and formal first-order design equations. (Circuit simulation was not a major element in the TETS design.)

2.4.1 DC Power Source

The TETS can operate on input DC voltages ranging from 9 V to 45 V. The lower limit is determined by the minimum input voltage specification of the hot swap electronic circuit breaker (section 2.4.2). The upper operating limit is determined by the maximum input voltage specification of the 12 V switching regulator (section 2.4.3). Under normal circumstance, the TETS operates from a 24 V DC power source. The major criterion in selecting this voltage was that it could provide more than enough drive strength to induce the voltage levels required in the secondary (5 V regulated maximum). Another major criterion in selecting this voltage was its availability in a wheelchair application. Motorized wheelchairs operate from two 12 V automotive batteries. In research settings where the test subject can be either

stationary or mobile, the following methods can be used to power the TETS.

Wall outlet-based power supplies

Where the test subject is restrained, a Condor (Oxnard, CA) 60W GXM60 medical-grade supply is used to power the TETS. This supply can output a maximum of 2.5 A, and features short circuit and overvoltage protection. It can tolerate AC inputs of 90-264 V at 47-63 Hz. Leakage current is limited to 80 μA under normal operating conditions.

Batteries

To power the system during mobile applications, two 12 V, 4500 mAh Ni-MH battery packs are used. The batteries weigh approximately 1.5 lbs. The 4500 mAh energy capacity of the batteries allows them to operate for approximately 12.5 hours.

2.4.2 Electrical Safety Features

To be viable in a clinical or research setting, the TETS primary circuit includes safety features to protect both the electrical components and the test subject from electrical failure.

Reverse polarity protection diode

To protect against a reverse polarity condition on the input DC power source, A 100 V, 1.5 A Schottky diode is used at the power input jack. This component protects the TETS primary circuitry by blocking reverse current through the ground pins of the ICs.

Hot swap electronic circuit breaker

To protect the TETS primary circuit against overvoltage, undervoltage, or a short circuit condition, an LT1641-2 high voltage hot swap controller (Linear Technology, Milpitas, CA) is used at the input. This chip is designed to ramp up a board's supply voltage in a controlled manner, so that surges do not damage other onboard ICs. The controller uses an external N-channel pass transistor to perform this function. The chip lights an LED if the input current and voltage are within specified limits.

For the current limiting feature, the device features a resistor-programmed fold-back current limit. Once the current limit has been reached, the device folds back the current, and engages a timer circuit. The chip operates in current limit for an amount of time determined by external capacitor selection. For the TETS, a 0.68 μF was used, which results in an 11 ms shutoff time. The current limit was set to 940 mA, or about 3 times the maximum expected current under normal conditions.

Under-voltage detection is also programmable using a resistor divider connected to a dedicated pin. The under-voltage threshold was set to 19.33 V. Over-voltage protection is accomplished by connecting a zener diode to the timer circuit of the chip. When an overvoltage condition exists, the diode's breakdown voltage is exceeded, and the timer circuit turns off the power. A 28 V zener diode was used for this purpose.

2.4.3 Voltage Regulation

To power the TETS primary subcircuits, the 24 V input source must be stepped-down. A 12 V switching regulator and a 3.3 V linear regulator are used for providing local power. The regulators are cascaded so that the switching regulator steps down the 24 V efficiently, providing power for the less efficient linear regulator. These devices are described below.

12 V nominal switching regulator

The LM2825 (National Semiconductor, Santa Clara, CA) is a complete 12V, 1 A DC-DC step-down (buck) converter, packaged in a 24-pin DIP. Contained within this package are all the active and passive components of a switching regulator. No external passive components are required. The part is available in either 12 V or adjustable output versions. This design uses the adjustable version; however, the 12 V version is completely compatible with the circuit. The adjustable model allows the output voltage to be lowered to 10 V, which reduces heat in the HIP4080A switching controller (discussed in section 2.4.5).

The switching regulator is responsible for powering the following devices: The H-bridge controller (HIP4080A), the 3.3 V linear regulator, two LEDs, and an optional cooling fan (not used in this design). The maximum expected current consumption of these devices is approximately 100 mA.

3.3 V linear regulator

The L78L33 (ST Microelectronics, Carrollton, TX) is a standard linear voltage regulator. It receives power from the switching regulator, and produces 3.3 V at up to 100 mA. The linear regulator provides power for the following devices: the H-bridge controller, oscillator, current sense amplifier, and comparator. The expected load of the regulator is around 2 mA.

Because the current sense circuit (described in section 2.7.8) is sensitive to switching noise, a first order low pass RC filter is used at the input to the 3.3 V regulator. A 1 kΩ resistor and 1 μF capacitor were used, for a cutoff frequency of 160 Hz. The switching frequency of the 12 V regulator is 150 kHz, and the nominal switching frequency of the H-bridge is 250 kHz. Thus, over three decades, this filter provides 60 dB attenuation. It also mitigates excessive loss in the regulator by moving a small

portion of the power loss out of the regulator IC and putting it in the filter's resistor.

2.4.4 Power Delivery Sensing

This portion of the TETS is responsible for measuring the amount of power being absorbed in the secondary. The theory behind this concept is that as the coils are brought in proximity to one another, the primary will begin to deliver power to the secondary. The primary DC power supply must compensate for the increase in dissipated power by supplying more current (since the only way to increase power for a fixed voltage source is to increase current). Knowing the exact amount of power consumed in the secondary should allow for a close prediction of the increase in primary DC current.

The two ICs used to implement this function are the LT6100 current sense amplifier (Linear Technology, Milpitas, CA), and the LMC7211 comparator (National Semiconductor, Santa Clara, CA). The current sense amplifier converts the delivered current into a voltage, which is then compared to a set voltage by the comparator. Specifications for these devices are briefly given below.

Current sense amplifier

The LT6100 is a precision, micropower, high side current sense amplifier. It has a separate power supply input that allows it to operate from the 3.3V supply. The device has fixed, pin-programmable gains of 10, 12.5, 20, 25, 40 and 50 V/V. The input sense pins are biased off when the device is powered down, to prevent loading of the monitored voltage. A filter pin is available for low pass noise filtering. The pole of the filter is specified by the size of an external capacitor connected to the pin. A value of 0.1 μF was chosen to establish a 12 Hz cutoff frequency.

The gain of the amplifier was set according the measured current drawn from the

DC power source during prototyping. The current ranged from 0.16 mA when the secondary was absent, to 0.333 mA when the two coils were within 10mm. A gain of 40 was chosen, so that the output of the amplifier would vary by around 700 mV for these two conditions. This range is wide enough to accommodate the threshold of the comparator, even in a noisy environment.

Comparator

The LMC7211 is a micropower CMOS comparator with rail-to-rail input and push-pull output. It operates from the 3.3 V supply. For this application, positive feedback is used to add 100 mV of hysteresis to prevent multiple threshold crossings. The threshold can be resistor programmed, but in this application, a potentiometer was used for in-circuit tuning. The output of the comparator was tied to an n-channel MOSFET, to activate an LED mounted to the TETS enclosure.

2.4.5 H-bridge Controller

A commercially available H-bridge driver was used to control MOSFET switching. The HIP4080A (Intersil, Milpitas, CA) is an N-channel MOSFET driver IC, capable of switching at frequencies up to 1 MHZ. The device can operate over high-side bridge voltages ranging from 10-80 V. It can provide 2.5 A peak pull-up and pull-down gate current, for rapidly turning on and off transistors. Switching is managed by two pins that are the input to a control comparator. When the voltage on one input pin is higher than the other, one pair of anti-parallel MOSFETS is switched on, the other pair is switched off. The opposite effect is true when the input voltage condition is reversed. The approach taken for this design was to use a voltage divider to place one of the pins near the center of the 3.3 V range. The other pin was connected to a 3.3 V square wave oscillator.

In addition to simplified switching control, the HIP4080A has several features that make it convenient to use. Although the device is compatible with 5 V logic, all of the input pins can operate at 3.3 V logic levels. Thus, the need for an additional voltage regulator is avoided. There is also a resistor-programmed turn-on delay for the high-side and low-side switches. The delays guarantee that both MOSFETS in the same bridge leg are not simultaneously on. Such a condition would allow current to flow directly from the power rail to ground (a condition called shoot-through), potentially causing catastrophic damage to components. The delay circuitry is a valuable circuit protection feature. In this application, 50 kΩ resistors were used to establish a delay of approximately 15 ns.

Finally, although the HIP4080A operates from a nominal 12 V supply, the input voltage can be decreased to reduce power loss. In this application, the LM2825 12 V regulator was resistor programmed to output 10 V. The only major disadvantage of reducing the supply voltage is that the MOSFETs in the H-bridge may not be fully turned-on. A consequence is that the on-resistance could go up, which would reduce or eliminate the benefits of lowering the supply to 10 V. However, for the MOSFETs used (described in section 2.4.6), all ratings are guaranteed at 10 V gate-source voltage. Therefore, turning down the supply voltage is prudent.

Oscillator

A standard low power square wave oscillator (LTC6900, Linear Technology) was used to control switching in the HIP4080A. The oscillation frequency of the component is resistor set. The only notable feature for this application is that a potentiometer was used to allow the frequency to be tuned by the user. This feature is important for reducing aliased TETS noise in the recording front-end.

2.4.6 H-bridge Components

The H-bridge consists of 3 major components: a custom wound coil, four power MOSFETs, and one or more polymer capacitors. The coil is discussed in detail in section 2.5. Below, is a description of the remaining components.

Power MOSFETs

MOSFET selection was based on trade-offs between the following device parameters: Drain-to-source breakdown voltage (V_{DSS}), continuous drain current (I_D), static drain-to-source on-resistance ($R_{DS(on)}$), total gate charge (Q_g), and component size. V_{DSS} and I_D were chosen to accommodate roughly twice the expected values: 55 V and 30 A, respectively.

The most difficult optimization was simultaneously minimizing $R_{DS(on)}$ and Q_g, which oppose one another. A low $R_{DS(on)}$ results in low loss from high current. A low Q_g means that less current is required to turn the MOSFET on, thereby lowering the power loss experienced in the H-bridge driver. Ultimately, the IRFR4105 (International Rectifier, El Segundo, CA) was selected. For this component the maximum $R_{DS(on)}$ is 24.5 mΩ, and the maximum Q_g is 27 nC.

Polymer capacitors

Because the primary and secondary coils are so loosely coupled, only a small amount of the energy radiated from the primary, is coupled into the secondary. Therefore, a large amount of energy must be developed in the primary. Consequently, very large circulating currents are present in the H-bridge. To prevent turning the DC source (batteries) into an AC source, large DC filter capacitors are used. In addition to the other components in the circulation path, the capacitors can also reduce the overall efficiency through power loss. Specifically, the capacitors exhibit I^2R loss, where R

represents the equivalent series resistance (ESR) of the component.

In order to minimize power loss, polymer film capacitors were chosen. This capacitor technology has several advantages over traditional electrolytic and ceramic devices. First, polymer film capacitors have twice the energy density of electrolytic caps, and more than ten times the energy density as ceramics [77]. They also have stable capacitance with both time and temperature. Finally, compared to all other capacitor technologies, they have a very low ESR at frequencies of 100kHz and greater [77, 78].

2.4.7 TETS Board

The TETS printed circuit board (PCB) is 7cm× 10cm, and consists of 6-layers. Both outer layers are populated. With the exception of several of the larger capacitors, surface mount footprints were used for all components. Geometries as small as 0602 were used where power dissipation allowed for it. All components, therefore, can be hand-soldered. The board was designed to isolate, as much as possible, the noise generating switching components from the sensitive current sense amplifier, comparator and hot swap controller traces. Specifically, the MOSFET H-bridge and controller are mounted on one portion of one side of the board, the remaining components reside on the other side of the board, contra-lateral to the H-bridge. Ground fencing was also used liberally, to provide a low impedance return path for radiated noise.

Extensive use of split planes was used for routing power on the inner layers. To the extent possible, these planes were kept from overlapping, to prevent capacitive noise coupling between layers. A slotted ground plane was used to isolate return paths for the high circulation current, and noise from the 12 V switching regulator. Several signal traces were also routed on the inner layers. All signal traces were kept as short as possible. A description of the stack-up is provided below.

1. Top Layer: Components (Linear regulator, hot swap controller, current sense amplifier, and comparator), and copper pours for MOSFET thermal dissipation.

2. Inner Layer 1: Slotted ground plane.

3. Inner Layer 2: Small copper pour for 12 V input terminal, small pour for cooling fan ground (optional), and large pour for 24 V switching current.

4. Inner Layer 3: Copper pours for 12 V regulator input and output, and signal trace for MOSFET gate control.

5. Inner Layer 4: Copper pour for 3.3 V power, pour for 12 V fan power (optional), pour for one leg of primary coil, and signal traces for MOSFET gate control.

6. Bottom Layer: Switching components (power MOSFETS, HIP4080A switching controller, gate resistors, 12 V switching regulator, bulk capacitors), and a pour for the other leg of the primary coil.

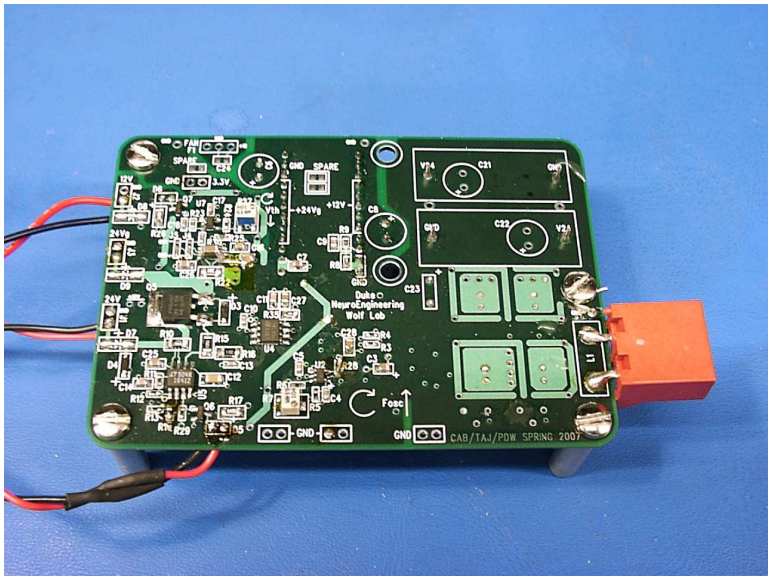

Figure 2.6: Photograph of the top layer of the finished TETS board. The left half of the board is dedicated to the electronic circuit breaker, current sense circuit, and 3.3 V regulator. The right side of the board is relatively unpopulated, due to noise and temperature effects brought on by high circulating currents. Only the oscillator and several support components of the H-bridge controller are located close to these currents. The underside of the power MOSFETs are denoted by the large thermal ties and ground fencing in the lower right side of the board. The large connector to the right is where the primary coil is connected.

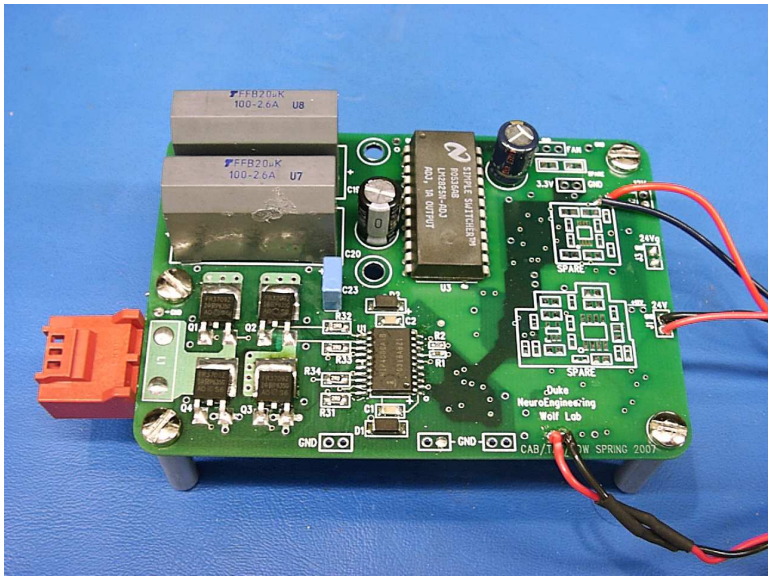

Figure 2.7: Photograph of the bottom layer of the finished TETS board. Major TETS subcircuits housed on this half of the board include the 12 V regulator, power MOSFET H-bridge and controller, and the polymer capacitors. Along the right side of the board are several unpopulated prototyping areas.

During TETS operation, the power MOSFETs dissipate heat. To increase the surface area for thermal dissipation, several large vias were used to connect the drain pad of each device to a copper pour on the opposite side of the board. Each of these pours was surrounded by ground fencing to reduce noise radiation. Figure 2.6 shows these thermal pours.

At various locations on the board, through-hole jacks were provided for measuring regulated power, and for access to ground. Several prototyping areas were also included for future expansion. Finally, a jack for powering an optional cooling fan was included. Because fans are electrically noisy, this jack was isolated from the rest of the board using separate copper pours for power and ground.

2.5 Coil Design

The primary and secondary coils were hand wound using commercially available litz wire. While formulas are available for predicting the self and mutual inductances of planar spiral coils [75, 76], generic guidelines have been also published for coil design [71, 79]. Both the guidelines and formal techniques were consulted during coil fabrication. However, in addition to inductance, the other factors used in determining the final design were heat dissipation, implant size, and ease of fabrication. Results from experimental testing were used to refine the design. The construction techniques and coil specifications are discussed below.

2.5.1 Primary Coil Design

The primary coil was constructed using 14 AWG, type 3 Litz wire (Cooner Wire, Chatsworth, CA). The wire consisted of 1050 strands of 44 AWG copper. Each strand was coated with solderable polyurethane for inter-strand insulation. The wire was bundled in a single layer nylon serving, which holds the shape of the wire. Although the finished wire diameter was specified as 14 AWG (1.63 mm), the actual diameter was closer to 12 AWG (2.05 mm).

To form the coil, a hollow, 30 mm diameter PVC tube was fixed to a large Teflon block. The Litz wire was wrapped around the tube from the inside out. A total of 7 turns were wound. To hold the turns in place, Med2-4213 adhesive silicone (Nusil, Carpinteria, CA) was applied. The coil was cured at 60°C in a convection oven. After curing the coil, the leads were twisted around one another and fed through a woven ground shield. A heat-shrink tube was then used as outer insulation. A final layer of silicone adhesive was used to seal and insulate the coil cable where it meets the coil.

After the initial sheep experiment (discussed in Chapter 5), it was determined that a magnet would be necessary to help hold the primary and secondary in place

during testing. A 25 mm diameter ceramic (non-conducting) magnet was used for this purpose. The thickness of the magnet was 4 mm. It was held in place in the center of the coil using additional silicone adhesive. A photograph of the completed primary coil assembly is shown in figure 2.8.

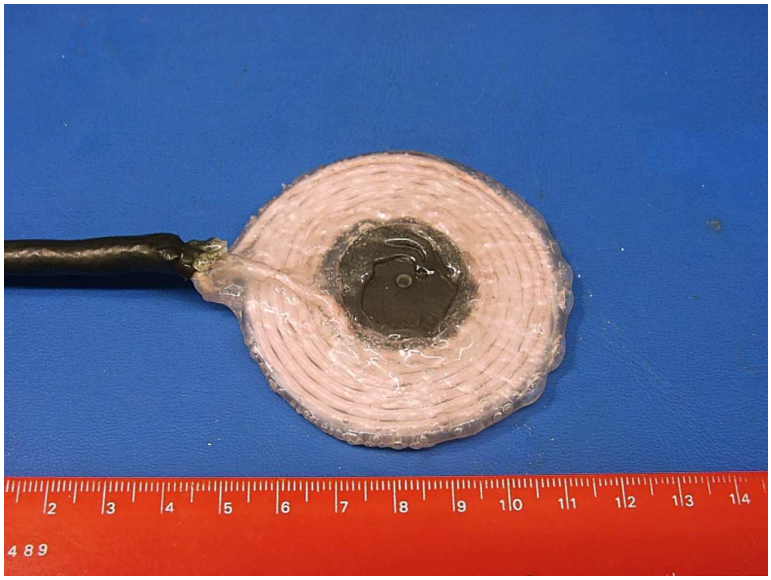

Figure 2.8: Photograph of the encapsulated primary coil with embedded ceramic magnet. The finished inner diameter of the primary coil was 30 mm, and the outer diameter was approxiamtely 56 mm. The coils consists of 7 turns of 14 AWG Litz wire. Silicone adhesive was used to encapsulate the coil. The thicker sections of adhesive were 2-3 mm thick. The coil lead wires were twisted together and covered in a woven ground shield. Heat shrink tubing was used as an outer insulator.

The finished coil has an inner diameter of approximately 30 mm, and an outer diameter of approximately 56 mm. The leads are approximately 80 cm long: more than enough length to allow the TETS driver to be conveniently worn. Following fabrication, the inductance and equivalent series resistance (ESR) of the coil were measured at 250 kHz, using an HP 4284A precision LCR meter. The measured inductance was 3 μH and the ESR was 0.13 Ω. The meter can also calculate the quality factor (Q) of the coil. That value was 34. The presence of the magnet had no effect on the measurements.

2.5.2 Secondary Coil Design

The secondary coil was wound using 22 AWG, type 2 Litz wire (New England Wire, Lisbon, NH). The wire consisted of 105 strands of 42 AWG copper. Each strand

was coated with solderable polyurethane for inter-strand insulation. The wire was bundled in a single layer nylon serving.

The secondary coil was formed differently than the primary coil. Because the wire diameter is considerably smaller, a coil winding "yo-yo" was collaboratively developed. The yo-yo was formed by two plastic sheets, with a thin plastic spacer, held together with a center bolt. This assembly was held in place with a vice during winding. The interior of the yo-yo was filled with Med2-4213 adhesive silicone, and the wire was quickly wound around the center bolt. The plastic sheets put pressure on the wire so that a planar spiral was formed. The coil was left in the yo-yo while being cured at 60 °C. After curing, the thin plastic sheets were gently peeled away from the coil.

Similar to the primary coil, the leads of the secondary coil were wrapped around one another and fed through a braided ground shield. Because the secondary coil was used in the body, special packaging procedures were required to ruggedize it. Section 5.2.3 presents the details. A photograph of the finished secondary coil is shown in figure 5.3 of that section.

The finished coil had an inner diameter of approximately 30 mm, and an outer diameter of approximately 45 mm. The leads are approximately 30 cm long: more than enough length to separate the Can and coil. The inductance and ESR of the coil were measured at 250 kHz with the precision LCR meter. The inductance was 4.3 μH and the ESR was 0.18 Ω. The coil Q was 35.

2.6 TETS Secondary Circuit

This section is a description of the components used to construct the secondary TETS circuit. Component tolerances and other specifications that are applicable to TETS operation are provided.

2.6.1 Resonant Capacitor

A series-resonant capacitor was used to cancel the leakage inductance of the secondary coil. Recall from section 2.1.2 that this inductance changes depending on the coupling. To determine the coupling, the mutual inductance was calculated using Grover's technique [76], for axial coil displacements of 1-30 mm. Using a 0.1 μF resonant capacitor, the resonant frequency was approximately 250 kHz, at a intercoil distance of 14-15 mm. The resonant frequencies ranged from approximately 243 kHz at large axial displacements, to 360 kHz when the coils were nearly touching.

2.6.2 Rectifier

Since the approach to coil misalignment is to overshoot the voltage input to the regulators, a voltage doubler rectifier was employed. The rectifier is shown schematically in figure 2.9.

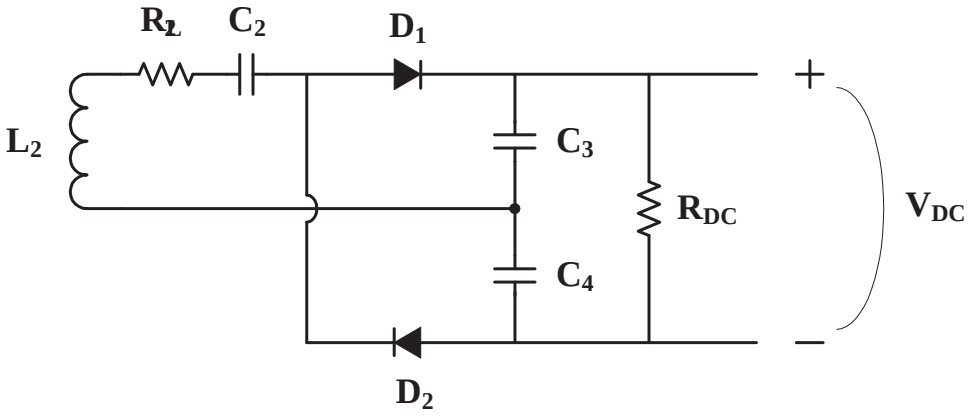

Figure 2.9: Schematic of the voltage doubler rectifier. Resistor R_{DC} represents the downstream regulators and associated electronics of the neural acquisition system. The voltage doubler is a fullwave rectifier, since both phases of the received signal are passed to the capacitors. An advantage of this particular topology is that the need for a center-tapped inductor is avoided.

A 10MQ100N Schottky diode (International Rectifier) was used in this design.

This component is rated for continuous current of 2.1 A DC, and 100 V maximum DC reverse voltage. The forward voltage drop is 0.78 V.

Capacitors C_3 and C_4 were selected to reduce voltage ripple. Although very large downstream capacitors make sizing these rectifier capacitors moot, a brief discussion of component selection is included here. (These large capacitors are described in the next section.) The following equation demonstrates how to calculate the required capacitance for a desired ripple voltage.

$$C = \frac{I\Delta t}{\Delta V} \tag{2.7}$$

Where, I is the expected current, Δt is half the switching period, and ΔV is the ripple voltage. If the rectifier were directly supplying the downstream components (DHSMs and ICCM components), a safe over-estimate of the required current is 0.5 A. A ripple voltage of 0.2 V is less than 1% of the typical rectifier output voltage of approximately 20 V (for coils separated by 5-10 mm). As described below, the ICCM switching regulators fall out of regulation at approximately 7 V, which means a 0.2 V ripple is around 3% of the rectifier output voltage. Such a ripple voltage is satisfactory for the design, and requires 4.7 μF capacitors for a 2 μs half-cycle.

2.6.3 Bulk DC Capacitors

As previously discussed, the approach taken during the TETS design was to mitigate axial coil displacement by drastically overshooting the regulator input dropout voltage. The high input-voltage switching regulators are discussed in the next section. In the ICCM design, bulk DC capacitors were used as an additional coil misalignment protection. The idea is that large capacitors will act as a power source during large, short-duration coil misalignments. To size the capacitor appropriately, first order design equations were used.

The energy that must be supplied by the capacitor during a coil misalignment goes as:

$$P\Delta t = \frac{1}{2}CV_{start}^2 - \frac{1}{2}CV_{end}^2 \tag{2.8}$$

On the left hand side of the equation, P is the power required by the implanted system, and Δt is the time over which this power must be supplied (i.e., the time over which the coils are significantly misaligned). On the right hand side, The standard expressions for energy stored by a capacitor reflect the amount of energy that must be supplied to the implanted system by this component. Within this expression, C is the capacitance, and V_{start} and V_{end} are the capacitor voltages at the beginning and end of a misalignment, respectively.

TETS prototyping showed that approximately 20 V could be induced at the rectifier output at around 5-10 mm axial coil displacement. ICCM prototyping showed that the switching regulators dropped out at approximately 7 V. Assuming a 2.5 W system with a 1 s desired holdup time, a 14 mF capacitor would be required. Although such a component could be custom made, the cost/size of such a capacitor was prohibitive for this research. Instead, a smaller, commercially available capacitor was chosen after examining the range of available parts. Ultimately, two 470 μF electrolytic capacitors were chosen, based on size, cost, and availability. The parallel combination results in a holdup time of approximately 66 ms. While this amount of time might easily be exceeded during a very large displacement, it is enough time to smooth the change in voltage brought on by smaller displacements.

An additional consideration for the choice of capacitor was that they are sensitive to input voltage. Although normally a component is selected to tolerate at least two to three times the maximum expected input, the input voltage rating of the capacitors was 24 V. Under ideal circumstances, the capacitors will be operating very near their

rating. It was found experimentally, that when the input voltage is even a few volts over the rating, the capacitors get noticeably hotter. At around 40 V, the capacitors explode. To prevent such a condition, a 24 V zener diode was used to clamp the input voltage.

2.6.4 Secondary Voltage Regulation

The secondary regulation scheme shown in figure 2.10 was chosen to allow high input voltage from the rectifier, and to mitigate switching regulator noise. The parts used in this scheme are described below.

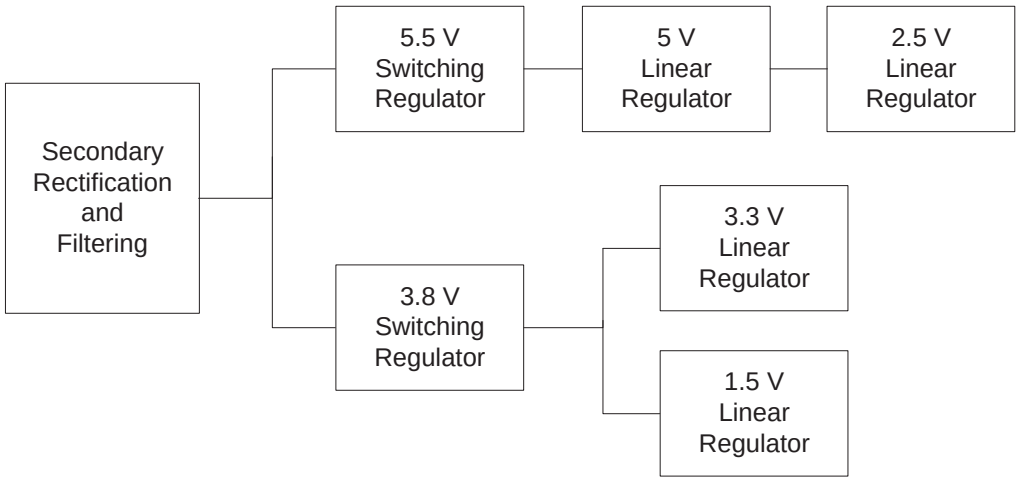

Figure 2.10: Block diagram of the secondary regulation scheme. A key feature of the overall TETS design approach was to use high input voltage step down switching regulators at the output of the rectifying stage. The coil configuration and rectifier were then designed to overdrive the input voltage to the regulators. What is advantageous about switching regulators is that the power across them stays nearly constant. At the input, voltage and current are traded as needed, to maintain constant power. This results in a negative input impedance characteristic. Another notable feature about the scheme is the parallel arrangement of the 3.3 V and 1.5 V linear regulators. This approach was taken to accommodate the power sequencing requirements of downstream digital logic components.

One constraint that was considered during design was power supply sequencing. The FPGA on the ICCM requires that the 1.5 V required for the core logic be established before the 3.3 V I/O voltage. To address this constraint, the 1.5 V

regulator was placed in parallel with the 3.3 V regulator. This arrangement allows the lower-voltage regulator to come up before the higher-voltage regulator. Conversely, the 1.5 V regulator will turn off after the 3.3 V regulator during power down. A trade-off is that the regulator efficiency is decreased, since the input voltage is higher. No such constraint exists for the analog supplies, so the 2.5 V regulator is placed in series with the 5 V regulator.

Switching regulators

Two LT1766 (Linear Technology) step-down switching regulator were used for providing 3.8 V and 5.5 V. This regulator can tolerate input voltages of 5.5 V to 60 V, while providing up to 1.5 A output current. The output voltage is resistor programmed.

A noise reduction feature of the LT1766 is that a synchronization pin is provided on the chip. This feature allows the switching frequency to be modulated by an external logic device. In this design, the two regulators are driven at 250 kHz by the FPGA, once it's fully powered. Noise is reduced by driving the regulators with signals of opposite phase.

Linear regulators

All four linear regulators are LT1962 (Linear Technology) low noise, micropower, low dropout regulators. The device is capable of supplying as much as 300 mA with a dropout voltage as low as 270 mV. The output voltage of each regulator is fixed. The regulator has internal circuitry to protect against reverse current and overcurrent conditions.

2.7 TETS Bench Evaluation

The TETS board, coils, and ICCM were fully constructed according to the above design. The behavior of the complete power supply on the test bench is now described. Where applicable, the TETS was tested with the secondary coil in a 0.9% saline bath. This bath is a good approximation of blood. Compared to other types of tissue, blood tends to have higher conductivity, and thus, acts as a worst-case phantom material.

2.7.1 Regulator Power Consumption

After completely assembling and testing the TETS and 96-channel neural acquisition system, the regulators were metered for current and voltage. This process involved de-soldering the legs of ICs where accessible, and/or bypassing traces on the ICCM board. The results are presented in Table 2.1. The table shows that the rectifier delivers 1.868 W to the input of the regulators.

2.7.2 Regulator input Characteristics

To understand the behavior of the switching regulators used in the secondary, an input I-V curve was developed. The secondary coil was removed from the ICCM. DC power was applied to the common input of the 3.8 V and 5.5 V switching regulator using an external DC power supply. Fluke DMMs were connected to the switching regulators to monitor both input and output voltage and current. The input DC voltage was swept from 2.9-23 V in fine increments. Results are shown in figure 2.11

After the devices enter regulation, the typical negative impedance characteristic of a buck regulator is visible. This characteristic results from the constant power relationship between input and output of a switching regulator. Prior to entering regulation, several current peaks are seen as the 5 V regulator starts up. The behavior of the regulators in this transitional phase of start up can be temperamental,

	Switching Regulators		Linear Regulators			
	5.5 V	**3.8 V**	**5 V**	**3.3 V**	**2.5 V**	**1.5 V**
Input Voltage	9.58 V	9.58 V	5.471 V	3.845 V	4.966 V	3.845 V
Input Current	85 mA	110 mA	147 mA*	156 mA*	1.31 mA*	61.4 mA*
Input Power	**814 mW**	**1054 mW**	**804 mW**	**600 mW**	**6.5 mW**	**236 mW**
Output Voltage	5.471 V	3.845 V	4.997 V	3.305 V	2.521 V	1.505 V
Output Current	147 mA†	217.4 mA†	144 mA	153 mA	1.19 mA	59.8 mA
Output Power	**804 mW**	**836 mW**	**719 mW**	**506 mW**	**3 mW**	**90 mW**
Efficiency	98.8%	79.3%	89.4%	84.3%	46.1%	38.1%
Total Power	**1.868 W**					

Table 2.1: Power requirements for the first generation ICCM and DHSM assembly. Three headstages were connected to the ICCM. Artificial data was collected on 96 channels during a spike detection task. Measurements were taken with a digital multimeter and verified using a current probe and digitizing oscilloscope. Values for input and output power were calculated from the input and output voltage and current of the respective regulator. (*) Derived value. For a linear regulator, input current nearly equals output current. In this case, the data sheet for the LT1962 linear regulator specifies exactly what that difference is at particular loads. The maximum value from the data sheet was added back in as an estimate of the input current. (†) Derived from the input current of the appropriate linear regulator(s).

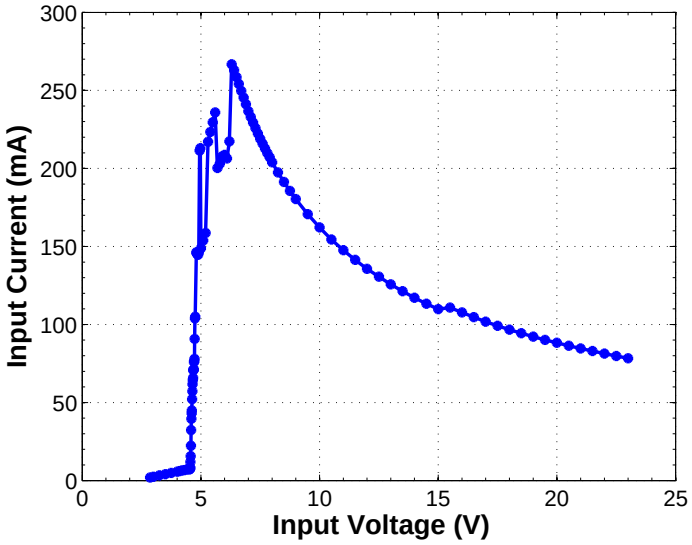

Figure 2.11: Graph of the input IV characteristic of the ICCM switching regulators. A bench power supply was used to finely control regulator input voltage. Input current was recorded with an ammeter. As the input voltage increases, the regulator begins to rapidly enter regulation. In the process, downstream linear regulators and LEDs begin to come online and change the power demands of the switching regulators. Thus, several bumps are apparent during regulator startup. Once the regulation is established, the device exhibits the typical negative impedance characteristic of these types of regulators (the reciprocal of the slope is negative). The maximum input voltage was limited to 24 V, since a zener protection diode was present. The regulator can tolerate as much as 60 V at its input.

especially when the input voltage is varied as slowly as in this case. These peaks were not found in IV curves produced after the rectifier was incorporated.

2.7.3 Coil Axial Misalignment Tolerance

A key measurement in showing that switching regulators are advantageous in a TETS design is the received rectified voltage at the input to the switching regulators. To determine the system's ability to tolerate axial coil misalignment, the secondary was mounted to a micromanipulator, and axial displacement was induced. To model *in vivo* operation, the experiment was conducted in a 0.9% saline bath. The primary was mounted to the underside of a 45×30 cm non-conducting plastic tub, with a wall

thickness of approximately 1 mm. The tub was kept at least 15 cm away from large metal objects, such as the bench support structure. Fluke DMMs were connected to the switching regulators of the ICCM to monitor both input and output voltage and current. The secondary was axially aligned with the primary coil, then lowered until the secondary switchers entered regulation. The secondary coil was then axially withdrawn. A plot of the secondary rectified voltage is provided in figure 2.12.

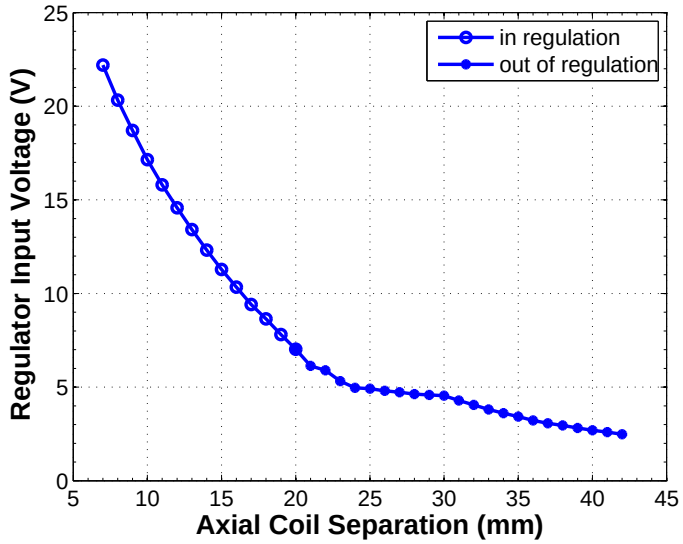

Figure 2.12: A plot of the received rectified voltage vs. axial coil misalignment. The ICCM falls out of regulation when the regulator input voltage is approximately 6.5 V. The last data point on the graph where regulation is maintained is 20 mm, with an input voltage of 7 V.

2.7.4 Coil Radial Misalignment Tolerance

To determine the system's ability to tolerate radial coil misalignment, the secondary was mounted to a micromanipulator, and radial displacement was induced. The same test setup outlined in section 2.7.3 was followed. The secondary was aligned axially with the primary coil, then lowered until the secondary switching regulators entered regulation. The axial separation was varied as previously described, with

the secondary remaining in regulation. At each step, the secondary coil was radially displaced until the dropout voltage was reached by one of the regulators. The coil was then brought back to center, so that regulation was re-established. Figure 2.13 displays the results.

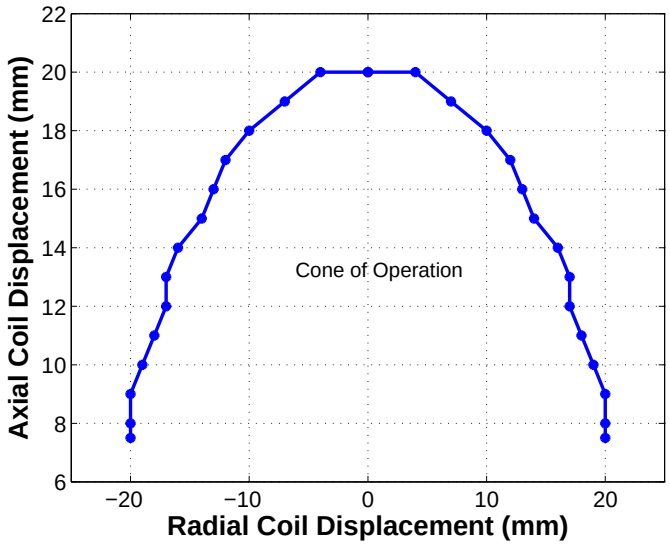

Figure 2.13: A plot of the axial coil misalignment vs. radial coil misalignment. The secondary coil was mounted on a manipulandum connected to a micromanipulator. The coil was submerged in a saline bath. The primary coil was mounted to the exterior of the bath, directly against the wall. Displacements were stepped by 1 mm increments. Data points indicate the furthest position where regulation was able to be maintained (with respect to the coil centers). The thickness of the bath wall and encapsulation were accounted for in the plot.

2.7.5 Reflected Impedance

Although ICCM and TETS prototyping gave a good indication of how the primary circuit reacts to the presence of the secondary, we would now like to compare the results of prototyping with the results of the theoretical analysis presented in section 2.3.2 above.

The first step is to determine the equivalent DC resistor, R_{DC}, shown in figure 2.5. As previously discussed, the value of this resistor depends on coil separation.

Therefore, on a fully-functional ICCM, the switching regulator input and output voltage and current were metered, for both regulators. Three, fully-functional DHSMs were attached, so that the complete acquisition system was powered. The secondary coil was fixed to a micromanipulator and placed in a 0.9% saline bath, as described in section 2.7.3. The axial coil displacement was varied and regulator IV data was recorded. When the coils were close enough that the ICCM was in regulation, telemetry was established to verify that the system was completely operational. From the IV data, R_{DC} was calculated. Equation 2.1 was used to determine the equivalent load resistor representing the combination of R_{DC} and the voltage doubler rectifier. Figure 2.14 shows how the load resistor varies with axial coil separation.

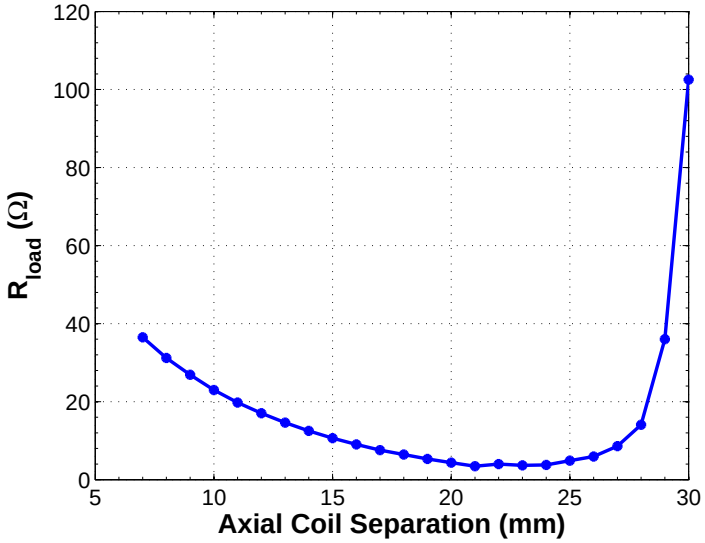

Figure 2.14: Plot of the R_{load} resistor shown in figure 2.5 vs. axial coil separation. This resistor represents the combination of the rectifier, regulators, and other downstream electronics. Data points were determined by measuring the input regulator voltage and current at different coil separations (to calculate R_{DC}), then factoring in the rectifier diode drop (see eqn. 2.1). This explicitly demonstrates the negative impedance characteristic of the switching regulator.

Once the load resistor was determined, equation 2.3 was used to calculate the reflected resistance. The result is shown graphically in figure 2.15.

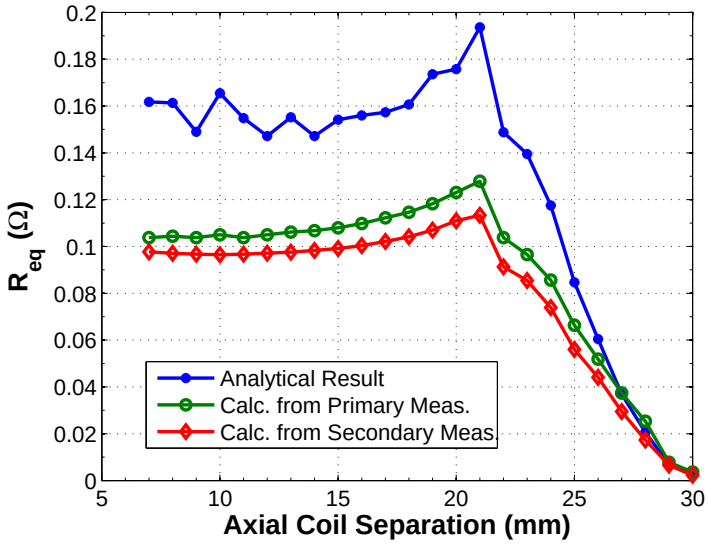

Figure 2.15: Graph of the reflected resistance, R_{eq}. The upper curve was calculated using eqn. 2.3. The middle curve was determined from voltage and current measurements in the primary. Specifically, the current supplied by the primary DC power source was measured both in the absence of the secondary, and as the secondary coil was positioned at different distances from the primary. The ratio of the primary voltage (24 V) to the change in current represents the change in resistance seen in the primary (R_{eq}). The lower curve was produced by measuring the full power requirements of the secondary, and then using rms current in the primary ($P = I^2R$).

In this figure, the predicted resistance and the measured resistance are also presented for comparison. The predicted resistance was calculated using the known power requirements of the secondary and the known rms current in the primary ($P = I^2R$). This resistance is only plotted over coil distances where the secondary is in regulation, since one would not know the unregulated power requirements *a priori*. The measured resistance was calculated from the increased power delivery from the primary DC source, and using the known rms current in the primary (again, $P = I^2R$).

2.7.6 Efficiency

The link efficiency was calculated according to equation 2.6 for axial coil separations up to 30 mm. The results are presented in figure 2.16. The measured values for R_{load} were used in the calculations.

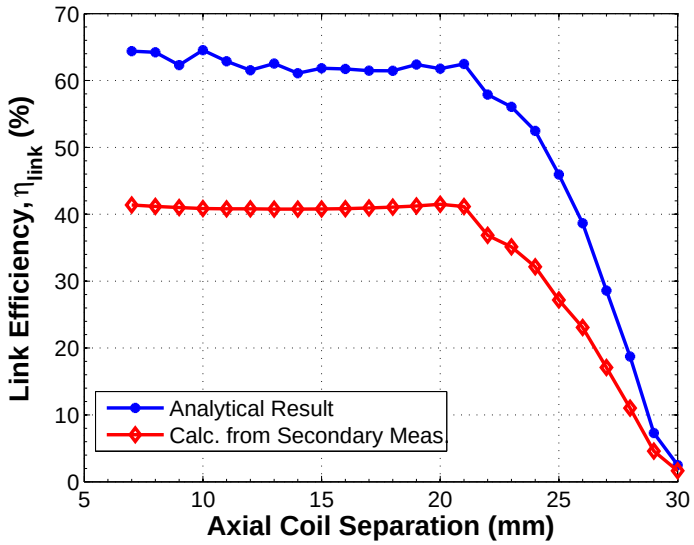

Figure 2.16: Link efficiency curve. The upper curve is the efficiency calculated from the ideal R_{eq} from equation 2.3. Link efficiency was also determined for the R_{eq} calculated from secondary power measurements. This calculation was described in section 2.7.5. As also demonstrated in figure 2.15, the ideal design equations overpredict measured circuit performance.

The DC efficiency was calculated in two ways. First, the DC power consumption of the entire secondary circuit, in regulation, was determined from measurements. The details are described in the next section. The secondary power dissipation was then taken as a ratio over the measured power drawn from the 24 VDC input source. This ratio is referred to as the overall DC-DC efficiency. In this case, the DC-DC efficiency was 24.6%.

Second, with the implanted system in regulation, the DC power consumption after the linear regulators was calculated, based on output power measurements. This

treatment does not count any of the power supply as part of the secondary circuit. Only the parts of the circuit after the regulators are considered. This measure is then taken as a ratio over the measured power drawn from the 24 VDC input source. This efficiency is referred to as the end-to-end efficiency. In this case, the end-to-end efficiency was 16.2%. Each of the efficiencies described above are shown graphically in figure 2.17.

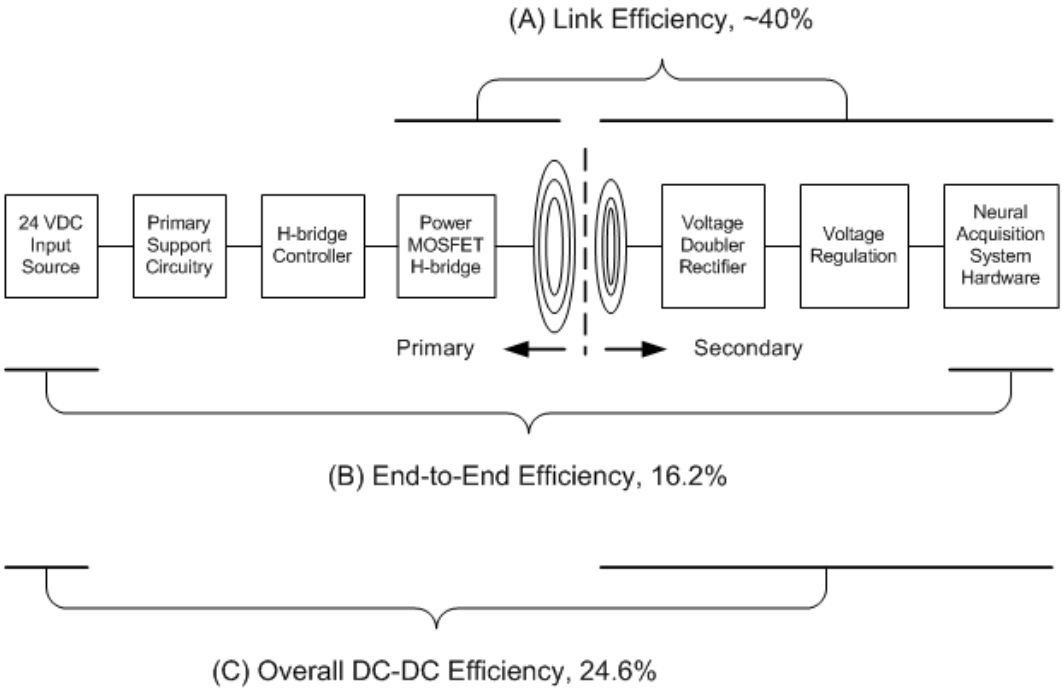

Figure 2.17: Efficiency block diagram.(A) the link efficiency is the ratio of power being received by the secondary to the amount of power being dumped into the reactive portion of the primary switching circuit. As shown in figure 2.16, the designed TETS has nearly constant link efficiency over the entire 2 cm operating range of axial coil displacements. (B) The end-to-end efficiency is ratio of power being delivered to the end application (neural acquisition hardware in this case) to the power being drawn from the primary DC power source. This measure treats the power supply portion of the secondary as a separate entity, not associated with the application. (C) The overall DC-DC efficiency is the ratio of DC power consumed by all secondary components to the power being drawn from the primary DC power source. In this case, the power supply is treated as part of the end application.

2.7.7 Secondary Power Distribution

To compliment the efficiency results, it is also useful to have an understanding of how the power is distributed across all portions of the implanted neural acquisition system. For components that are less power-hungry (e.g., the EEPROM), data sheet values were used to determine expected operating currents. The power consumption of each of these components was then calculated using the expected current and known operating voltage. For the DHSMs and FPGA, voltage and current were measured. For the secondary coil, current was measured, and power was calculated using $P = I^2R$. In this case, because the coil current is sinusoidal, the RMS current was used in the power calculation. Similarly, for the rectifier diodes, RMS current was measured, and the data sheet value for the forward voltage drop was used in the power calculation. Figure 2.18 shows the power distribution for the all of the major components of the secondary. Figure 2.19 shows the power distribution only for components residing on the ICCM (neglecting the DHSMs and secondary coil).

2.7.8 Current Sense Circuit

Another key comparison for verifying current sense circuit theory of operation is the measured and predicted primary DC current. This current is drawn from the TETS primary DC power source (bench supply or batteries). To restate the underlying concept, as the coils are brought in proximity to one another, the primary will begin to deliver power to the secondary. The TETS power supply must compensate for the dissipated power by supplying more current (for a fixed voltage source). Knowing the exact amount of power consumed in the secondary should allow for a close prediction of the increase in primary DC current. An experiment was conducted to prove this hypothesis.

To simplify secondary measurement, a "dummy" load was used in place of the

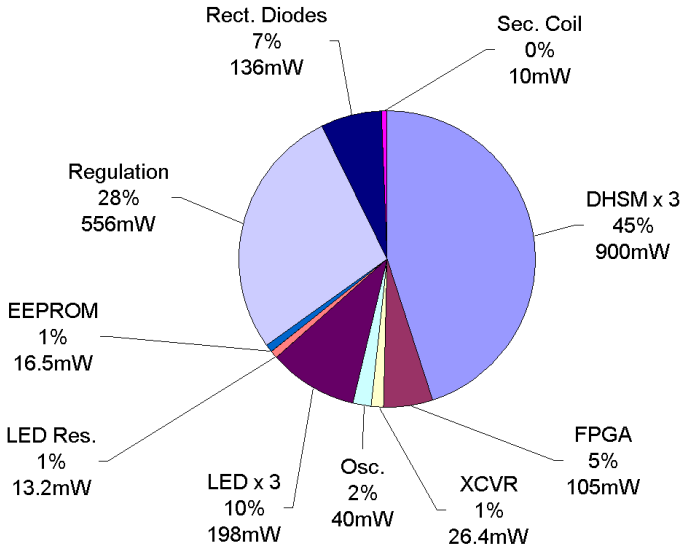

Figure 2.18: Power distribution of the implantable portion of the wireless acquisition system. Total power consumed by these major components and subassemblies is 2.001 W. The percentages represent the proportion of power consumed by each part, out of the total power. The implanted system has a set of six LEDs that are very useful in verifying ICCM operation. Not all of the LEDs are on at once, and those that are on may not be on continuously. In these results, it is assumed that half the LEDs are on continuously. Power is also consumed by the series resistors used in the LED circuit, so those values are also reported. The oscillator and EEPROM are associated with the digital functions of the neural acquisition system. The transceiver manages the wireless communications link.

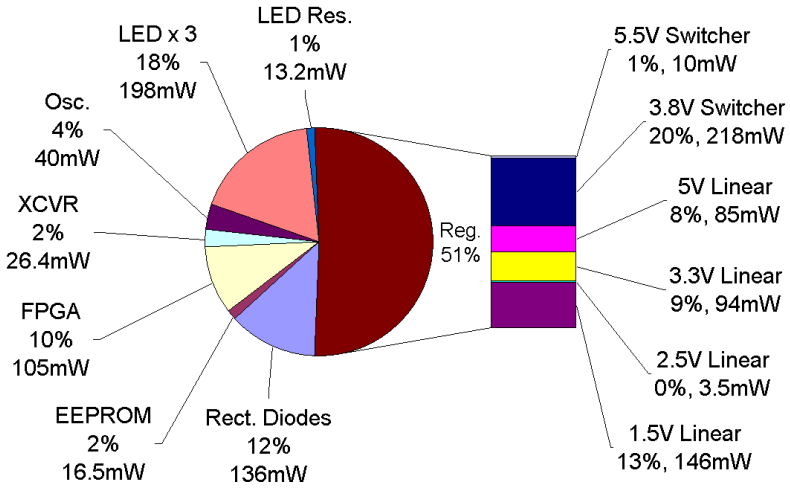

Figure 2.19: Power distribution of just the ICCM components. The total power consumed by the ICCM is 1.092 W. Percentages represent the proportion of power consumed by each part, out of the total power dissipated by the ICCM. The regulators consume slightly more than half of the power.

full ICCM and DHSM assembly. This dummy load consisted of the ICCM switching regulator (LT1766) mounted on a demonstration board. This regulator was attached to an automotive light bulb capable of dissipating more than 2 W. An ICCM board was populated only with the coil input circuit and voltage doubler rectifier. The output of the rectifier on the ICCM board was wired to the regulator input on the demo board.

The TETS primary also consisted of a modified circuit. The board was populated with the H-bridge switching components and the current sense circuit (amplifier and comparator). The electronic circuit breaker, protection diodes, and regulators were not installed. Bench power supplies were used to provide 3.3 V, 12 V, and 24 V. This arrangement allowed the current from each supply to be monitored separately.

With the secondary coil again mounted on the micromanipulator, the coils were axially aligned, and axial coil displacement was induced. Current and voltage input and output were monitored in the secondary while the coil distance was varied in 1

mm increments. Recorded values were used to calculate the total secondary power consumption, including the rectifier and coil ESR. Once the power consumption was determined, the primary DC current was predicted using $P = IV$, for a 24 V system. The result is graphed versus measured primary DC current in figure 2.20 (a).

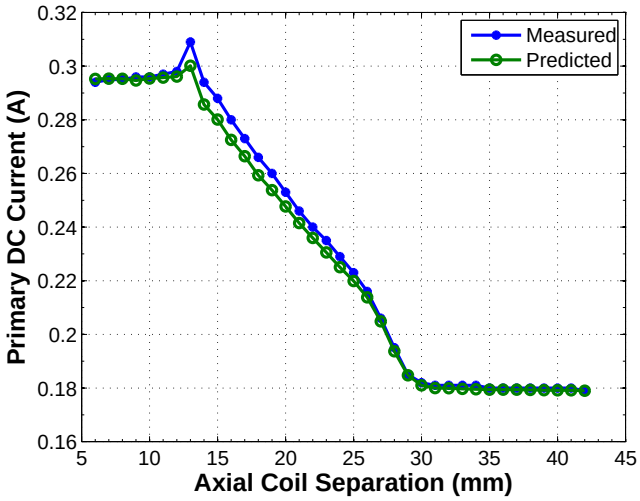

(a)

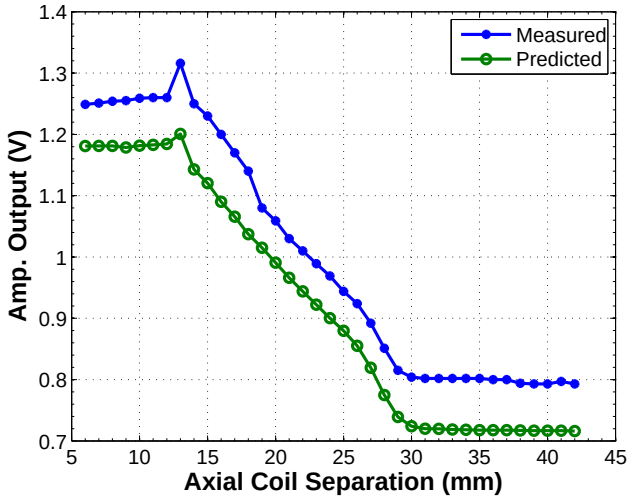

(b)

Figure 2.20: Current sense circuit performance. (a) Measured values represent DC current levels delivered to the H-bridge, through the sense resistor of the current sense amplifier. Measurements were taken with an ammeter. Predicted values were calculated by first measuring the total power consumed by *all* secondary components, including the secondary coil. Using $P = IV$, with a 24 VDC source in the primary, the DC current delivered to the H-bridge was predicted. (b) With a fixed amplifier gain of 40 V/V, The current predicted from graph (a) was used to calculate the predicted output of the amplifier. The measured amplifier output is shown for comparison.

During the experiment, the amplifier output was also monitored using an oscilloscope. The predicted primary DC current was used to calculate the predicted amplifier output, based on the selected gain of 40. The two methods are compared in figure 2.20 (b). The error associated with the amplifier output prediction ranged from 90-95%.

2.8 Discussion

A TETS was designed, built, and fully tested on the lab bench. The results show that the designed H-bridge driver is capable of operating independently of the 2 W secondary load. Another important result is that the presence of the secondary circuit could be predicted based on primary power delivery. These findings are discussed in detail in this section.

2.8.1 Load Independence

Load independence means that the operation of the primary driver is not affected by the presence of the secondary. Whereas the class-E driver uses feedback to vary switching frequency and DC bus voltage, the H-bridge driver designed in this research operates at fixed frequency, duty-cycle, and bus voltage. This topology greatly simplifies driver design, and nullifies the need for in-circuit measurement of secondary voltage or current. In two ways, the results presented in the preceding section indicate that load independence is achieved.

First, the reflected resistance is minimal, as shown in figure 2.15. Measurements indicate that $R_{eq} \approx 100$ mΩ. The ESR of the primary coil (R_{L_1}) is 132 mΩ, and the on-resistance of a power MOSFET (R_{MOS}) is specified at 24.5 mΩ. The $\frac{L_1}{R}$ current time constant is reduced by approximately 5 μs, to around 10 μs. With tuned switching times of 1.85-2 μs, the primary coil current is scarcely effected.

Second, The current amplitude was measured using a clamping current probe. As the secondary entered regulation, the amplitude changed by no more the 150 mA. Considering the amplitude of the coil current was approximately 7.8 A_{peak} without the secondary, a change of 2% can be considered negligible.

2.8.2 Reflected Impedance

Returning to R_{eq}, a noticeable difference exists between the analytical result (from equation 2.3), and the two measured results, in figure 2.15. As a percentage, this difference would seem to be substantial. However, the fact that the impedance can be predicted to within 50 mΩ is actually remarkable. There are a number of factors that could easily account for the difference. The most dominant factor is the coil coupling coefficient, k, which depends on the calculated mutual inductance. The mutual inductance assumes perfectly flat coils that are exactly aligned. If the inter-coil distance is off by even 1 mm, R_{eq} is reduced by approximately 25 mΩ. The mutual inductance calculation also assumes windings that are small and tightly wound. A minor violation of these assumptions would reduce the coupling further. Finally, any increase in R_{load} would also reduce R_{eq}. A 2 Ω increase would reduce it by approximately 10 mΩ. Considering the number of parasitic resistances in the rectifier and coil circuit that are not accounted for in the analytical result, it is likely that R_{eq} could see a decrease of this magnitude.

Along other lines, it was assumed earlier in this chapter that the reactive portion of the impedance could be neglected, leaving only the real part (the resistance). The resonant frequency of the secondary is approximately 242 kHz. At a tuned frequency of 265 kHz, the system operates near resonance, but not exactly so. To verify that the reflected reactance does not significantly alter the primary reactance, Z_{eq} from equation 2.2, was calculated. The maximum reactance was $-j0.065\Omega$. The primary

coil has a reactance of $j3.8\Omega$ at 265 kHz. Thus, the reactance of the primary is altered by less than 2%.

2.8.3 Efficiency

The degree to which the efficiency stays constant was an unexpected finding during this research. It is not a surprising result though, considering the nature of switching regulator operation. These devices are designed to maintain nearly constant power from input to output, drawing only what they need to keep the output at the programmed voltage. They accomplish this task by making tradeoffs between input voltage and current. Thus, it should come as no surprise that the regulator is able to compensate for changes in coil coupling, which has a direct influence on the received voltage.

Comparing the efficiency results of the TETS with other's systems is challenging for a number of reasons. No other system has constant efficiency, so a particular system may perform really well at one distance, but less well at another. In addition, some groups report only link efficiency, rather that overall DC-DC efficiency. Of those that due report overall efficiency, it may be difficult to ascertain whether the regulators are included in the numbers.

2.8.4 Loss

Although the designed TETS can operate for a full 8 hr day from the NimH battery pack, increasing the system efficiency would extend this period, and could decrease battery size and weight. Most of the system loss is experienced in the primary. When the TETS is operating without the secondary, 5.95 W is required by the fully populated driver. As a consequence, of the 8 W consumed when the secondary is energized, 75% is being utilized in the primary.

To determine how the losses are distributed within in the primary, the power consumption of each major component is measured or calculated from data sheet values. The losses attributable to the H-bridge components were isolated by removing the 12 V and 3.3 V regulators and inputting 24 V, 12 V and 3.3 V separately (as described in section 2.7.8). The power consumption of the power MOSFETs, primary coil, and polymer capacitors was 4.32 W. In other words, around 72% of the power losses in the primary, occur in these three component subgroups.

Adding back in the regulators, the measured power delivered by the 12 V regulator is 0.637 W. This value includes every component powered by the 3.3 V regulator, which is downstream from the switcher. At an efficiency of approximately 70%, the power consumed by all 12 V and 3.3 V devices is 0.91 W. So approximately 15.3% of the primary power consumption results from operating these components.

The only major remaining component is the electronic circuit breaker. The power calculated from the data sheet is approximately 0.134 W, or 2.25%. Thus, more than 90% of the TETS primary losses can be accounted for in the major assemblies. Not included in the tabulation are parasitic losses from some of trace resistances that were bypassed during measurement; lossy electrolytic capacitors associated with the 12 V switcher, that were not installed during the measurements; and several voltage divider networks, and the MOSFET associated with the electronic circuit breaker.

The good news is that 72% of the primary losses are in components whose resistance can be reduced by better device selection. For example, larger Litz wire could be used to reduce the coil ESR. Ultra-low on-resistance MOSFETS could be also used (though with some trade-offs). In addition, the losses could be further reduced by using soft-switching techniques [80, 81].

In the secondary, optimization of the power components is also relatively straightforward. An obvious way to increase efficiency would be to simply eliminate 3 of the

4 voltages required by the system. With additional noise filtering, this move could eliminate 5 out of 6 regulators. The diode-based full-wave rectifying scheme could also be replaced with a synchronous rectifier. This circuit uses low-resistance transistor switches that turn on at the beginning of the appropriate phase. Basic synchronous rectifier topologies are available in nearly any solid-state power electronics or power supply textbook, but several good examples can be found in [70].

While these changes may be relatively obvious to identify, their implementation is not at all easy within the context of the 96-channel neural acquisition system. An implanted acquisition system requiring a single supply would require a complete redesign not of the TETS, but of the acquisition system itself. The TETS is impartial to downstream electronics. It only requires a step-down switching regulator at the output of the rectifier. So in this case, the DHSMs would have to be redesigned, and the FPGA would likely have to be exchanged for a custom IC. This process is a major undertaking, which is well beyond the scope of this work.

Chapter 3

Electromagnetics and SAR

In this chapter, we investigate whether the electromagnetic fields generated by the primary coil would expose a human patient to excessive levels of radiation, as defined by the Federal Communications Commission (FCC). We begin with a discussion of these limits, before proceeding with field calculations.

3.1 Guidelines for Exposure to Electromagnetic Fields

The exposure limits for both the field intensities and specific absorption rate (SAR) were presented in chapter 1, section 1.4.3. The details for comparing with these limits are now briefly discussed.

As previously stated, the FCC has established exposure guidelines based on those written by standards organizations. The specific guidelines are available in FCC bulletin 56 [49], and methods for evaluating compliance are available in bulletin 65 [82]. These guidelines exactly match those established by the IEEE [44], with one exception. For the purposes of evaluating electric and magnetic field intensities, the FCC's guidelines do not pertain to signal frequencies less than 300 kHz. The IEEE provides guidelines for signal frequencies as low as 3 kHz. Therefore, in this chapter, the field intensities are compared against the IEEE standard C95.1.

An important exposure limit, common to both organizations, is the specific absorption rate (SAR). This measure is key to understanding how much electromagnetic energy a subject is exposed to. As shown later in this chapter, there is no frequency

dependence for SAR.

In evaluating whether an exposure limit (either a field intensity or SAR) has been exceeded by the TETS, the methods outlined in the above guidelines must be followed. There are two particular methods that apply to this research. First, the root-mean-square (RMS) field intensities must be used for comparison with the published limits. The RMS value is preferred because it represents joule-heating, which is one of the major considerations in the guidelines. As we will see in the next section, the fields are a function of current. The current is a triangular function in time, so the RMS value is the peak current divided by $\sqrt{3}$.

The other major consideration in determining compliance, is that for the field intensities, the spatial average must be used. The spatial average is simply the mean field strength, taken over a vertical cross-section of the human body. Here, that surface is taken to be 2 m by 0.5 m.

3.2 Electromagnetic Field Equations

Near-zone field equations of even a simple circular current loop tend to be quite complex. The classic approach is to first determine the vector magnetic potential ($\mathbf{A}$), then use it determine the electric and magnetic fields. In many analyses, the expression for $\mathbf{A}$ takes the form of an integral that does not have a closed form solution [83, 84]. In this case, computational methods can be employed. In other cases, either far-field or small-loop approximations are used to simplify the integration, or restrictions are placed on the region of integration [83, 85, 86]. However, an analysis has been carried out that produced exact analytical expressions for the radiated fields near the loop, without any restrictions [83].

Within the analysis, the small-loop approximation was compared to the exact solution. It was found that the error in field intensities was less than 5% when the

loop radius is $1/10^{th}$ the wavelength. As will be shown momentarily, the radiated fields are a function of current, and as previously stated, the current through the primary coil is a triangular wave. It is easily shown using Parseval's theorem that approximately 98.6% of the signal power is contained in the fundamental frequency, 250 kHz. Thus, for the purposes of this study, the harmonics can be ignored. The free space wavelength at 250 kHz is around 1200 m. Because the largest primary coil radius is approximately 0.028 m, the small-loop approximation is valid for the calculations at hand. To ensure that this approximation also holds for fields in the body, the wavelengths of various types of tissue were calculated. These values are presented later in this section, with the results of simulation. Before discussing the findings, the field calculation is now introduced.

Because field expressions tend to be so complicated for even simple coil geometries, the approach taken here was to represent each turn of the primary coil as an individual current loop. The geometry between source and field points is depicted in figure 3.1. Note that spherical coordinates are used.

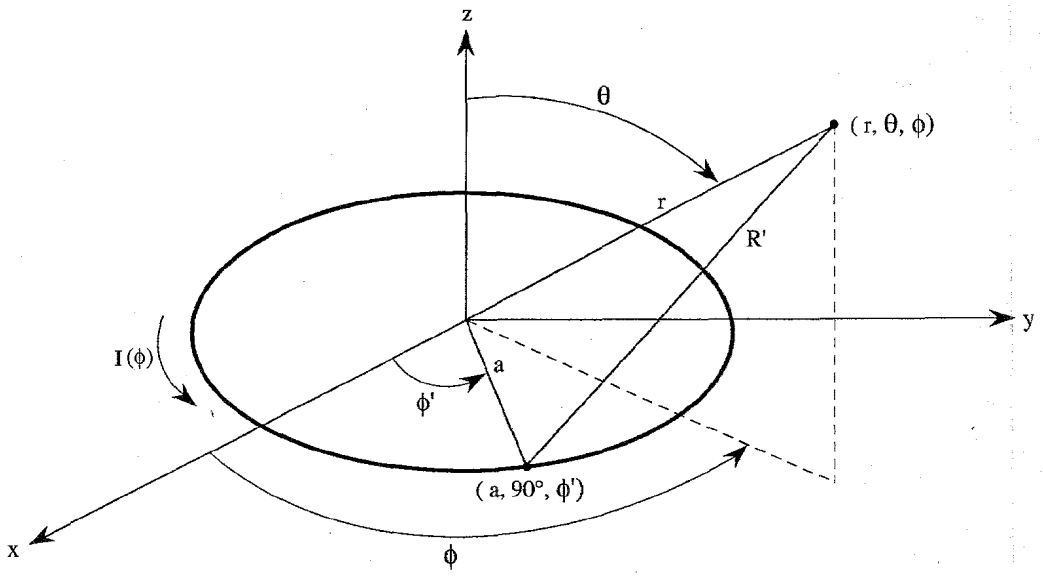

Figure 3.1: Geometry of a circular loop radiator in spherical coordinates (from [83]).

Through the vector magnetic potential, it is shown in [83] that the electric and magnetic fields can be expressed as follows [83, 85]:

$$H_r(r,\theta) \approx \frac{j\beta a^2 I\cos\theta}{2r^2}\left[1+\frac{1}{j\beta r}\right]e^{-j\beta r} \quad \text{A/m} \tag{3.1}$$

$$H_\theta(r,\theta) \approx -\frac{(\beta a)^2 I\sin\theta}{4r}\left[1+\frac{1}{j\beta r}-\frac{1}{(\beta r)^2}\right]e^{-j\beta r} \quad \text{A/m} \tag{3.2}$$

$$E_\phi(r,\theta) \approx \frac{(\beta a)^2 \eta I\sin\theta}{4r}\left[1+\frac{1}{j\beta r}\right]e^{-j\beta r} \quad \text{V/m} \tag{3.3}$$

The geometric components a, r, and θ are described in figure 3.1. The current amplitude is given by I. The phase constant, β, and intrinsic impedance, η, are calculated by:

$$\beta = \omega\sqrt{\mu\varepsilon}\left\{\frac{1}{2}\left[\sqrt{1+\left(\frac{\sigma}{\omega\varepsilon}\right)^2}+1\right]\right\}^{\frac{1}{2}} \quad \text{rad/m} \tag{3.4}$$

$$\eta = \sqrt{\frac{\mu}{\varepsilon}} \quad \Omega \tag{3.5}$$

Both of these constants are functions of the material properties. In these equations, the permittivity is represented by ε (F/m), the permeability by μ (H/m).

3.2.1 Computational Methods

To calculate the total electric and magnetic fields generated by the primary coil, the fields for each of seven loops was calculated, then summed (superposition). The loops were considered to be infinitely thin and coplanar. The radius of the inner loop was 16 mm, the radius of the outer loop was 28 mm. The distance between loops was 2 mm. This distance was used to match the physical dimensions of the actual coil.

Although 14 AWG wire was used, the measured wire diameter was closer to 12 AWG wire. So, the wire centers were taken to be 2 mm apart.

The field equations (eqn. 3.1-3.3) and the loop geometries were coded in Matlab. Because the field is azimuthally symmetric (i.e., not a function of ϕ), a plane in $r\theta$ in any of the quadrants will contain the maximum field intensity. Therefore, field points ranged from the center of the coil outward, in the axial and radial directions. Because the field equations contain a singularity at the origin, fields strengths were examined at distances no closer than 2 mm from the surface of the coil. This distance is appropriate considering that the silicone coating of the actual primary coil is approximately 2 mm thick.

During simulation, spatial step sizes were varied, in order to find the maximum field intensities. Within several meters of the coil, steps of 1 mm were used. Farther from the coil, step sizes of 1 m were used. For the electric field, intensities were quite small and almost completely uniform over the vertical cross-section of a human. Therefore, there was no need to carry out the spatial average, as described above. The peak intensity was compared directly to the exposure limit.

For the magnetic field, the greatest intensities occurred very near the surface of the coil. In addition, the field strength fell off quickly within the first few millimeters. In this case, to accurately assess the exposure the spatial average was carried out. Results for both fields are now presented.

3.3 Field Strength Results

3.3.1 Electric Field Intensity

The maximum electric field intensity was 1.603×10^{-7} V/m, which occurred at $\theta \approx 90°$and $r \approx 450$ m. Because the peak intensity occurs at some distance from the coil, the more restrictive exposure limit for the general population (uncontrolled exposure)

must be applied. IEEE standard C95.1 specifies an electric field intensity limit of 614 V/m, for frequencies from 100 kHz to 1 MHz [44]. Thus, the electric field generated by the coil is substantially less than the recommendation. Although, this field would not be encountered by a subject wearing the TETS primary coil, SAR will be calculated using this result, simply for demonstration purposes.

3.3.2 Magnetic Field Intensity

To determine the magnetic field exposure, the spatial average was carried out. The averaging surface was assumed to be 2 m from the coil surface, as described above. It was assumed that the coil was positioned over the center of the averaging surface. Although in a human, the coil would likely be worn against the upper torso, centering the coil exposes more of the averaging surface to higher field intensities. This approach allows the worst case exposure to be examined.

The spatially averaged magnetic field intensity was 52.3 A/m. IEEE standard C95.1 specifies a limit of 16.3/f(MHz) A/m, for frequencies from 100 kHz to 1 MHz [44]. The limit is 65.2 A/m for a 250 kHz operating frequency. In this case, the magnetic field intensity is approaching the limit, but does not exceed it.

3.4 Specific Absorption Rate

To ensure that the tissue is not being excessively heated as a result of absorbed electromagnetic radiation, the specific absorption rate (SAR) was calculated. An expression for SAR was given by equation 1.2, but is repeated here for convenience.

$$SAR = \frac{\sigma E^2}{\rho} \qquad \text{W/kg} \tag{3.6}$$

To determine SAR, the electric field is used. Established tissue properties can

then be applied to complete the calculation.

3.4.1 Tissue Properties

As previously stated, the SAR calculation depends on two tissue-dependent properties: electrical conductivity (σ) and mass density (ρ). Several authors have reviewed the literature and presented tables of property values for various types of tissue. Values for ρ were taken from [48]. The most widely cited source for electrical tissue properties is a three-part study by Gabriel, *et al.* [87, 88, 89]. (These data are also available via online database [90].) Table 3.1 presents the values taken from these studies for computing SAR.

3.4.2 SAR Results

Results for calculated SAR are presented below. Note that these results are the worst case levels that could possibly be encountered, and that they are many orders of magnitude below the maximum permissible exposure levels. The most restrictive limit provided by the FCC is 0.08 W/kg, for the general population (uncontrolled) receiving whole-body exposure [49].

The wavelength of the field in each tissue type indicates that for the largest loop radius in the primary coil (0.028 m), the small loop approximation holds. Wavelength was calculated using $\lambda = 2\pi/\beta$.

3.5 Discussion

The major finding of this chapter is that the electromagnetic fields generated by the TETS primary coil are within well-established exposure limits. The electric field intensity and SAR are substantially less than the maximum permissible exposure limits. The magnetic field intensity also meets the requirement, but is within approximately 20% of the limit.

It is not surprising that the electric field intensity is so miniscule. The TETS is designed to transfer power by linked magnetic flux. So by the same token, the magnetic field is expected to be significantly stronger than the electric field. Moreover, the geometry of the coil itself would indicate a strong magnetic field. Loops of wires represent magnetic dipoles, which by definition, are very good generators of magnetic fields, and very poor generators of electric fields. So the results presented above make sense fundamentally.

In determining these results, several assumptions were made that require further discussion. First, it was assumed that the maximum electric field intensity was directly applied to each of the tissue types listed in table 3.1. This technique ignores the fact that to reach some of these tissues, the field must pass through different tissue types. As shown in the table, each of these tissues has different permittivities. So at each tissue boundary, a portion of the electric field would be reflected, and a portion would be conveyed. This process would serve to weaken the field actually reaching a particular tissue. However, because the fields strengths were so low, and because this type of analysis is not outlined in the guidelines, it was sufficient to

Tissue Type	**Mass Density** ρ (kg/m^3)	**Conductivity** σ (S/m)	**Permittivity** $\varepsilon_{\mathbf{r}}$	**Wavelength** λ (m)	**SAR** $\times 10^{-16}$ (W/kg)
Blood	1060	1.25 (*)	3662	5.5291	0.101
Bone (cancellous)	1080	0.0378 (*)	334.8	30.51	0.003
Bone (cortical)	1990	0.0305 (*)	208.6	34.29	0.0013
Cardiac Muscle	1060	0.270	6354	10.33	0.0218
Fat	916	0.0263	47.2	38.42	0.0025
Lung (inflated)	260	0.0906	1578	18.58	0.298
Muscle (parallel)	1041	0.566	1001	8.28	0.0466
Muscle (transverse)	1041	0.440	5709	8.69	0.0362
Skin (dry)	1150	0.00217	888.2	39.89	0.0002
Skin (wet)	1150	0.135	9025	11.32	0.0101

Table 3.1: Tissue Properties and SAR. (*) Indicates values measured at 1 MHz (the lowest frequency for which data was available). Wavelength was calculated for each tissue type using $\lambda = 2\pi/\beta$. SAR values were calculated for the maximum rms electric field intensity generated by the primary coil.

simply compare the maximum value against the limit.

The magnetic field does not have the same characteristics as the electric field, as it passes through tissue. The permeability of the body is considered to be that of free space. So to the magnetic field, the body is completely transparent. There is no induced current at tissue boundaries as a result of the magnetic field. In this case, it makes sense to spatially average over a cross-section of the body, and to use the whole body exposure limit.

It should also be noted that a major emphasis by both the FCC [82] and the IEEE [44] is that for distances within 20 cm of the radiating source, the SAR is *the* measure of importance for determining acceptable exposure. This emphasis is driven by the fact that it is difficult to physically measure near-field electromagnetic intensity. With the emphasis placed on SAR for near-field exposure, field strengths that exceed the maximum permissible exposure limits may be acceptable, as long as the SAR level is acceptable.

Finally, in modeling the primary coil, a set of perfectly circular loops was used. As stated above, loops are poor generators of the electric field. There are other aspects to the coil geometry that may result in the generation of additional electric fields. For example, it is not uncommon to consider the feed wires as electric field generators. For a wire loop, two feed wires branch off at nearly 180 °, forming a somewhat awkward electric dipole. However, in the case of the designed primary coil, the feed wires do not branch at 180°when they reach the coil. Referring to figure 2.8, the wires branch in more of a "v" pattern. Furthermore, with a wavelength of approximately 1200 m, the wire isn't nearly long enough or straight enough to form a quarter- or half-wavelength dipole (which would appreciably radiate [85]). The feed wires are also tightly wrapped in a braided ground shield, which would sink any electric field generated by any charge build-up along the length of the wire. It can be concluded,

then, that the coil is the only major electric field generator, and that it has been shown to meet the guidelines outlined above.

Chapter 4

Temperature System Design

This chapter describes the design of a 6-channel digital thermometer for measuring temperatures in the implanted neural acquisition system. The temperature system was designed to plug in to the digital IO connector of the ICCM. It operates from the regulated 3.3 V supply on the ICCM, provided through the connector. The temperature system consists of 6 Wheatstone bridge thermistor circuits, and a commercially available mixed signal integrated circuit (IC). The IC provides amplification and analog-to-digital conversion. Digitized data is retrieved over a serial bus (SPI), which is managed by the field-programmable gate array (FPGA) on the ICCM. Data packets retrieved from the temperature system are combined with neural data packets for wireless transmission out of the body.

The packets are received by the WCM and then routed to a graphical user interface (GUI) for storage and display. The GUI also provides a means of configuring the temperature system. Here, data packets travel in the opposite direction: first to the WCM, then wirelessly to the ICCM. Once received, several modules in the FPGA remove the temperature system packets, which are then sent to the system over the serial bus.

The communication scheme used in this design allows for real time monitoring of implanted system temperatures, on the order of 50 ms. Temperatures from a DHSM, the secondary coil, a reference probe and the surface of the ICCM enclosure were collected during an *in vivo* animal study using this sytem. In this chapter, the details of thermistor selection, IC function, GUI design and calibration are discussed.

4.1 Common Temperature Transducers

The most common types of temperature transducer are the thermocouple, thermistor, and resistance temperature detector (RTD). The advantages and disadvantages of these elements is briefly discussed in the following sections.

4.1.1 Thermocouples

A thermocouple is a junction between two dissimilar metals, that produces a temperature-dependent voltage. This thermoelectric effect is known as the Seebeck effect. In-turn, the Seebeck effect is the sum of two independent effects. The first effect is the Peltier effect: a voltage produced simply by the contact of dissimilar metals and the junction temperature. The second effect is the Thomson effect: a voltage produced by the gradient along each of the conductors [91].

Practical thermocouple operation requires two junctions: one at the temperature of interest, and another at reference temperature (an ice bath classically). The Peltier effect is proportional to the difference between the junction temperatures. The Thomson effect is proportional to the square of the difference between the junction temperatures. The result is that the effect of the lead wires has a greater impact on the temperature measurement than the junction of interest. The leads can be connected to terminals of different metals without affecting the measurement, as long as the temperature is the same at the connection point [91, 92].

There are several standard combinations of metals used in thermocouple thermometry. The more common variety are composed of alloys of copper-nickel (constantan), chromium, iron, and aluminum. These materials result in sensitivities on the order of tens of μV/°C. In general, thermocouples tend to have moderate stability, and can exhibit hysteresis [92]. However, they tend to have very fast response times (time constant as small as 1ms) [91], and can operate over temperature ranges

of -270°C to 2500°C (depending on material). Thermocouple accuracy ranges from 0.5°C to 2°C [92, 16].

4.1.2 Thermistors

There are two types of thermal resistors (thermistors): positive temperature coefficient (PTC) and negative temperature coefficient (NTC). PTC thermistors exhibit an increase in resistance with an increase in temperature. There are two major categories of this thermistor type. The first type are thermally sensitive silicon resistors (silistors). They usually exhibit a relatively small change in resistance with temperature ($\sim 0.77\%/°C$). The other major type is a switching PTC thermistor, which are typically constructed with compositions of barium titanates. This type has a small negative temperature coefficient until a critical temperature (the Curie temperature) is reached. At temperatures greater than the Curie temperature, the component can exhibit changes in resistance of several orders of magnitude over just a few degrees [93, 94].

NTC thermistors exhibit a decrease in resistance with an increase in temperature. These ceramic semiconductors are formed by sintering a mixture of two or more metal oxide powders. They can be formed into a wide variety of very small shapes, such as beads, discs, chips, flakes, and so on [93, 95]. NTC thermistors are relatively sensitive to changes in temperature. The resistance change is typically on the order of 3-6%/°C [16, 91, 92]. They also have very good long-term stability, usually around ± 0.2% of the nominal resistance value per year [91]. Time constants for NTC thermistors range from approximately 0.5-10s, depending on the medium [92]. These devices are considered to have a limited operating range (-50°C to 300°C) [92, 16], but their use for temperatures as high as 1000°C have been reported. The accuracy of this type of thermistor can be as low as 0.01°C over a 10°C span [92].

4.1.3 Resistance Temperature Detectors

Like a thermisitor, a resistance temperature detector (RTD) also undergoes a change in resistance with increasing temperature. Typically, the nomenclature 'RTD' is applied to those devices that are made of platinum. RTDs are known for very high accuracy, stability, and wide operating range (though it is not as wide as thermocouples). RTDs are used for precise measurements over a range of -200°C to 1000°C. They have a sensitivity in the neighborhood of 0.4%/°C, and an accuracy of 0.01°C to 0.2°C [16, 92].

4.1.4 Transducer comparison

The benefits of using a thermocouple as a transducer are that they are inexpensive, readily available, and small. They also have a fast response time. For this application, having a wide temperature range is not advantageous, since the expected temperature will only vary by a few degrees around 39°C. The disadvantages are that they exhibit a very low output voltage, and have very low sensitivity. For a 2°C change in temperature, a typical thermocouple's output would change by approximately 100 μV. This change is on the same order as an action potential! Considering that one measurement of interest is the temperature change of the secondary coil, noise reduction would be a Herculean task. Another disadvantage is that thermocouples aren't all that accurate. The highest accuracies require very rigorous design, and very tight calibration procedures. Even then, the results are modest. Finally, the need for multiple reference temperatures for a multi-channel thermometer would further complicate circuit design.

The benefits of using an RTD is that they are accurate and stable. Again, the wide operating range is not a benefit in this application. One major disadvantage is that RTDs have low sensitivity. While they are not as limited as thermocouples,

the sensitivity is an order of magnitude less than for thermistors. Another issue is that they are not robust to strain and vibration [92]. In an ambulatory animal, this limitation could be difficult to compensate for.

PTC thermistors are also not a practical solution. The silicon-based types don't have enough sensitivity to be useful. The switching types are ideal for threshold detection or in current limiting functions, but are impractical over the limited range a temperatures in the present application. They also tend to be larger than the other transducer types, and are not all that readily available.

On the other hand, NTC thermistors are a practical alternative to both thermocouples and RTDs. The advantages afforded this type of thermistor are that they have superior sensitivity; they are small, relatively inexpensive, and available; they have reasonable response times; and they are stable and interchangeable. They also have suitable accuracy, and can operate over the desired temperature range.

The only major disadvantage to NTC thermistors is the possibility of self-heating. Current must be passed through the component in order to measure its resistance. This current causes power to be dissipated in the form of heat. The subsequent rise in temperature can cause measurement error, or even circuit failure. To counter this effect, the thermistor circuit must limit current through the component. This stipulation is easily addressed with proper design.

4.1.5 Thermistor Selection

The thermistor chosen for this application is the MC65 NTC chip thermistor, manufactured by GE Sensing/thermometrics (St. Marys, PA). This component is resin epoxy coated with heavy isomid insulated lead wires. It is also interchangeable to $\pm 0.05°C$. Table 4.1 lists additional specifications.

The table lists the zero power resistance of the thermistor. This measure is

Sensor Diameter:	1.65 mm max
lead Diameter:	0.1 mm
$R_{25^\circ C}$:	10 kΩ ($\Delta R_T \sim 4\%/^\circ$C)
Dissipation Constant:	Still Air: 0.5 mW/°C
	Stirred Oil: 4 mW/°C
Thermal Time Constant:	Still Air: 8 sec.
	Stirred Oil: 0.5 sec.

Table 4.1: MC65 thermistor specifications. $R_{25^\circ C}$ is the zero power DC resistance measured at room temperature. The dissipation constant is the ratio of the change in power dissipation in the thermistor to the resultant body temperature change.

the resistance of the component at room temperature, with power dissipated by the thermistor low enough that any further decrease in power will not result in more than a 0.1% change in resistance. The zero power resistance is a way of communicating the component's resistance at a given operating point under known conditions. The table also lists the dissipation constant, which is the ratio of the change in power dissipation in the thermistor to the resultant body temperature change. It describes how the temperature of the thermistor itself will increase, based on how much power is being dissipated in the component. Both the dissipation constant and the thermal time constant depend on the thermal properties of the medium. The values given are treated as upper and lower limits.

To calculate the temperature as a function of thermistor resistance, the Steinhart-Hart equation is used [95].

$$\frac{1}{T} = a + b\left(ln\left(\frac{R_T}{R_{25^\circ C}}\right)\right) + c\left(ln\left(\frac{R_T}{R_{25^\circ C}}\right)\right)^2 + d\left(ln\left(\frac{R_T}{R_{25^\circ C}}\right)\right)^3 \qquad (4.1)$$

The constants a, b, c, and d are provided by the manufacturer; R_T is the resistance of the thermistor at the temperature of interest; and $R_{25^\circ C}$ is the zero power resistance. To measure R_T, a complete temperature system was designed.

4.2 Analog and Digital Transducer Circuitry

The heart of the temperature system is the Analog Devices AD7794 (Norwood, MA) This device is a 6-channel, low noise, low power, 24-bit $\Sigma - \Delta$ ADC, with an on-chip multiplexor, buffer, instrumentation amplifier and reference. It collects analog data from a selected temperature transducer circuit, and provides a digital interface for retrieving the data. Each differential input to the device is connected to an individual Wheatstone bridge, which each encorporate one thermistor. The following sections describe the design of one of the temperature channels, and a small portion of the AD7794 feature set. It should be noted that the design of the temperature circuitry did not proceed linearly, in the order described below. Rather, the bridge design necessarily had to account for the AD7794 buffer and amplifier input characteristics. Consultation with the AD7794 data sheet may clarify the design constraints.

4.2.1 Wheatstone bridge design

In order to use the temperature system both at room temperature and in an implanted setting, the bridge circuit was designed to operate the 20-50°C range. To allow for flexibility, an eight element bridge topology was chosen. This allows the user to re-configure the bridge to meet any additional constraints that may arise. The bridge is shown schematically in figure 4.1

The approach was to place the null point of the bridge in the upper half of the 3.3 V full scale range. In this application, the null point (or zero differential bridge voltage) represents the lower temperature range, 20°C. As the temperature increases, the voltage of the thermistor leg will increase beyond the null point. Since the thermistors will be placed remotely throughout the system, large wire loop area will make them susceptible to noise pickup. Keeping the null point of the bridge closer to 3.3 V limits the noise to a small percentage of the signal of interest. However, the

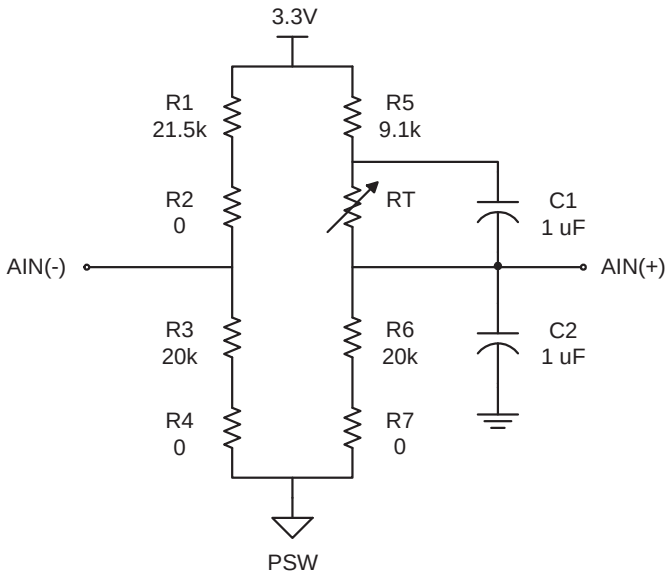

Figure 4.1: Wheatstone bridge circuit for a single thermistor channel. An 8-resistor design was used to allow for flexibility. Capacitors C1 and C2 are included for filtering common-mode and differential noise, respectively. The AIN terminals are inputs to an instrumentation amplifier, described later in this section. Rather than using ground, the bridge is connected to a power switch (PSW), which allows the circuit to be turned off when not in use. This switch is part of the AD7794, which is also described in this section.

input range of the AD7794 buffer and amplifier must also be considered. Because the operating range will be in the upper portion of the 3.3 V scale, lower gains must be used. When gains of 1 or 2 are selected, the input range of the AD7794 is 0.1-3.2 V. When gains of 4-128 are selected, the input range is reduced to 0.3-2.2 V. The null point was chosen as half the maximum input for the low gain settings, or 1.6 V. Appropriate resistor values were chosen, within the constraints of manufacturable values.

As designed, the bridge will produce a maximum differential voltage of 0.418 V. Since the full scale range of the analog-to-digital converter (ADC) on the AD7794 is 3.3 V, a maximum gain of 4 may be used. Over the temperature range 39°C to 42°C, the sensitivity of the bridge is 0.0117 V/ °C.

To combat noise, differential and common-mode filter capacitors were installed at the thermistor input terminals. Because the thermistor changes with temperature, the Thevinin resistance seen by the AD7794 is variable. For a temperature of 50°C, using a 1 μF capacitor (C2) will result in a lowpass cutoff frequency of approximately 9 Hz for the differential filter. Lower temperatures will lower the cutoff frequency. A common-mode filter is formed by a 1 μF capacitor (C1), and the thermistor. The lowest expected resistance, again, occurs at 50°C. For this temperature, the cutoff frequency is approximately 44 Hz. Lower temperatures will also lower the cutoff frequency.

4.2.2 AD7794

As previously stated, the AD7794 is a mixed signal device: one portion of the chip is dedicated to analog amplification; the other portion is dedicated to logic control and digital data I/O. A block diagram is presented below.

The device is configured through a serial digital data interface (I^2C/SPI). A number of features are configurable by the user during operation. This section briefly outlines those features and discusses how the device operates. The reader is referred to the AD7794 data sheet for detailed information.

Analog input

One of six channels is applied to the input of the amplification stage by a multiplexor. The user selects which channel to view by configuring the device through the digital interface (described below). The gain is also digitally selectable by the user. For gains of 1 or 2, the buffer is automatically engaged, and the instrumentation amplifier is removed from the circuit. For all higher gains (4, 8, 16, 32, 64, and 128), the instrumentation amplifier is automatically engaged. The user can select whether

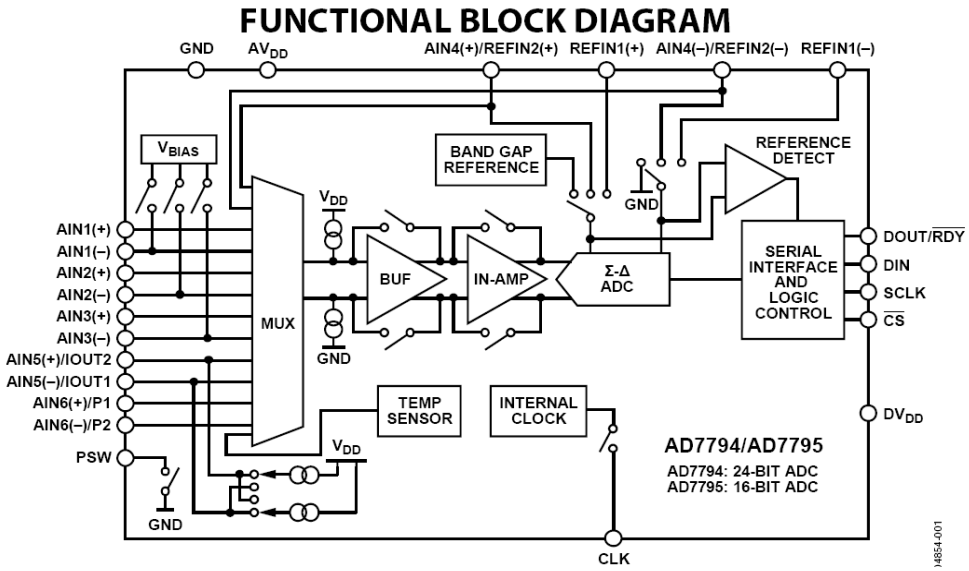

Figure 4.2: Block diagram of the AD7794 temperature system microcontroller (from Analog Devices datasheet for AD7794) A selected channel is first multiplexed to the buffer and amplifier stages. The output is converted to a 24-bit digital signal and stored in an internal register for retrieval.

or not the buffer is also engaged. Another important feature is that the offset is continuously removed by the AD7794, resulting in low offset and offset drift error.

Clock

The device operates from an internal 64 kHz clock. Through internal logic, the clock is available at an external pin. Alternatively, an externally generated clock can be fed in for synchronization.

Internal registers

The only memory on the AD7794 is a set of nine registers. The features of the device are configured by writing to several of these registers. Some of the registers are read only, such as the data register, which holds the digital temperature data. A register can be 8, 16, or 24 bits wide, depending on its function.

Analog-to-digital converter

As described, the device uses a 24-bit $\Sigma - \Delta$ ADC. The update rate of the ADC is user selectable, from 4.17-500 Hz. Depending on the rate, a digital Sinc3, Sinc4, or integrate-only filter is automatically applied. Notches are placed at 50 Hz and 60 Hz.

The ADC has three selectable references: an internal 1.17 V bandgap reference, and two inputs for externally provided references. An external 3.3 V reference was used in this application.

Digital interface and control

Communication with the AD7794 is managed by the field programmable gate array (FPGA) on the ICCM. All communications happen in pairs. First, a write takes place from the ICCM to the communications register, to tell the device whether the next operation will be a read or a write, and which register will be affected. The next transaction completes the cycle. After a cycle is finished, the device waits for a write to the communications register by default. If synchronization with this cycle is broken, the device must be reset.

Transactions take place over the 3-wire serial peripheral interface (SPI) bus. The ICCM masters this bus. It consists of a DIN line for sending data to the AD7794; a $DOUT/\overline{RDY}$ line for retrieving data from the device; and an $SCLK$ line which clocks data in and out of the device. All reads and writes take place with respect to the $SCLK$. This clock is generated by the ICCM. Although the internal AD7794 logic runs on a 64 kHz clock, data can be clocked into or out of any of the registers at up to 5 MHz. For this application, data was clocked at 1.2 MHz (10 cycles of the 12MHz ICCM master clock).

The ICCM manages data retrieval from the AD7794 through a set of control modules written in VHDL. One module interfaces with the receive module of the

telemetry engine, which was also contained in the ICCM. This set of modules routes two incoming 32-bit packets to the SPI module for the appropriate action. The SPI module takes in these packets, carries out the instructions, and outputs any collected data to the transmit module of the telemetry engine. Each incoming 32-bit packet contains an 8-bit instruction header and a 24-bit data section. The header tells the SPI module what operation to carry out: read, write, or continue in the previous state. The data section contains any data that has to be written to the AD7794, as the first half of a paired transaction. The second 32-bit packet has an identical structure, but contains instructions for the second half of the paired transaction.

When a received instruction is a read command, the SPI module reads the data and builds a 32-bit packet for transmission out of the body. The structure of this packet is identical to that of the receive packets. An 8-bit header tells the graphical user interface whether there is valid data in the 24-bit data section, and whether that data is temperature data or other register data (please see section 4.4 for details on the graphical user interface). A second "dummy" packet is hard-coded in the SPI module, so that two 32-bit packets are transmitted out of the body. This second packets contains instructions to ignore the data contained in it. Having two 32-bit packets allowed for symmetry in the WCM/ICCM telemetry packet structure, which ultimately simplified the temperature system interface with the telemetry engine.

Operating modes

The AD7794 has a number of operating modes. The most useful of these are listed below.

- Power Down Mode: all circuitry is powered off.
- Single Conversion Mode: ADC powers up, performs a conversion, sets $DOUT/\overline{RDY}$ low (to signal that a conversion is complete), and returns to power down mode.

Data can be clocked out using paired transactions as described above.

- Continuous Conversion Mode: the ADC continuously performs conversions and sets $DOUT/\overline{RDY}$ low to indicate completion. Data can be clocked out using paired transactions as described above.
- Continuous Read Mode: the ADC continuously converts, but data can be clocked out directly, without paired transactions.

Power switch

A digitally controlled low-side power switch is available at an external pin. The switch can be used to power down the bridge circuits when they are not in use. A maximum of 30 mA can be routed through the switch.

Reset

If communication between the ICCM and the AD7794 becomes asynchronous, or some other error occurs, the device can be reset by writing 32 consecutive ones. The system does not need to be powered down to perform a reset.

4.2.3 Temperature Board Design

Once the temperature system design and prototyping were complete, a 4-layer printed circuit board (PCB) was layed out. The board has two signal layers and two power planes. A split ground plane was used to keep digital signal return paths isolated from the sensitive analog signal lines. Signal traces were 10 mil wide, with minimum 10 mil spacing. Power traces were 15 mil wide. Through-hole connections were provided for attaching thermistor leads. These holes can accommodate up to 28 AWG wire.

The board attaches to the ICCM with a 40-pin, dual-row Hirose connector. This connector provides ground and 3.3 V power to the board. Three pins are used for

the SPI bus and another pin is used for chip select. A fifth pin was connected to the *clk* pin for optional use.

During layout, the board was specifically designed to fit within the footprint of the ICCM. It has a unique shape to allow it to fit around the holdup capacitors, which are the tallest feature of the ICCM. When attached to the ICCM, the board lies directly over two switching regulators. Although tight layout and shielded inductors were used on the ICCM, the bridge circuits were routed on top of the temperature board, to avoid noise pickup from the ICCM's switchers. In addition, several large ground pours were used to provide a low impedance return path for the noise. The finished board is shown in figure 4.3.

4.2.4 Digital Voltmeter

In addition to temperature, another important measure is the received voltage at the input to the ICCM's switching regulators. Although the system does not use this value in its operation, such a measure is an important indicator of system operability. Therefore, one of the temperature channels was converted to a voltmeter. Since the purpose of a Wheatstone bridge is to produce a differential voltage between the legs, converting a channel to a voltmeter simply involved installing the proper voltage divider to ensure adequate dynamic range.

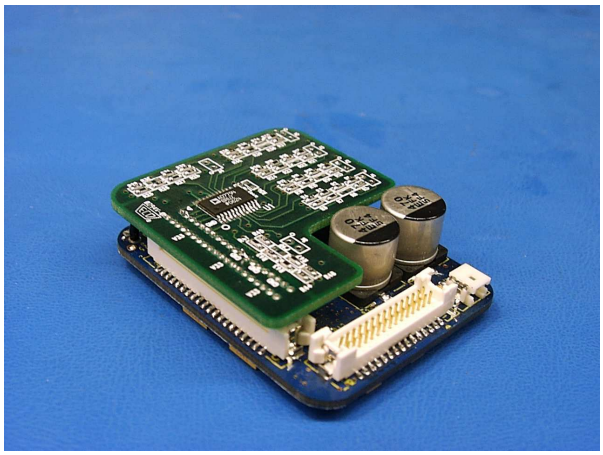

(a)

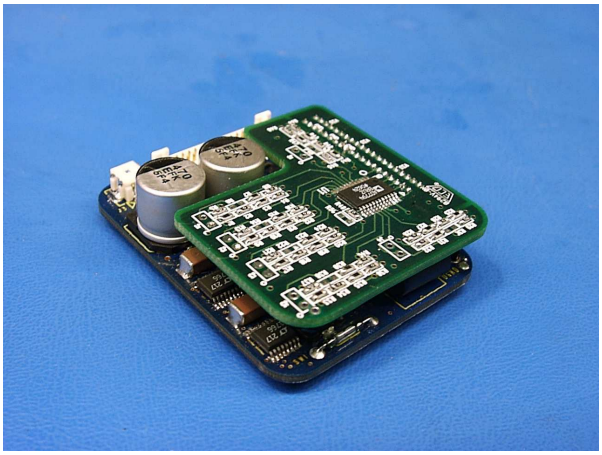

(b)

Figure 4.3: Photographs of the temperature system PCB (green) plugged into the ICCM PCB (blue). (a) The temperature system connects to the ICCM through the 40-pin digital I/O connector, which also provides 3.3 V power and ground. The 30-pin DHSM connector is also visible (with pins exposed). (b) Opposite angle. Through-holes are visible on the closest left edge for connecting thermistor lead wires. Four bridge circuits are prominent in this view. Below this section of the board, on the ICCM, the switching regulator ICs are visible.

Referring to figure 4.1, all resistors in the thermistor leg of the bridge were removed. An 11:1 voltage divider was constructed using a 200 kΩ and a 20 kΩ resistor. For gains of 1 or 2, a maximum input voltage of 35 V can be read by the meter. For a gain of 4, the maximum input voltage is approximately 24 V. There is no minimum voltage input, the device will fall out of regulation before reaching the minimum recommended input of the buffer or amplifier.

4.3 Temperature System Power Demands

A low power temperature system was designed, prototyped and built. To ensure that the operation of this system does not dramatically increase the power demands of the implanted acquisition system, power consumption was considered during design. Current and voltage measurements were taken during prototyping and after PCB fabrication. Prior to installing surface mount bridge resistors, all resistance values were measured. Power consumption in the reference legs of the bridges (AIN(-)) was calculated using measured voltages and resistances. With a bridge reference voltage of 3.301 V, the maximum current drawn by any of the bridge reference legs is 79.4 μA. Power consumption in the thermistor legs (AIN(+)) was calculated based on the highest expected temperature, 50°C. At this temperature, and with a 3.301 V bridge reference, the thermistor leg of the bridge draws approximately 101.2 μA. The maximum power consumption of a single bridge circuit is therefore 0.596 mW. Combined, the six channels consume 3.577 mW.

The power consumption of the AD7794 was also calculated. The input current measured 353 μA, at a voltage of 3.301 V. However, the data sheet lists the maximum possible current as 500 μA. Using this value, the power consumption was calculated as 1.651 mW.

For the entire temperature system, the total power consumption is therefore,

5.228 mW. Assuming a total power delivery of 2 W, the temperature system will increase the secondary power consumption by approximately 0.26%. This increase is negligible.

4.4 Graphical User Interface

An existing LabVIEW graphical user interface (GUI) was modified to extract temperature data from the received telemetry packets. The data is processed and plotted on the GUI front panel for real-time monitoring. The data arrives in the form of differential bridge voltage expressed in 24-bit binary. To obtain the differential voltage in decimal, the following conversion formula was used:

$$V_{diff} = \frac{\left(\frac{binary\ code}{2^{N-1}} - 1\right) \times V_{ref}}{GAIN} \tag{4.2}$$

In this equation, N is the total number of converter bits (24) and V_{ref} is the ADC reference voltage (3.3 V). The gain of the amplifier is also accounted for. With the differential voltage and know bridge resistor values, the thermistor resistance was calculated. Finally, equation 4.1 was used to map the resistance to temperature. For the channel the was converted to a voltmeter, mapping the voltage to a resistance was unnecessary. Figure 4.4 shows a portion of the front panel used for displaying the temperature data.

Another portion of the GUI is used for configuring the temperature system. All the available options are listed in drop-down menus. Menu selections are used to build two 32-bit words. These two packets are transmitted via cable to the WCM, where they are handed to the telemetry engine for transmission to the ICCM. Once in the ICCM, the SPI module carries out the paired transmission protocol previously described. This part of the GUI is shown in figure 4.5.

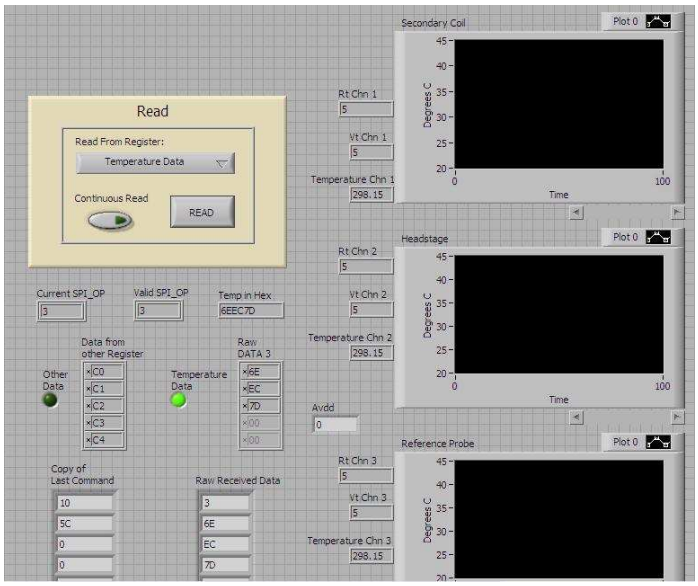

Figure 4.4: Portion of the GUI used for viewing temperature data. Only three of six screens are shown. Several additional numerical displays are used for viewing and interpreting received data.

4.5 Calibration and Uncertainty

Prior to use in sheep studies, both the temperature channels and voltmeter were calibrated.

4.5.1 Voltmeter Calibration

The voltmeter was calibrated by comparing its readout against two Fluke digital multimeters (DMMs). With the temperature system connected to the ICCM, the voltmeter and an external DC power supply were both wired to the input of the switching regulators of the ICCM. Fluke DMM models 87V and 87III were also connected to this input. The DC power supply was swept from 7-23 V. The step size was 0.25 V from 7-9 V, and 0.1 V from 9-23 V. The input voltage did not exceed 23 V because a 24 V zener protection diode was installed on the ICCM. Telemetry was established between the ICCM and WCM on the test bench. Voltmeter readings

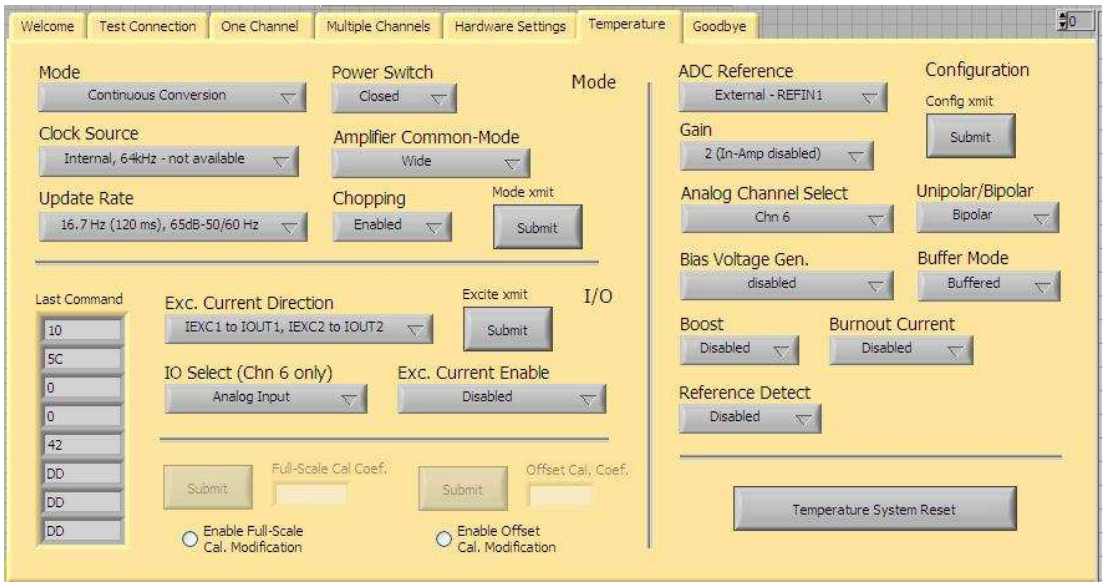

Figure 4.5: Portion of the GUI used for configuring the temperature system. A number of options are available in drop down menus. These options are used to build two 32-bit words, for paired communication between the ICCM and the temperature system.

were recorded using the GUI.

The collected data were loaded into Matlab and a linear regression analysis was performed. The two DMMs had identical readings. Using the voltmeter data as a dependent variable and the DMM data as an independent variable, a first order polynomial was fit to the data. An expression for the best fit line was produced.

$$V = 1.0008(V_{meas}) - 0.0177 \tag{4.3}$$

Where V is the approximation of the true voltage, and V_{meas} is the reading produced by the voltmeter. The correlation coefficient, or r-value, was 0.99999976. The mean-squared error (MSE) was 9.184×10^{-6}. These results show excellent agreement between the voltmeter and the DMMs. A plot of the data is shown in figure A.1 in Appendix A.

4.5.2 Thermistor Calibration

After the thermistors were installed at the desired location in the implanted acquisition system, each temperature channel was calibrated using a VWR Scientific model 1166 water bath. The bath was filled with de-ionized water, and was continually stirred. The temperature system was installed on the ICCM. With thermistors attached, the secondary coil, DHSM, reference probe and two halves of the ICCM enclosure were placed in the bath (the placement and packaging of the thermistors is described in section 5.2). The system was energized and telemetry was established between the ICCM and a WCM. The temperature was swept from 36°C to 44°C, in steps of 0.5°C. Temperatures were collected using the GUI.

A calibrated thermometer was not available to compare the recorded temperature data against. Instead, a Cole-Parmer (Vernon Hills, Il) model 93210-50 digital thermometer was used. The thermometer has a resolution of 0.01°C, and an accuracy of ±0.03°C. A jack on the thermometer allows for different temperature probe styles to be used. A 400 series probe was used for calibration. This probe consists of a thermistor in a Pyrex glass sheath. The accuracy of the probe is ±0.1°C.

A second, identical digital thermometer was also calibrated for later use during sheep studies. Rather than the larger 400 series probe, a YSI 554 probe was used. This 1 mm, Teflon-coated catheter probe has an accuracy of ±0.1°C. Although the probe is fully compatible with the thermometer, the manufacturer provides a calibrated conversion table, for correcting the temperature readout. Linear interpolation is recommended. The tabulated conversion data was loaded into Matlab, and a line was fit.

Uncertainty in commercial digital thermometers

The amount of uncertainty in the reference temperature was calculated using the probe and thermometer uncertainties provided by the manufacturer. The uncertainty of the digital thermometer unit was ±0.03°C, independent of the probe. The uncertainty of the 400 series glass probe was ±0.1°C. The 95% confidence limit uncertainty for the reference temperature is:

$$\sigma_{ref} = 2\sqrt{0.1^2 + 0.03^2} = 0.209°C \tag{4.4}$$

Because the uncertainties in the second digital thermometer and smaller 554 probe are identical to the reference thermometer and glass probe, the 95% confidence limit uncertainty for this unit is also ±0.209°C.

Uncertainty in temperature system thermometers

The uncertainty for each temperature system channel is determined through the water bath calibration procedure. All probes were placed in the bath and the temperature was swept, as described above. The data for each channel was fit to the reference thermometer readings using a linear least squares fit routine (Matlab). The best fit line, mean-squared error (MSE), and correlation coefficient (r) were generated. Data from the second digital thermometer and 554 probe were also fit to the reference thermometer data. (This data had to undergo two linear transformations: one to compensate for the 554 probe, another to be able to compare the reading to that of the reference probe.) Table 4.2 presents the results from the least squares fit.

The least squares fit provides a way to map thermistor temperature readings to the digital reference thermometer. It is necessary to quantify the total uncertainty associated with a given reading. There are two sources of uncertainty associated with a measurement. The first source is the reference thermometer, which has already been

Sheep study	Best fit line	MSE	r
Channel 1			
5	1.006(T_{th}) - 0.3165	1.499×10^{-5}	0.999999
6	1.013(T_{th}) - 0.3776	6.053×10^{-5}	0.999995
Channel 2			
5	1.006(T_{th}) - 0.3075	4.250×10^{-5}	0.999996
6	1.007(T_{th}) - 0.1396	4.136×10^{-3}	0.9997
Channel 3			
5	1.013(T_{th}) - 0.4928	5.568×10^{-5}	0.999995
6	1.018(T_{th}) - 0.3906	3.940×10^{-4}	0.99997
Channel 4			
5	1.023(T_{th}) - 0.6208	3.029×10^{-5}	0.999997
6	1.025(T_{th}) - 0.3683	6.350×10^{-4}	0.99995
Channel 5			
5	1.005(T_{th}) - 0.2488	1.820×10^{-5}	0.999998
6	1.015(T_{th}) - 0.3048	1.120×10^{-3}	0.9999
554 probe and thermometer			
5	0.9982(T_{th}) - 0.04810	5.305×10^{-5}	0.999996
6	0.9989(T_{th}) - 0.09392	6.200×10^{-5}	0.999995

Table 4.2: Thermistor calibration data.

described. The second source consists of both the dependent and independent uncertainties that exist throughout the temperature system hardware. These uncertainties are compensated for by way of the linear mapping. However, the mapping does not perfectly fit the thermistor data to the reference thermometer data. The remaining uncertainty is therefore manifest in the mapping error. The following description outlines this error.

$$T = a(T_{th}) + b + \epsilon \tag{4.5}$$

Where, T is the approximation of the true temperature, a and b are the coefficients

from the linear least squares fit, and ϵ is the total uncertainty. The two sources contributing to the total uncertainty are independent, so ϵ is obtained as follows:

$$\epsilon = \sqrt{\sigma_{ref}^2 + \sigma_{LLS}^2} \tag{4.6}$$

Where θ_{ref} is taken to be half the 95% confidence limit value, and θ_{LLS} is the uncertainty from the linear least squares fit. As described in [96], a common way of expressing uncertainty is as a percentage of reading. The largest deviation from the least squares line can be taken as a bound on the uncertainty. This deviation was determined for each of the calibrations described in table 4.2. Maximum values, and maximum percent error associated with that value, are shown in table 4.3.

The last column in the table displays the accuracy of a channel for a given experiment. The maximum deviation from the least squares line, $\sigma_{LLS\,max}$, is combined with the uncertainty of the reference probe, to produce the 95% confidence interval uncertainty, $2\epsilon_{max}$. The maximum percentage deviation associated with the $2\epsilon_{max}$ uncertainty is then calculated.

Sheep study	$\sigma_{\text{LLS max}}$	$2\epsilon_{\text{max}}$ (95% C.I.)	Max % of Reading
Channel 1			
5	0.00805°C	0.0621°C	0.170%
6	0.0184°C	0.0704°C	0.174%
Channel 2			
5	0.0175°C	0.0695°C	0.190%
6	0.172°C	0.348°C	0.860%
Channel 3			
5	0.0157°C	0.0677°C	0.185%
6	0.0392°C	0.0988°C	0.244%
Channel 4			
5	0.00861°C	0.0624°C	0.171%
6	0.0584°C	0.131°C	0.324%
Channel 5			
5	0.00793°C	0.0621°C	0.170%
6	0.0821°C	0.175°C	0.430%
554 Probe and Thermometer			
5	0.0139°C	0.0661°C	0.181%
6	0.0139°C	0.0661°C	0.163%

Table 4.3: Thermistor uncertainty. The $\sigma_{LLS\,max}$ column displays the maximum deviation from the linear least-squares line. The $2\epsilon_{max}$ column displays the 95% confidence interval uncertainty. Values in this column account for $\sigma_{LLS\,max}$ and σ_{ref}, per equation 4.6. The last column displays the maximum percentage of the reading associated with the $2\epsilon_{max}$ uncertainty. Values in this column represent the accuracy of each temperature system channel, for a given experiment.

Chapter 5

Evaluation

5.1 Overview

The efficacy of the transcutaneous energy transfer system (TETS) was evaluated during six *in vivo* sheep experiments. The TETS and temperature system were fully fabricated and tested on the lab bench, as described in chapters 2 and 4, respectively. These two systems were then tested with the complete 96-channel neural acquisition system, to ensure that is was fully functional.

A total of six acute sheep studies were carried out with the complete system. The experiments took place in the operating room while the animal was fully anesthetized. Prior to each experiment, the implanted components of the system were packaged in biocompatible material and tested in a saline bath. For each animal study, the acquisition system was successfully powered, and was able to perform all neural data processing functions. The temperature of the implanted components was also monitored in real-time. Results show that when the DHSM and ICCM are implanted at reasonable depths in the tissue, the temperature rise can be reduced. This chapter presents the details of the system preparation, implant surgery, and *in vivo* test results.

5.2 Packaging

Prior to implantation, the entire system was packaged for operation inside the body. The following sections outline how each component was prepared.

5.2.1 Electrodes

Electrode arrays were hand-assembled from 30 μm and 50 μm diameter tungsten wires. Electrode shanks were 2 cm, 2.5 cm, and 3 cm long, to correspond to the desired cortical depth. The electrodes were insulated with polyimide, which was removed at the tips when the electrodes were clipped to length. Since the three DHSMs are placed near the craniotomy on top of the skull, a short cable was needed to connect each array to its headstage. Cable lengths ranged from 2.5 cm to 3.5 cm; all cable diameters were 0.94 mm. The outer sheath of the cable was medical grade silicone tubing. Each cable terminated into a small printed wire board, to which a 36-pin, dual row Omnetics nano connector was attached. This allowed an array to be plugged into a DHSM. Once the array was plugged in, a final coating was applied to seal the connector and any remaining seems. Please see section 5.2.2 for further details. A photograph of a electrode array is presented in figure 5.1.

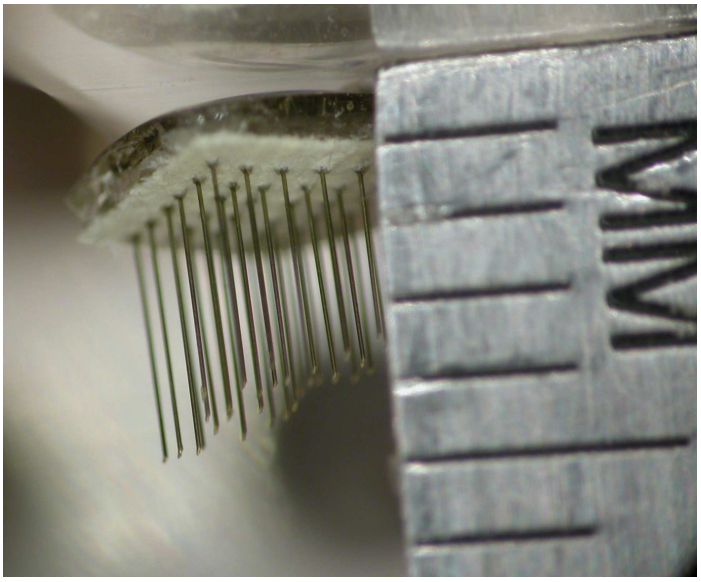

Figure 5.1: Photograph of a single 32-channel electrode array.

5.2.2 DHSM

Each DHSM was built on a flexible circuit board to minimize overall thickness. Excessive flexation can cause vias and pads to become disconnected. Therefore, the boards needed to be both ruggidized and sealed against fluid. Resin epoxy was chosen for this purpose. Before coating each DHSM, the ICCM cable connectors were removed, and the cables were soldered directly to holes in the boards. The electrode connector was left in place, so that each DHSM could be used on multiple sheep (the electrode arrays are not reusable, and needed to be discarded after each experiment). For one of the headstages, a bead thermistor was placed directly against the board, between the analog ICs, for temperature measurement.

Once the boards were prepped, each DHSM was coated with a layer of Loctite Hysol epoxy (Henkel, Dusseldorf, Germany) on each side. All electronic components were completely encapsulated by the Hysol. The epoxy also covered the through-hole cable connections, and overlapped part of the electrode connector. Once coated, the DHSMs were cured at 60°C.

With the electrodes attached, a fine layer of flowable silicone adhesive (permatex) was then poured over the epoxy layer, electrode cable connector, part of the electrode cable, and part of the ICCM cable. For some of the later experiments, a bead thermistor was placed against this outer silicone layer, above one of the analog ICs. This thermistor was soldered to a pair of wires in the ICCM cable, and was held against the headstage using a very thin coating of the same adhesive. The soldered connections at the ICCM cable were also sealed with the silicone adhesive. Figure 5.2 shows a finished DHSM subassembly with bead thermistors.

Figure 5.2: Photograph of DHSM packaged for an *in vivo* experiement. In the center of the board, the two analog ICs are visible, covered in copper foil for noise reduction. A thermistor is present over one of them at the outer epoxy surface. The lead wires are also visible. These wires make their way into the DHSM cable, out of the picture to the left. Also note the omnetics electrode connector and electrode cable to the right.

5.2.3 Secondary Coil

Surgical mesh was used as a substrate for packaging the coil and magnet together. This mesh was 610 μm thick, and made of polypropylene. The coil and magnet were first placed on a small circular section of the mesh. Two thermistors were placed within the subassembly: one was placed on the magnet, the other was placed in contact with the windings of the coil. Lead wires were routed down the exterior of the shielded coil cable, underneath the medical grade silicone tube. The coil was then encapsulated with A-103, MDX4-4210 platinum cure silicone elastomer (Factor II, Lakeside, AZ). The subassembly was cured at 60°C. As needed, both flowable RTV silicone and Med2-4213 adhesive silicone (Nusil, Carpinteria, CA) were used for sealing seams and voids.

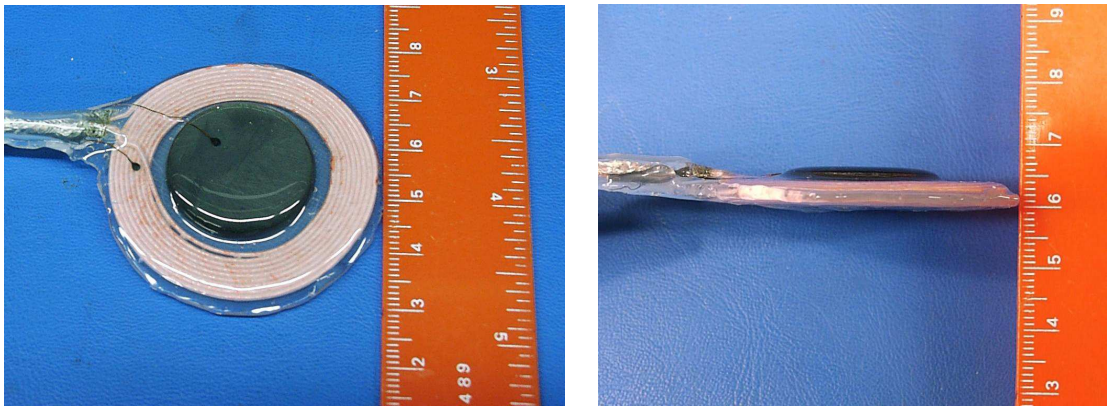

(a) (b)

Figure 5.3: Photograph of secondary coil prepared for implantation. (a) Two thermistors are visible: one on the magnet, one on the coil windings.(b) A profile of the secondary coil. This coil was used in sheep study 6. A similar technique was used to prepare the coil in previous studies. (The scale has units of mm.)

5.2.4 Reference Temperature Channel

In order to measure the change in surface temperatures, one channel of the temperature system was used as a reference channel. A probe was constructed to house the thermistor and leads. The leads were 28AWG stranded wire, and were attached to the thermistor via soldered connection. The probe was encapsulated in two diameters of medical grade silicone tubing. The tip of the probe was filled with Med2-4213 adhesive silicone, as a barrier against leaks, and for flexibility. Figure 5.4 shows the finished probe.

5.2.5 DC power-in cable

To ensure that noise generated by the TETS does not hinder the ability of the neural acquisition system to collect and extract spikes, a DC power-in cable was added. This cable connects to the acquisition system at the input to the switching regulators. Since TETS-generated noise is eliminated when a DC source is used, the RMS noise of each channel can be compared between the two power supply options. Because the

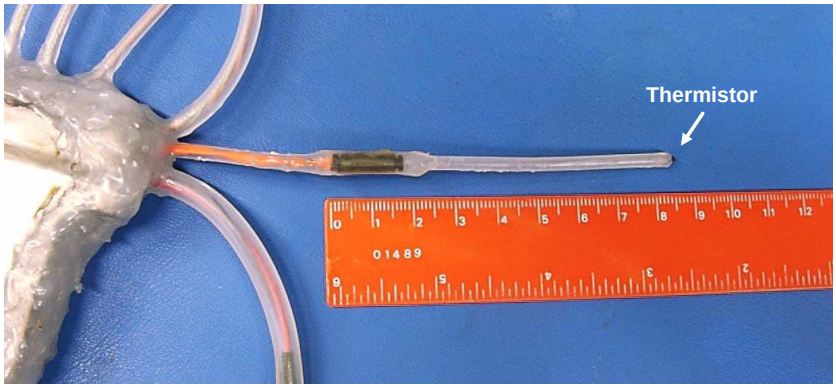

Figure 5.4: Photograph of reference temperature channel used by the temperature system. The thermistor is at the tip of the probe, near the right edge of the photograph.

cable is percutaneous, it must be appropriately sealed; medical grade silicone tubing was used for this purpose. A connector is used at the end of the cable to plug in the DC source. This connector is initially sealed with Med2-4213 adhesive silicone so that the cable can be tucked into a pocket in the tissue until needed. The cable is then brought out from the pocket, the sealed end is clipped, and a DC power supply is plugged in.

5.2.6 ICCM Cabling

The outer sheath of all cables was medical grade silicone tubing. This tubing can be sealed at the ends with medical grade silicone adhesive. Table 5.2.6 lists the specifications of each cable.

5.2.7 ICCM

After all subassemblies and cables were encapsulated, the ICCM and temperature system were packaged in a titanium defibrillator enclosure (herein referred to as the Can). Several holes were first drilled in the Can for cable egress. A bead thermistor was attached to the interior of each half of the Can, and fixed in place using epoxy.

	Number of Cables	Number of Conductors	Ground Shield	Diameter
ICCM-DHSM Cables:	3	30	3	3.175mm/9.525mm (each)
Telemetry Antenna:	1	2	coax	3.175mm
Secondary Coil:	1	6	1	4.88mm
Thermoprobe:	1	2		3.175mm/4.88mm
DC power-in Jack:	1	2		6.35mm/9.525mm
TOTAL:	7	42	4	

Table 5.1: Cable Specifications. In cases where 2 diameters are given, the number on the left represents the typical cable diameter, the number on the right represents the diameter of the largest part of the cable. For example, the DHSM cable is as large as 9.525 mm at the connector, but the cable itself is much smaller. For the secondary coil, the conductor count reflects the addition of two leads for each of two thermistors. The lead wires were 30AWG stranded copper.

Lead wires were connected to the temperature system. A 2.5 V AC ground wire was spot welded to the interior of the Can, and connected to the ICCM at an appropriate terminal. A small amount of epoxy was as added to reinforce the weld. A picture of the system just prior to enclosure is shown in figure 5.6. To further protect the electronics against leaks, before the ICCM and temperature system was sealed in the Can, the subassembly was bundled in a nitril envelope.

The surface of the Can was prepared before applying sealant. First, a wire brush was used to abrade the surface of both halves of the Can near the seam. A lint free cloth and de-ionzed water were used to clean any metallic residue left from this process. The surface was then cleaned with a lint free cloth and rubbing alcohol, followed by acetone. Finally, the surface was treated with Med-163 silicone primer (Nusil), to increase the effectiveness of the silicone adhesive. With the ICCM inside and cables appropriately routed, the Can was clamped in a vice. Clear RTV silicone adhesive sealant (Permatex) was applied over the seam, in sections. Between sections, the adhesive was cured at 60°C. To prevent inward pressure during *in vivo* operation, the final section was applied at room temperature. This approach will result in an outward pressure as the electronics heat the enclosure. To further minimize the

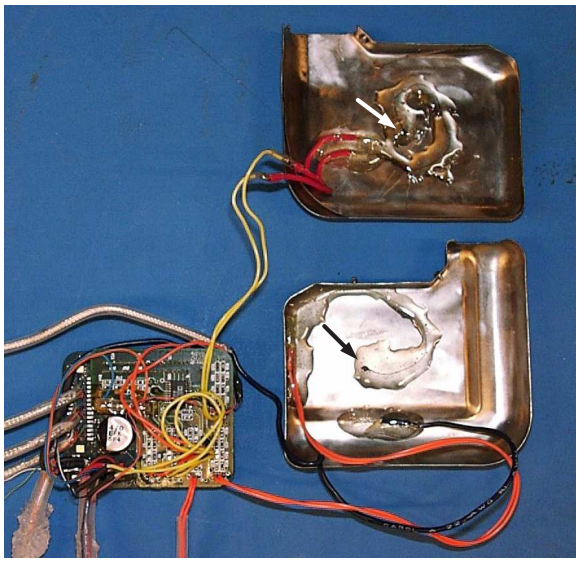

Figure 5.5: Photograph of the ICCM with temperature system attached, and the two halves of the titanium enclosure (Can). In the upper half of the Can (the lid) a white arrow indicates a thermistor. In the lower half of the can (the base) a black arrow indicates the other thermistor. Also in the lower half, a 2.5 V AC ground wire (the dark wire) is spot welded to the interior. A small amount of epoxy reinforces the weld. In the lower left, the ICCM has the temperature system attached and thermistor leads connected.

possibility of leaks, a final thin coat of flowable silicone adhesive was applied over the sealant, to fill small seams an voids. A photograph of the finished system is presented in figure 5.6.

5.2.8 Final Testing

With the implanted components fully sealed, the acquisition system was tested in a 0.9% saline bath. All components were completely submerged for a period of no less than three hours. The DHSM connectors were left out of the bath, since they remain unsealed until implant. The secondary coil was mounted against the inside of the bath's plastic wall, below the water line. The primary coil was mounted opposite the secondary coil, on the exterior of the bath. With this configuration, the system could be energized throughout the testing.

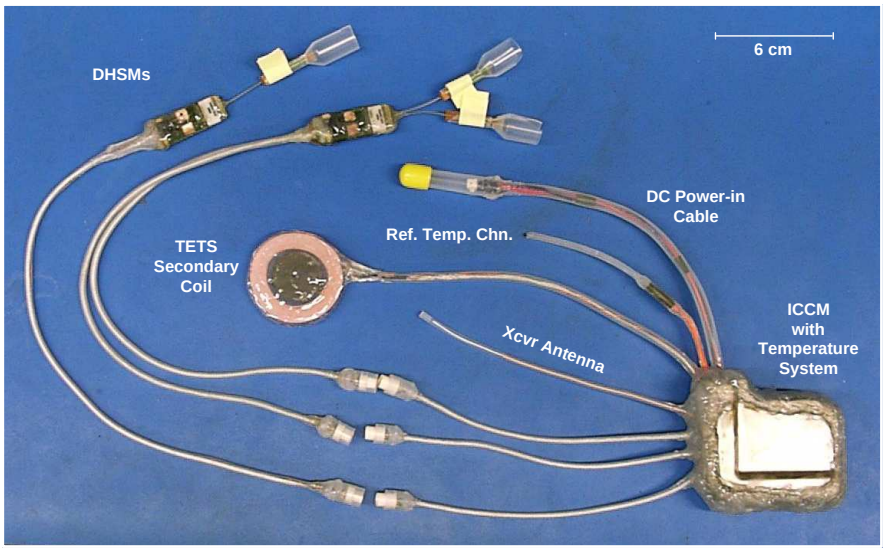

Figure 5.6: Photograph of the entire 96-channel wireless acquisition system, fully packaged for implant. Notice that two DHSMs have been stacked and encapsulated as a single unit.

The performance of the acquisition system was informally evaluated by monitoring its ability to acquire and telemeter an injected test signal. The signal was induced in the bath using two electrodes and a signal generator. Two types of signal were used during these tests. The first was a variable amplitude, 1 kHz sine wave (the amplitude was adjusted to limit DHSM amplifier saturation). The second type of test signal was a variable amplitude, 60Hz square pulse, with a pulse width of 340 μs. These signals provided a quick verification of the system's functionality.

Such testing was conducted prior to each of the acute sheep studies. In every instance, at least one compromise in the packaging was discovered. A common point of failure in the DHSMs was at the electrode connector. Repairs were usually made by applying additional silicone adhesive. On several occasions, major leaks were also detected in the ICCM enclosure sealant. Repairs were made by completely disassembling the enclosure, cleaning off the original layer of sealant, and repeating the process described in section 5.2.7. Because saline was used in the bath, whenever

a leak occurred, the ICCM electronics were usually damaged in some way. Damage ranged from corrosion on power pins, to major destruction of circuit traces and components. In all cases, appropriate repairs were made, and all system components were fully re-tested, before resealing the enclosure. Once resealed, the system was placed back in the saline bath, as time allowed.

5.3 Implantation Procedure

The implantation procedure was performed in compliance with a protocol approved by the Duke University Institutional Animal Care and Use Committee. A total of six sheep (Ovis Aries) were implanted over a period of 6 months. All studies were acute, non-survival procedures, which took place during the span of a day. A brief overview of the surgical procedure follows.

Twenty-four hours prior to surgery, the back of the sheep's neck was shaved and a Fentanyl patch was applied (100 mcg/hr). On the day of surgery, the animal was sedated with ketamine hydrochloride (15-22 mg/kg IM) and anesthetized with isoflurane (1-5%). The sheep was then shaved, ECG patches were applied, and an IV line was established in a leg vein. Once anasthesia was achieved an endotracheal tube was placed and the animal was connected to a ventilator. An oro-gastric tube was then placed into the stomach to prevent rumen aspiration. Throughout the procedure, ECG, heart rate, and bloodgas were monitored, and an IV infusion of 0.9% saline was maintained. Once all surgical preparations were complete, the sheep was switched to a propofol IV anesthetic. An initial bolus was administered at 2 mg/kg, followed by IV infusion at 0.2-0.8 mg/kg/min.

For the electrodes and DHSMs, an incision was made over the skull and the skin was reflected. A second incision was made over the right trapezious muscle. A 1.27 cm diameter tunneler was passed from the trapezoidal incission to the cranial incision,

for later use. A 3 mm Stryker burr (Kalamazoo, MI) was used to form a 2 mm by 3 mm craniotomy over the right motor cortex. The dura was carefully dissected from the cortical surface. Two methods of electrode insertion were attempted. In one case, a micromanipulator was secured to a bolt that was secured to the horn-bud of the animal. A suction-based insertion probe was used to hold each electrode array in place while it was being lowered. In the other case, an arm manipulandum was mounted to the surgical table. A micromanipulator was attached to the manipulandum, and a a vice probe was used to hold an electrode array.

Prior to electrode insertion, the region of cortex associated with motor output was localized. The cortex was stimulated with a WPI (sarasota, FL) constant current stimulator and hand held bipolar forceps. The stimulus consisted of a bipolar pulse, ranging from 0.5-10 mA. The duration of each phase was 1 ms, with a 1 ms pause between phases. The repetition rate was approximately 60 Hz. As the forceps were placed at various locations on the cortex, muscle groups associated with that region were observed to experience twitching. Regions associated with face and left limb were chosen for implant. Each array was then slowly lowered through the pia and into the cortical layers. Once the arrays were fully implanted, one of two methods was used to hold them in place. Either the resected skull was anchored back in place over the arrays using surgical titanium bone plates, or dental acrylic was used to cement each array in place. The headstages were also affixed to the skull using thin titanium bone plates. Before attaching the DHSMs to the ICCM, each headstage was connected to a PC-based 32-channel acquisition system, to examine each device for operability and to look for neural activity.

After DHSM operation was verified, the headstage cables were tunneled down to the ICCM implant site in the trapezious muscle. The cables were plugged into connectors on the ICCM and sealed. A pocket was formed for the ICCM using a

long curved Kelly clamp. The secondary coil was tunneled to a pocket located just posterior to the sheep's right shoulder, along the back. The transceiver antenna was tunneled to the left side of the animal, contralateral from the ICCM. The reference temperature probe was tunneled above the trapezious muscle, away from the ICCM.

5.4 *In Vivo* Data Collection

The TETS was used to power the fully implanted system during neural data collection. Rectified voltage at the switching regulators was measured using one of the channels on the temperature system. Temperature data was collected using the remaining five channels. Secondary coil temperatures were collected for two sheep. Of this data, the temperature of the wire was collected for one sheep, and the magnet temperature was collected for the other. The temperatures of the Can and headstage were recorded for two of the six experiments. As an additional verification, an external commercial digital thermometer was used to gather reference body temperature and Can temperature during these the studies.

In addition to voltage and temperature data, neural data was collected and examined for noise. To determine the effect of TETS operation on the system's ability to extract spikes, the acquisition system was powered both with an external DC power supply and with the TETS. RMS noise measures were calculated for all channels for the two power sources.

5.4.1 Rectified Voltage

For all six sheep studies, the TETS successfully powered the implanted system. The implant depth of the secondary coil was measured with calipers for studies three through six. Tissue thinckness ranged from 2.97-4.95 mm. In all studies, the data recorded from the electrodes was able to be wirelessly transmitted out of the body,

Digital Voltmeter	Fluke DMM	Tissue Thickness	Study #
17.7V	17.64V	-	1
14.86V-15.45V	-	3.66mm	5
19.9V-20.238V	-	3.89mm	6

Table 5.2: Rectified voltages at the input to the switching regulators. The first column presents voltages acquired with the digital voltmeter on the temperature system. For comparison, a Fluke 87 III DMM was used to verify the reading during the first study. This measurement was accomplished using a percutaneous DC jack. The third column shows tissue thickness between the implanted secondary coil and the surface of the body. Thickness measurements were taken with calipers.

using several of the ICCM's acquisition modes.

As described in section 4.2.4, one of the temperature channels was modified to measure the rectified voltage input to the switching regulators. Voltage measurements were taken in three sheep. The coil implant depth and recorded voltage are presented in table 5.2.

In the first study, a Fluke DMM and the DC power-in cable were used to measure the rectified voltage, for comparison with the digital voltmeter reading. Please refer to section 5.2.5 for a description of the cable. In studies 5 and 6, only the digital voltmeter on the temperature system was used to record rectified voltage. In all cases, the recorded voltages were well within the operating range of the secondary circuit.

5.4.2 Temperature rise of implanted components

Temperature data was collected during studies 5 and 6. In study 5, temperatures were recorded every 2 min, for approximately 100 min. In study 6, temperatures were recorded every 5 min, for approximately 125 min. In both studies, the temperature was allowed to reach steady state on all channels before recording was stopped. One exception was the headstage temperature data recorded during study 6. During this study, the thermistor cable failed, allowing only 80 min of temperature collection.

The absolute temperatures recorded during these studies are presented in figures

5.7- 5.10. Note that for the secondary coil, the study 5 data represents the temperature of the magnet, and the study 6 data represents the temperature of the secondary coil windings. Both sets of measurements were taken at the surface of each component, rather than at the outside surface of the encapsulation. Also note that in the figures, "Can lid" refers to the side of the ICCM enclosure facing the temperature system, and "Can base" refers to the side of the ICCM enclosure facing the FPGA.

In addition, the mean core body temperature of the sheep is also displayed in the figures. This temperature was recorded using a separate rectal thermometer available in the operating room. This thermometer was not calibrated against the same standard as the temperature system; thus, the data is presented for qualitative comparison. Core body temperatures were recorded approximately every hour, in compliance with the experimental protocol. Because so few data points are available, the mean core temperature is presented.

Between studies 5 and 6, the temperature data was analyzed and significant temperature increases were noted (as shown below). It was determined that one contributing factor may have been that the implanted components were not in full contact with well-perfused muscle tissue. Recall that the temperature studies referred to in chapter 1 were conducted in muscle tissue. Thus, during study 6, the components were implanted at depths that allowed them to be in greater contact with muscle, with the belief that the temperature rise would be reduced. The discussion section at the end of this chapter elaborates on this point.

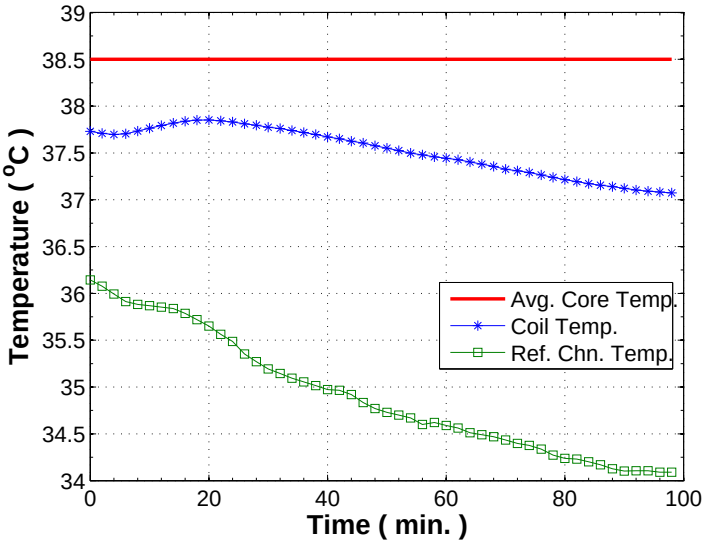

(a)

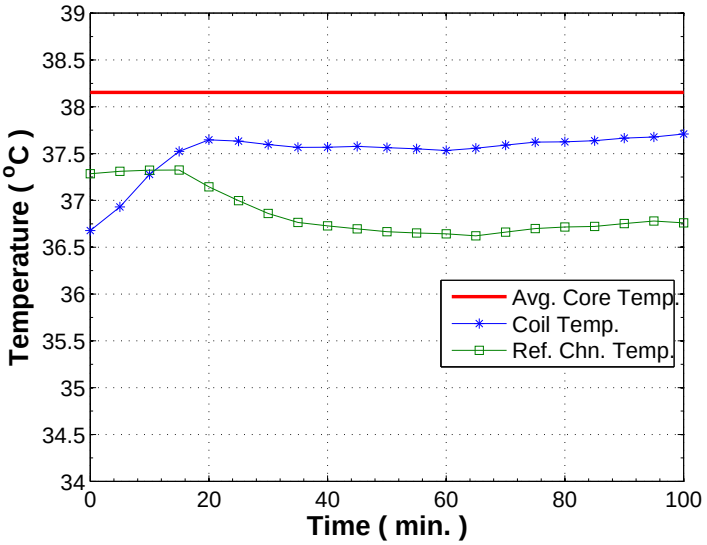

(b)

Figure 5.7: Absolute temperatures of (a) the secondary coil magnet, and (b) the secondary coil windings. Magnet temperatures were recorded during study 5, winding temperatures were recorded during study 6. The average core body temperature is also presented for qualitative comparison.

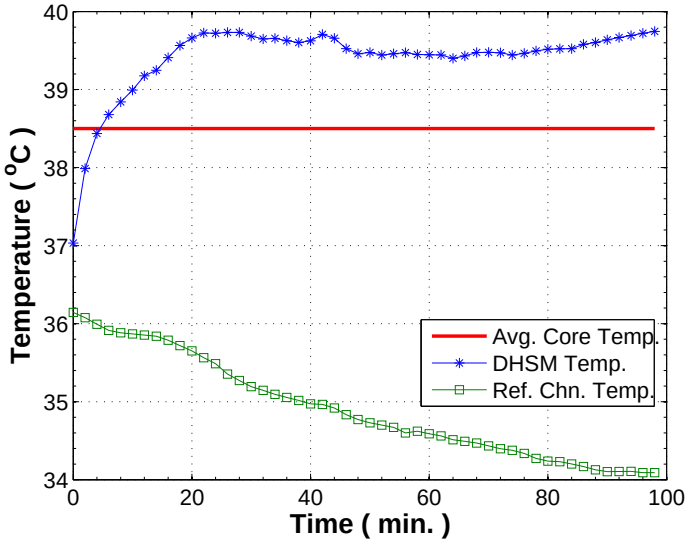

(a)

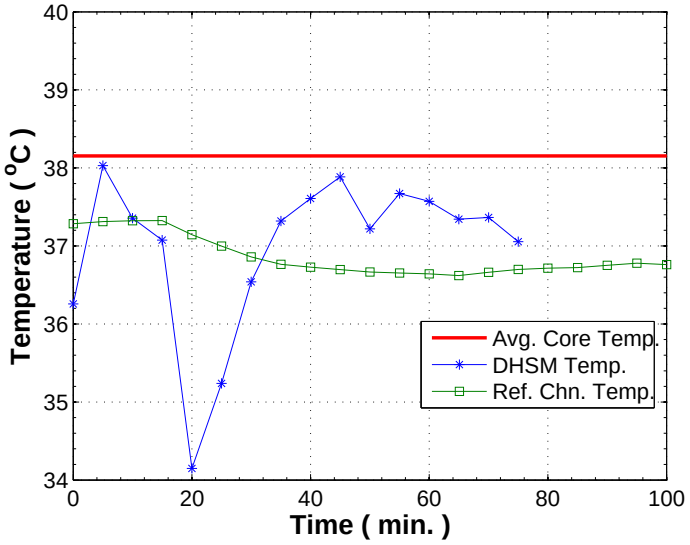

(b)

Figure 5.8: Absolute temperatures of the DHSM during (a) study 5 and (b) study 6. The average core body temperature is also presented for qualitative comparison.

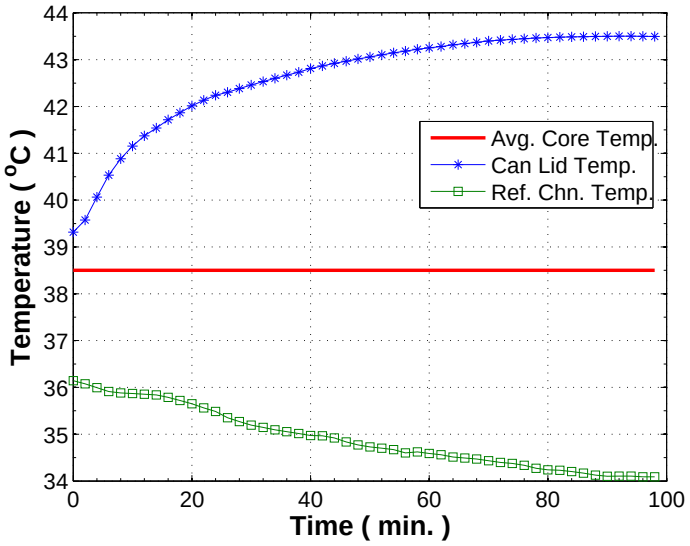

(a)

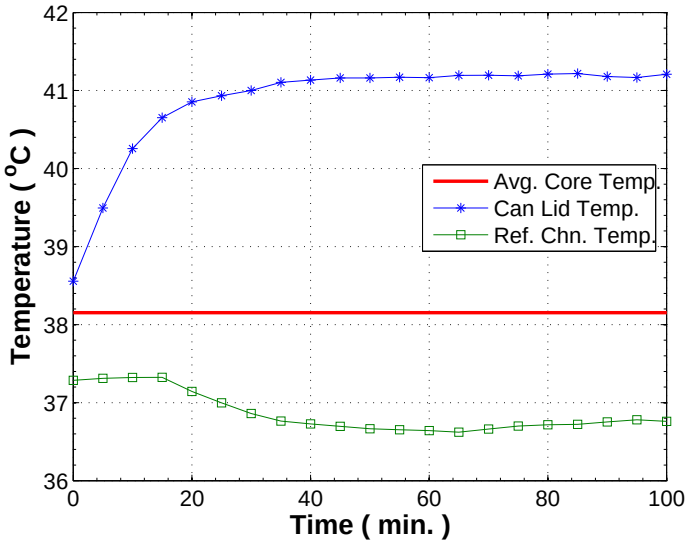

(b)

Figure 5.9: Absolute temperatures of the Can lid during (a) study 5 and (b) study 6. The lid refers to the half of the ICCM enclosure facing the temperature system. The average core body temperature is also presented for qualitative comparison.

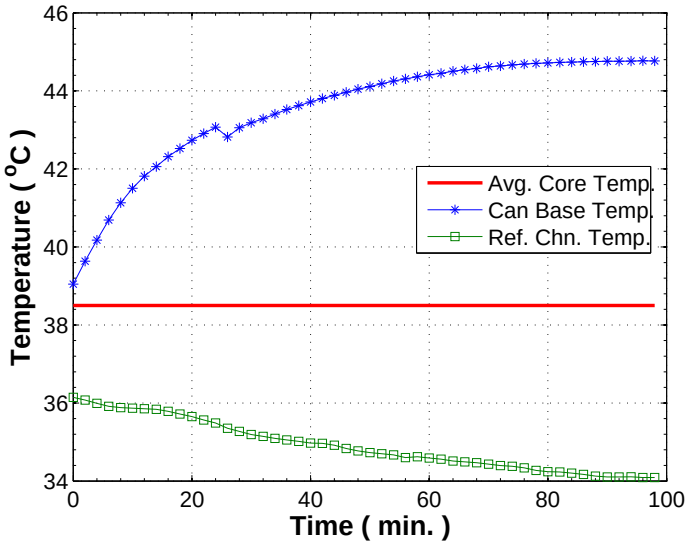

(a)

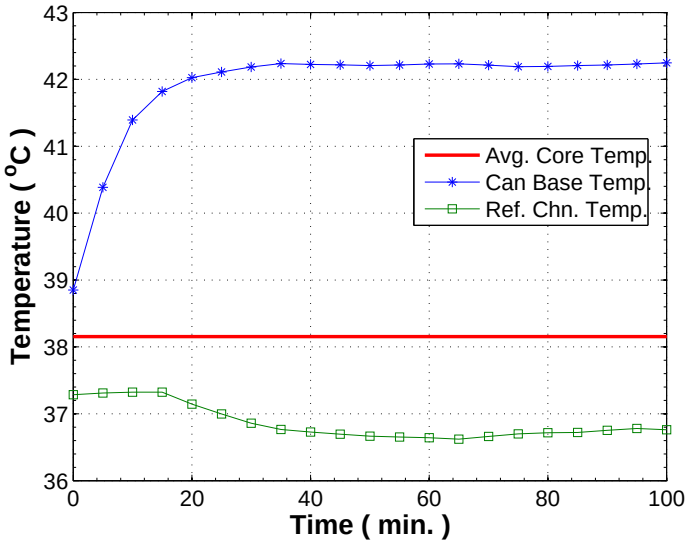

(b)

Figure 5.10: Absolute temperatures of the Can base during (a) study 5 and (b) study 6. The base refers to the half of the ICCM enclosure facing the FPGA. The average core body temperature is also presented for qualitative comparison.

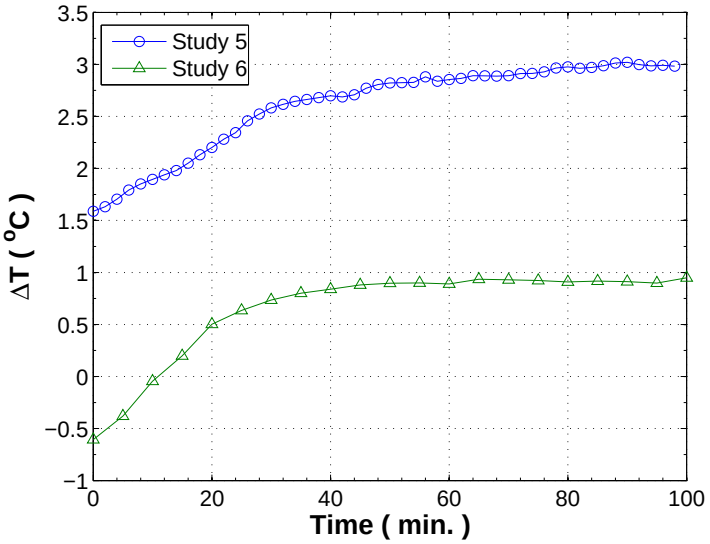

Figure 5.11: Change in temperature for the secondary coil and magnet vs. time. The change is taken with respect to the reference temperature channel. The magnet temperature was recorded during study 5, the coil temperature was taken during study 6.

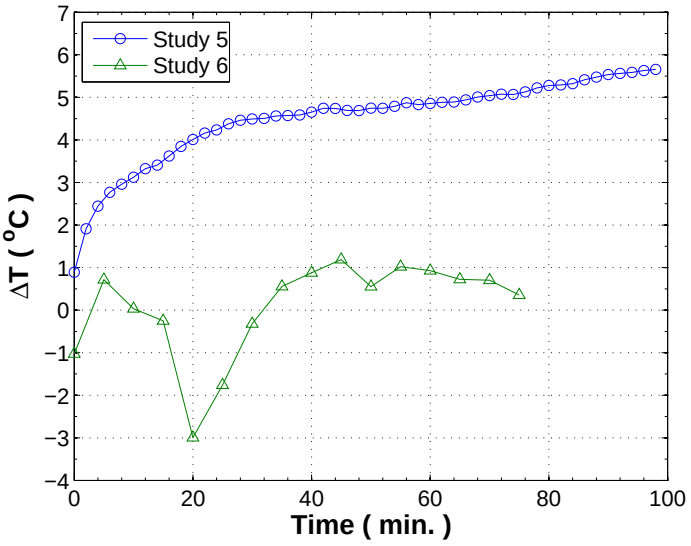

Figure 5.12: Change in temperature for the DHSM vs. time. The change is taken with respect to the reference temperature channel.

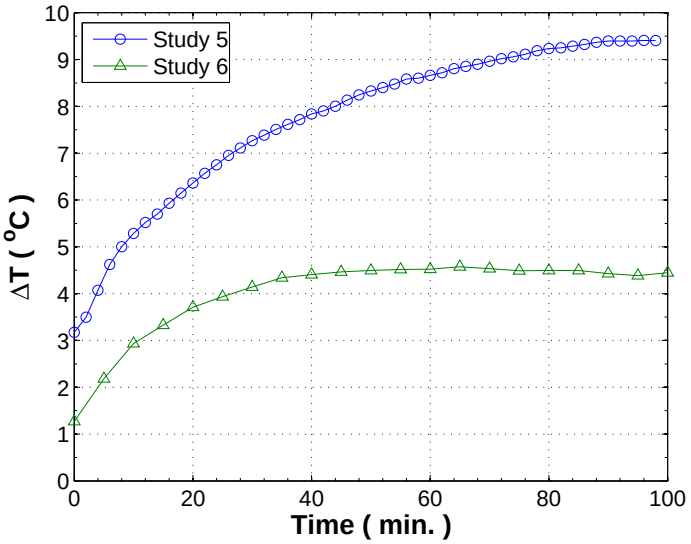

Figure 5.13: Change in temperature for the Can lid vs. time. The change is taken with respect to the reference temperature channel.

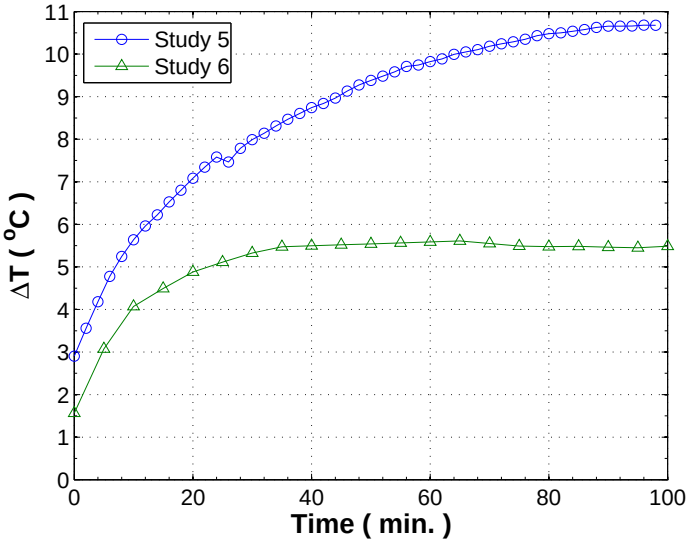

Figure 5.14: Change in temperature for the Can base vs. time. The change is taken with respect to the reference temperature channel.

Because the change in surface temperature is key to determining the feasibility of the 2 W system, the differences between the absolute temperatures and the reference channel temperature was taken. The time-course of temperature increase for each channel is plotted in figures 5.11-5.14. Maximum temperature increases are also presented in table 5.3.

Sheep study	Maximum ΔT
Channel 1 - Secondary Coil	
5	3.0196 ± 0.1411°C
6	1.1789 ± 0.2225°C
Channel 2 - DHSM	
5	5.6551 ± 0.1637°C
6	1.1887 ± 0.6758°C
Channel 4 - Can Lid	
5	9.4072 ± 0.1616°C
6	4.5726 ± 0.3213°C
Channel 5 - Can Base	
5	10.6797 ± 0.1648°C
6	5.6115 ± 0.4048°C

Table 5.3: Table of maximum temperature rise for each channel. Of the six available channels on the temperature system, one was converted to a voltmeter, and another was used as a reference probe. The temperature changes reported here are taken with respect to the reference channel.

5.4.3 Effects on neural data

By design, the TETS radiates a large amount of electromagnetic interference. To verify that this radiation does not limit the ability of the implanted neural acquisition system to detect spikes, acquired neural data was examined for TETS noise. Both a DC power source and the TETS were used to power the system while neural data was recorded. The data was collected and stored using the neural data portion of the GUI (which previously existed, and is not original to this work).

	TETS	**DC Source**
chns in sample	159	82
mean RMS noise	6.49 μV	5.88 μV
max RMS noise	14.70 μV	8.91 μV
min RMS noise	3.65 μV	4.15 μV
σ_{RMS}	2.55 μV	0.91 μV
mean window size	1.3173 s	6.5435 s
max window size	11.6 s	24.3501 s
min window size	0.108 s	0.25 s

Table 5.4: Noise statistics for data collected with the 96-channel neural acquisition system during three sheep studies. The system was powered with the TETS and with an external DC source for noise comparison.

A total of 159 channels from TETS-powered systems, and 82 channels from DC-powered systems were compared using Matlab. Data was taken from sheep studies 3, 4, and 6. For each channel, RMS noise measures were calculated after removing the mean. Sample windows were chosen to minimize the presence of spikes. For the TETS, the frequency was adjusted as necessary, to place the aliased noise at the highest possible frequency. Table 5.4 lists the noise statistics.

Figure 5.15 shows an action potential recorded on the same channel on the same day, with the acquisition system powered by the TETS and by an external DC source. The RMS noise for the two channels is nearly identical.

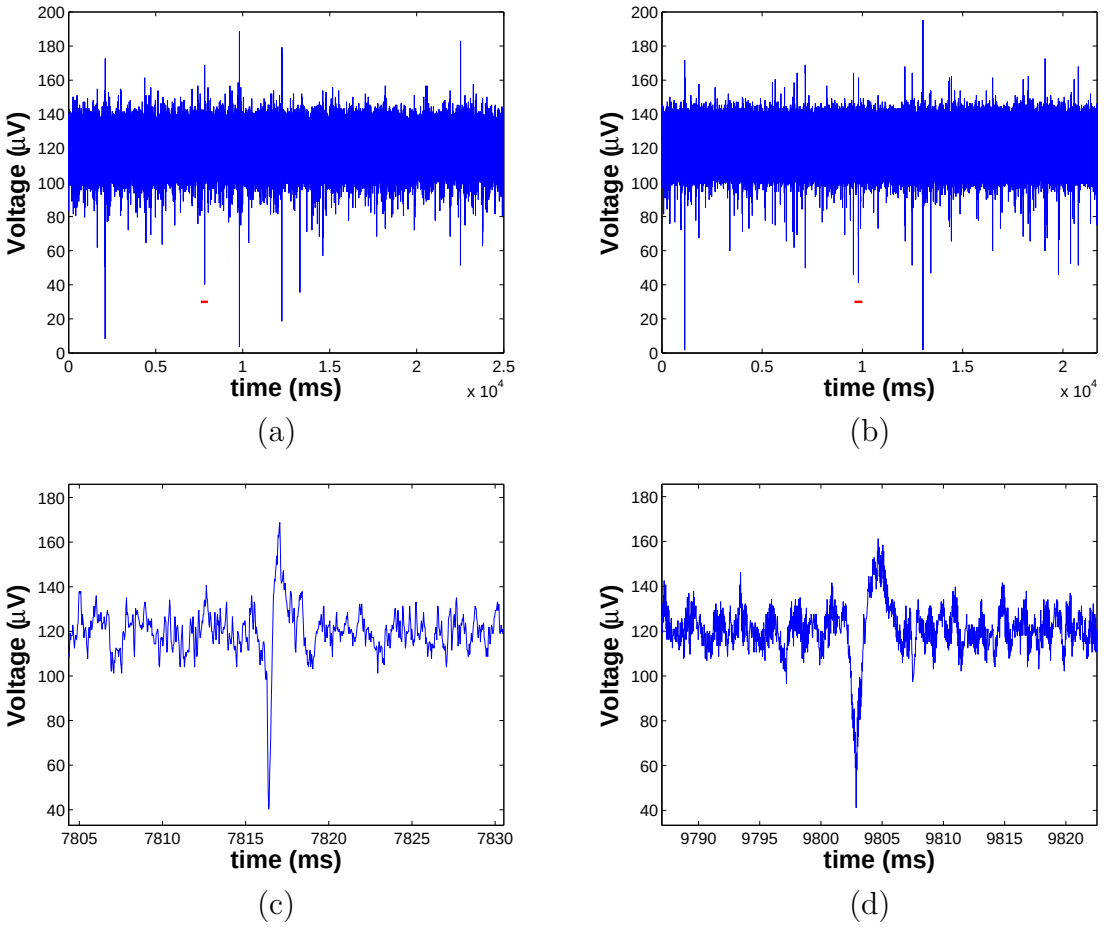

Figure 5.15: Comparison of the neural signal recorded on one channel of the implanted acquisition system, powered first by an external DC source (left column), then by the TETS (right column). Figures (a) and (b) show the raw signal received from the ICCM. The short underline in each plot indicates a spike that was time–magnified in figures (c) and (d), respectively. The calculated RMS noise was 7.16 μV for the DC-powered system, and 7.58 μV when the TETS was used. The TETS was tuned so that aliased noise was placed at the highest possible frequency.

It is also useful to demonstrate whether the acquisition system can detect spikes even if the frequency of the TETs is not tuned. The same channel presented in figure 5.15 was recorded prior to tuning the TETS frequency. That signal is presented in figure 5.16. As shown in the figure, the RMS noise on the channel is 16.1 μV. A low amplitude spike ($\approx$ 100 μV_{pk-pk}) was chosen as an example. A close-up view of the spike shows that the TETS noise is quite noticable. In spite of this noise, the figure shows that the spike is detected and extraced by the ICCM.

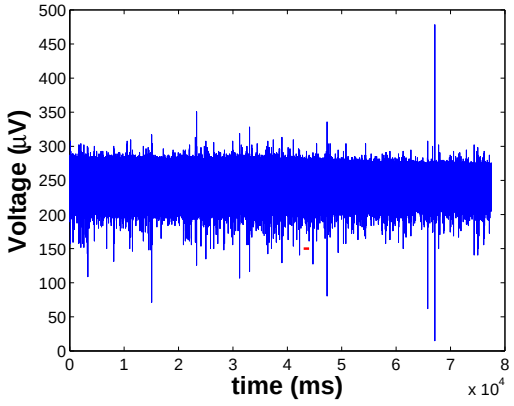

(a)

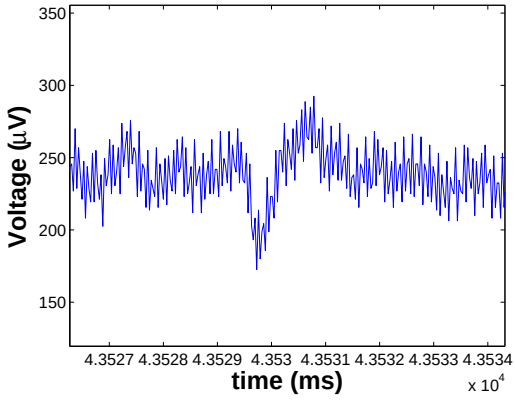

(b)

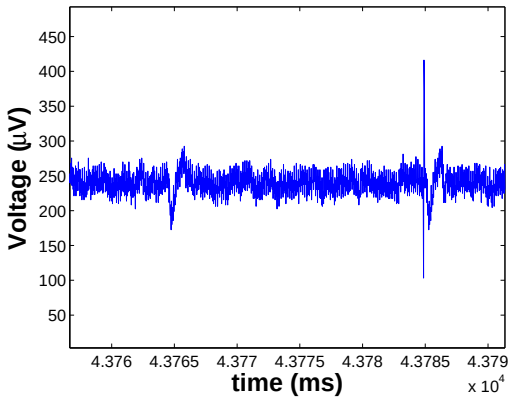

(c)

Figure 5.16: A neural signal acquired when the TETS is not frequency-tuned. (a) A low amplitude spike ($\approx$ 100 μV_{pk-pk}) was chosen from the raw neural signal, as indicated by the underlined region. (b) A time-magnified view of the spike. The RMS noise was 16.1 μV. (c) The ICCM detects and extracts the spike. The higher-amplitude, short duration pulse is the time stamp and channel number. A copy of the extracted spike is also placed at the end of the packet.

5.5 Discussion

The key finding presented in this chapter is that the TETS was able to successfully deliver approximately 2 W to a fully implanted neural acquisition system. Rectified voltage measurements taken during three *in vivo* sheep studies indicate that anywhere from 14.86-20.24 V was provided to the switching regulators. According the findings in section 2.7, voltages at this level would allow for 8-12 mm of axial coil displacement, or as much as 20 mm of radial coil displacement. These distances are reasonable for TETS application in an ambulatory animal.

Another important finding is that the TETS was able to power a putative medical device that has a low tolerance for noise. Because of the low signal-to-noise ratios that are inherent in neural signals, excessive noise generation would corrupt the signal of interest. This research demonstrates that spikes are able to be extracted from raw neural data, even when the switching frequency of the TETS is not optimally tuned for noise reduction. Indeed, although a number of channels were noisy even after frequency-tuning, many channels were as noisy, or were less noisy, then when the acquisition system was powered with a DC source. This finding indicates that a low-noise, neural acquisition system with a distributed component topology allows for continual power delivery with a TETS.

Finally, table 5.3 shows that the temperature increase in study 5 was substantial, but that the increase during study 6 was much more limited. These findings warrant further discussion.

5.5.1 Temperature Rise of Implanted Components.

A comparison between studies 5 and 6 reveals several factors that may have lead to such a temperature disparity. First, the implant depth of the Can varied considerably between the studies. In study 5, the implant depth was 4.85 mm. The base of the

Can was in contact with the trapezious muscle, but the lid was in contact with subcutaneous fat. The measured thermal conductivity of this type fat is about half that of skeletal muscle [48]. In study 6, the implant depth of the Can was 18.2 mm. In this case, both sides of the Can were in contact with muscle.

For the DHSM, implant depth may also have been an important factor. In study 5, a large section of muscle was removed from the area of the craniotomy. The thermistor-bearing DHSM was mounted directly against bone. The thermal conductivity of cancellous bone has been measured as anywhere from one to three quarters of that of muscle [48, 97, 98]. With the scalp sutured, the top of the DHSM was in contact with subcutaneous fat. In this study, very little muscle tissue was present near the devices. In study 6, much of the rostral end of the neck muscle was intact following dissection. As a result, a substantial portion of the DHSM was in contact with well-perfused tissue.

In the case of the secondary coil, the implant depths were similar. The change in the magnet temperature in study 5 was slightly more than 1°C over the 2°C FDA limit. Although the same packaging technique was used for the coils in both studies, the silicone encapsulation was thicker in the coil used in study 5. (Recall that the temperatures cannot be directly compared, because the magnet temperature was taken in study 5, but the coil temperature was taken in study 6.) Over the magnet, the encapsulation was approximately 2-3 mm thick, whereas in the later study, the encapsulation thickness was reduced to only 1 mm. In addition, a flatter, larger diameter magnet was chosen for study 6. The surface area was increased from 7.92 cm^2 to 12.96 cm^2. These two changes may help reduce the temperature of the magnet. In study 6, the temperature of the secondary coil windings was well below the 2°C limit.

Apart from the differences in implant depth, the most significant factor contribut-

ing to the temperature increase was the effect of anesthesia. It is well documented that the types of anesthesia used in these studies significantly impair normal autonomic thermoregulatory control [99]. A major piece of evidence that thermoregulation was interrupted was the marked decrease in the reference channel temperature in study 5, despite core temperature maintenance. Although only mean core temperature is shown in figures 5.7-5.10, there was no trend in the core temperature, and readings did not varying significantly about the mean. In addition, the Can took a considerable amount of time to reach steady state in the 5th study. It has been reported that for power densities at, or greater than, the those of this system, temperatures reach steady-state in approximately 30-40 minutes [38, 39, 40, 41, 42]. The temperature profiles in study 6 did exhibit this sort of time course. It can be concluded, given the power densities involved, the effect of implant depth, and the effects of anesthesia, that the temperature increase brought on by the operation of implanted electronics would be further reduced in an ambulatory animal model.

5.5.2 System Modifications.

An easy way to reduce Can temperatures is to increase the surface area. In this research, the Can was sealed with various types of silicone adhesives. As seen in figure 5.6, the adhesive occupies substantial surface area. Specifically, approximately 41 cm^2 is taken up by the adhesive. Cured silicone is around 100 times less thermally conductive than the titanium enclosure. If this insulation were removed, it would effectively double the thermally conductive area currently available for heat dissipation.

Removing the adhesive would require two major changes to the ICCM enclosure. First, it would require that the Can be sealed using welding techniques. Welding is the industry standard for sealing implanted medical devices. Although basic welding

services are available at Duke, this research group has not had success with the tungsten inert gas (TIG) welding technique required for fusing titanium. Assuming that the enclosure could be welded closed, the second major obstacle is that pass-throughs would be required for the 42 conductors that must exit the Can. Such a high conductor-count pass-through is not presently available, and would have to be custom made. Cost estimates for pass-throughs have been quoted as several tens of thousands of dollars. For a proof-of-concept system, the costs of both of these measures are prohibitive.

Chapter 6

Summary

The design, construction, and testing of a transcutaneous energy transfer system and an implantable temperature monitoring system have been described. This chapter offers a brief discussion of the overall findings of the presented research.

6.1 Novel Contributions

For the first time, a mid-range transcutaneous energy transfer system has been developed for powering a 2 W fully-implanted wireless neural acquisition system. Several key features were introduced during system design, which ultimately allowed for this breakthrough. These features, original to this research, are summarized below.

- Step down switching regulators were used in the secondary to combat voltage droop due to coil displacement. These components achieved this goal through their negative impedance characteristic, which allows them to compensate for decreased coil coupling. This characteristic also prevents excessive internal power dissipation when the coils are closely coupled.

- The 96-channel neural acquisition system was acutely implanted in an ovine animal model, and was able to acquire action potentials without being corrupted by TETS noise. Induced noise was limited by distributing the acquisition system components; by using a conductive enclosure to shunt the induced current; and by tuning the TETS operating frequency.

- Real time surface temperatures were recorded from the fully powered device using a custom-designed 6-channel digital thermometer. The recorded temperature data show that temperature monitoring is a necessary feature for implanted systems requiring power levels on the order of 2 W.

- The MOSFET H-bridge was shown to be a viable driver topology for inductively-powered systems. This topology provides a simple, inexpensive approach for rapidly developing a TETS. The topology also shows reasonable efficiency, which can be improved with modest effort, using established techniques.

- A power delivery sense circuit was designed in the primary to detect the presence of the secondary. This circuit achieved this goal by monitoring the current delivered from the primary DC power source.

In the following sections, each of these items is discussed in more detail.

6.1.1 Switching Regulators

The most distinguishing feature of the TETS design is the use of high input-voltage step-down switching regulators in the secondary. These components allow for a completely new approach for mitigating the voltage droop caused by coil displacements. In low-power TETS design (<100 mW), the common approach is to actively tune the primary DC power source to *lower* the voltage delivered to the secondary regulators. Linear regulators are universally used in these designs, so managing the input voltage is critical for efficiency, and ultimately thermal management. Such management requires voltage measurement circuitry in the secondary; the use of a feedback telemetry channel for conveying the voltage information to the primary; a telemetry receiver/demodulator in the primary to receive the signal; and control circuitry for adjusting the primary DC power source. Incorporating these features can be onerous.

The approach used in the mid-range system designed during this research is the exact opposite of that taken for low-power systems. The 24 VDC primary power source, the coil configuration, and voltage doubler rectifier work in conjunction to provide as much voltage to the switching regulators as possible. It was demonstrated that the induced voltage at the input to the regulators was as high as approximately 22 V (figure 2.12). By dramatically overshooting the 6-7 V dropout voltage of the regulators, the system could tolerate axial coil displacements as large as 2 cm (figure 2.13). This degree of tolerance is on par with other well-known TETS designs.

An important property of switching regulators is that power remains nearly constant from input to output; the regulator itself operates very efficiently. In basic terms, that means that the regulator draws only as much power as the downstream application requires, plus a minimal amount of power to operate internal circuitry. It is able to maintain constant power by exchanging input voltage and current. As the input voltage goes up, the current draw goes down (and vice versa). These fundamentals are described in section 2.1.5. Translating this feature to a TETS application, as the coils separate, induced secondary voltage decreases with decreased coupling. The switching regulators compensate by drawing more current, thereby decreasing the impedance seen by the secondary coil (figure 2.14). The result is that the impedance reflected into the primary stays relatively constant(figure 2.15). By extension, the link efficiency also stays virtually constant over the entire range of axial coil separations (figure 2.16). No other published system has demonstrated nearly this level of constancy in link efficiency. The principal research groups in the area of TETS design have reported efficiencies that vary by tens of percents over the intended operating regimes [22, 25, 52, 56, 71, 100]. This result is quite remarkable!

6.1.2 TETS Noise Minimization

Development of the TETS lead to the first demonstration of a high channel-count, fully-implanted neural acquisition system. A major obstacle to this achievement was limiting the noise picked up by the electrodes. Leading up to the *in vivo* sheep experiments, the acquisition system was tested with the TETS in a simple saline bath. It was found that the distance between the secondary coil and the electrodes did reduce TETS noise by approximately several μV rms. However, the biggest factor for reducing the noise was the introduction of a conductive enclosure that was tied to a ground terminal on the ICCM. This enclosure provided a low impedance return path for any capacitively-coupled currents. The resulting noise was reduced to less than 10 μV rms on most channels.

Another important feature of the TETS that allowed the noise to be minimized was the ability to tune the primary switching frequency. Within the LabView GUI, a real time plot of the power spectrum of a neural channel was created using built-in functions. This simple utility allowed the TETS noise to be viewed spectrally, so that the switching frequency and harmonics could be adjusted out of the passband of the sensing amplifiers.

As demonstrated in section 5.4.3, the average noise measured *in vivo* was 6.49 μV rms. This level of noise was very close to baseline, 5.88 μV rms, measured when the system was powered by a DC source. Because the noise was limited, the signal processing algorithms within the ICCM were able to extract spikes from recorded neural signals.

6.1.3 Real Time Temperature Monitoring

In this research, a TETS was designed for a 2 W neural acquisition system. As discussed in sections 1.4 and 1.7, this amount of power requires a large surface area

to dissipate the heat and minimize temperature rise. The 96-channel neural data acquisition system powered by the TETS uses a distributed architecture, where various subsystems are implanted at different locations in the body. For the implanted components of the system, the power densities are approximately: 32 mW/cm^2 for a single DHSM; 10 mW/cm^2 for the ICMM; and less than 5 mW/cm^2 for the secondary coil. These power densities are less than 40 mW/cm^2, which is thought to be the threshold for a 2°C temperature rise). However, the DHSM is precariously close to this recommended limit. Therefore, a small 6-channel digital thermometer was designed to connect to the ICCM, within the titanium enclosure. This temperature system allows bead thermistors to measure the surface temperature of any implanted component. The resulting data can then be telemetered out of the body for recording. Thus, in future studies, temperature can be monitored in real-time in an ambulatory test subject and temperature safety can be assured.

This feature is also important for eventual clinical use of the neural acquisition system. The data recorded during the sheep studies provide a great example of why this temperature system is a necessary tool. When the components of the neural acquisition system were implanted too shallow, a maximum temperature increase of approximately 10°C was recorded from the surface of the enclosure. Had this measurement occurred in a human patient during surgery, measures could have been taken to ensure adequate implant depth. In addition, any number of electrical faults could arise within the acquisition system, that may not affect system operation in an observable way. FDA regulations state that the temperature rise of any implanted component should not exceed 2°C, including for the case of a single fault condition [37]. For a 2 W system operating with the power densities listed above, any fault resulting in greater internal power dissipation could bring about such an increase. Thus, the temperature system should be considered an integral part of the acquisition

system.

Finally, with respect to performance, in the acute studies presented in chapter 5, the temperature system was able to measure temperatures from all three major subassemblies, and from a reference probe, with a 50 ms latency. Calibration data showed that, with a minor exception, the temperature system had an accuracy of approximately ±0.1°C. Such accuracy is beneficial for monitoring slight temperature increases associated with electronic heating.

6.1.4 H-bridge topology

The first *in vivo* demonstration of the H-bridge circuit topology as a viable primary coil driver was presented. What is advantageous about this topology is its simplicity, effectiveness, and low component-count. While ease of design, itself, is not necessarily a motivating research objective, achieving simplicity is a major consideration in the medical device industry. The TETS developed here is easily adaptable to a host of medical device applications including wireless battery recharging, powering small pumps, or powering neural recording or stimulation devices in real time. Reducing circuit complexity is an important step in translating a proof-of-concept system into a marketable product, especially for a system with so many potential uses.

The H-bridge is also advantageous because its efficiency can be improved with a combination of component selection and more advanced switching techniques. It was shown in section 2.8.4 that 72% of the power losses in the primary were attributable to three components: the power MOSFETs, the wire of the primary coil, and the polymer power supply capacitors. Though there may be cost and/or size trade-offs, these components could be substituted for more efficient versions. In conjunction with upgraded components, alternative switching regimes could be implemented. Such techniques are described below, in section 6.2. It should be restated, however, that

a major thrust of this research was not to optimize primary efficiency. Rather, the goal was to address the 2 W power requirement while mitigating temperature rise.

6.1.5 Power Delivery Sensing

A second novel feature of the TETS is the power delivery sensing circuit in the primary (section 2.7.8). While it could be argued that class-E systems also detect the presence of the secondary, since they continually monitor for changes in primary resonance, the technique introduced here is fundamentally different. The present design directly monitors power delivered to the secondary, rather than indirectly monitoring impedance variations. This system is the first demonstration of this technique. Using basic current sense amplifier and comparator topologies, an LED is illuminated to indicate secondary regulation. Although simple, such a feature would be invaluable in a clinical TETS application, where the patient would need to know when the coils are aligned enough for sufficient power delivery.

6.2 Future Work

As stated above, an important contribution of this work is the introduction of a new method for mitigating coil misalignment using switching regulators. Application of this method stabilizes variability in the reflected impedance, and by extension, the efficiency. While stability itself is an achievement, the overall TETS efficiency can be increased through further optimization. As discussed in section 2.8.4, the major contributors to inefficiency are, to a large extent, associated with the H-bridge components. As mentioned in the earlier section, reducing capacitor ESR and MOSFET on-resistance are good starting points for optimization. An additional step would be to implement zero voltage switching (ZVS). The principle behind zero voltage switching is that the MOSFET's output capacitance is discharged before the switch

is turned on. This prevents the MOSFET itself from having to dissipate the stored energy. In addition to saving power, ZVS reduces component stresses and can extend component life.

In addition to ZVS, zero current switching (ZCS) could also be used to reduce losses in the MOSFETs. Whereas ZVS stipulates zero voltage across the MOSFET at turn-on, ZCS stipulates zero current through the device at turn-off. As the component is switched off, the channel resistance dramatically increases (eventually to an open circuit by definition). If current is flowing through the device, significant power can be wasted. To summarize, both ZVS and ZCS could be implemented to improve efficiency in the primary driver.

Another improvement that could be made to the H-bridge driver is to reduce the voltage of the primary DC power source. The obvious trade-off is that some tolerance to coil displacement would be lost. However, for applications where 2 cm displacements are not an issue, power savings could be attained. To demonstrate that the TETS design is robust to lower DC bus voltages, a 12 V TETS was also fully built and tested *in vivo*. No changes were required in the secondary. In the primary, the hot swap electronic circuit breaker was reprogrammed for lower under- and over-voltage protection. The 12 V switching regulator was also bypassed. During the final sheep study, both the 24 V and 12 V systems were used to power the neural acquisition system. The digital voltmeter on the temperature system was used to record the voltage at the input to the switching regulators. The 24 V system provided approximately 20 V to the regulators, at a cost of 7.44 W. The primary coil was unplugged from the 24 V system and left in place over the secondary coil (using the magnets). The 12 V system was then connected to the primary coil. This lower power system was able to deliver approximately 8.76 V to the regulators, at a cost of 3.48 W. Although the 8.76 V would likely not be robust to major coil displacements, the

total power was more than cut in half. The overall DC-DC efficiency was increased from around 24% to more the 55%. These results show that the designed TETS can easily be adapted to the conditions most suitable for a given application.

6.3 Conclusion

This research has resulted in the development of a novel transcutaneous energy transfer system. This mid-range design is the first such system in its class. The design is easy to understand and implement; the system is comparable to other TETS designs in the degree to which it can tolerate coil displacement; and the efficiency is good, and is extremely stable, even at the limits of coil displacement. The TETS was crucial in demonstrating the first successful fully-implanted, high channel-count neural acquisition system.

Appendix A

Temperature System Calibration Curves

This appendix provides a graphical presentation of the temperature system calibration curves. The calibration procedure was described in section 4.5.2. The best fit lines, mean squared errors, and r values presented in table 4.2 were generated from the data below. The graphs on each page show the calibration data from sheep studies 5 and 6, for each channel of the temperature system. Within each graph, the dashed line represents the 1-to-1 reference line, and the diamonds are the data collected from a particular channel. The reference line is provided so that the relative accuracy of a temperature channel can be assessed. The closer the recorded data is to this line, the closer the channel is to reading the same value as the reference thermometer (which is serving as a standard in this experiment).

The first plot presented below is for the voltmeter. Recall that one of the channels of the temperature system was converted to a voltmeter, so that rectified TETS voltage could be measured through the wireless system. In this case, because the voltmeter was so accurate, a reference line is not included. Note also that the data is presented as a solid line, rather than as individual data points. With step sizes as small as 0.1 V, the data points are indistinguishable on reasonably scaled axes.

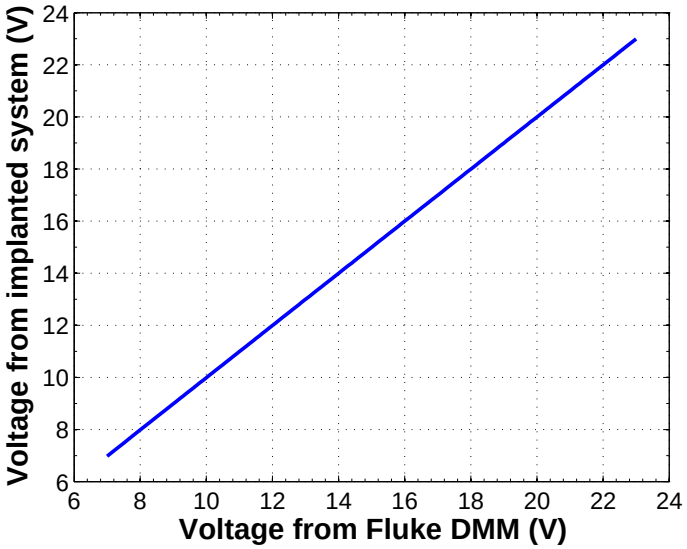

Figure A.1: Voltmeter Calibration Curve. An external DC power supply was input to the switching regulators where the voltmeter was connected. Voltage was swept from 7-23 V. The input voltage was not increased beyond 23 V, because the 24 V zener protection diode was installed. The measured voltages show excellent agreement with the measurements of two Fluke digital multimeters (DMMs). Section 4.5.1 presents the results of curve fitting.

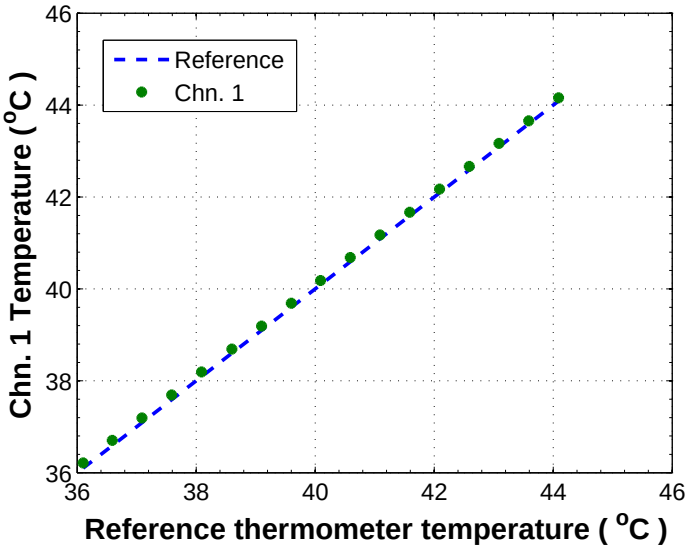

Figure A.2: Calibration curve for channel 1, sheep study 5. The channel 1 thermistor was connected to the secondary coil for this study.

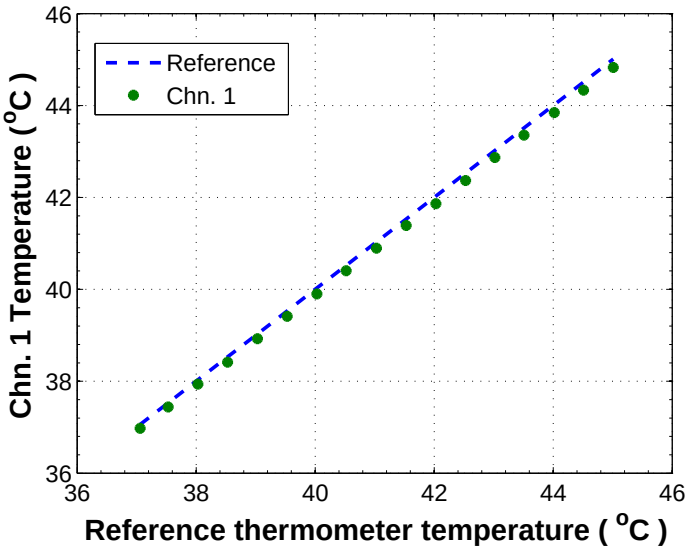

Figure A.3: Calibration curve for channel 1, sheep study 6. The channel 1 thermistor was connected to the embedded ceramic magnet of the secondary coil for this study.

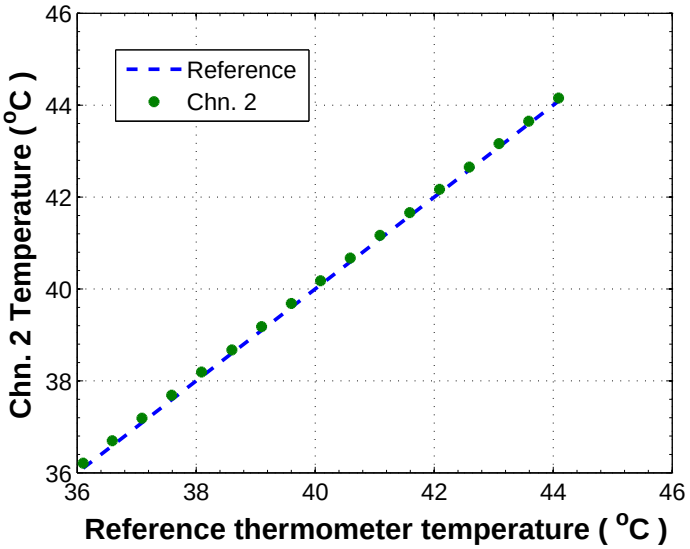

Figure A.4: Calibration curve for channel 2, sheep study 5. The channel 2 thermistor was connected to the digitizing headstage module (DHSM) for this study.

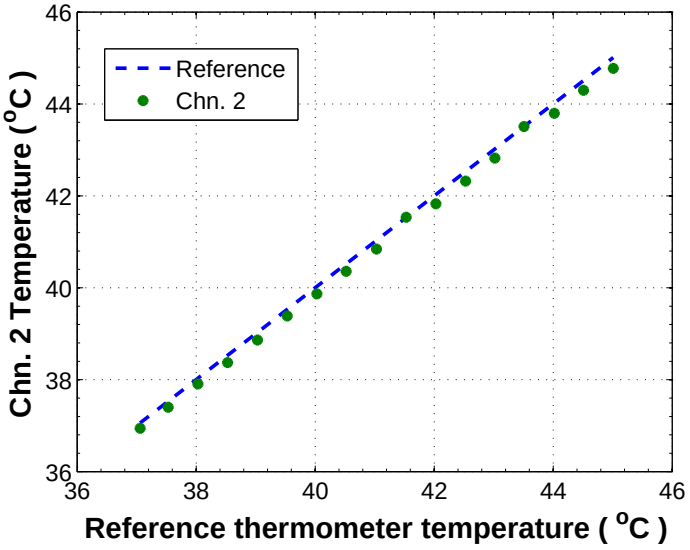

Figure A.5: Calibration curve for channel 2, sheep study 6. The channel 2 thermistor was connected to the digitizing headstage module (DHSM) for this study.

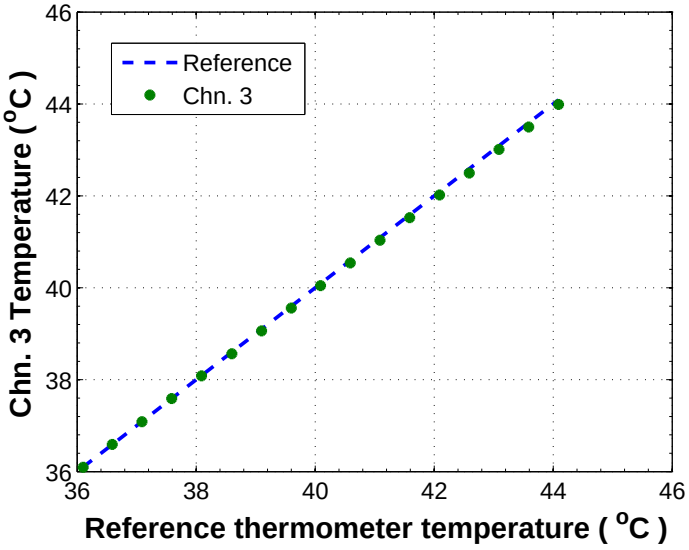

Figure A.6: Calibration curve for channel 3, sheep study 5. The channel 3 thermistor served as a reference channel for all studies.

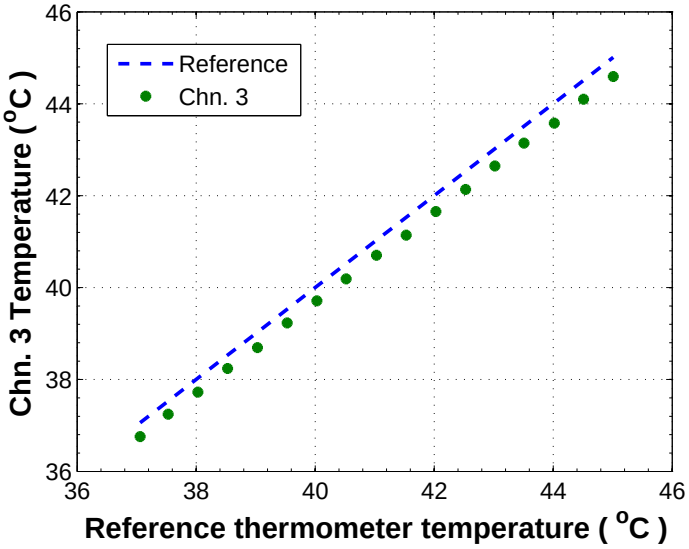

Figure A.7: Calibration curve for channel 3, sheep study 6. The channel 3 thermistor served as a reference channel for all studies.

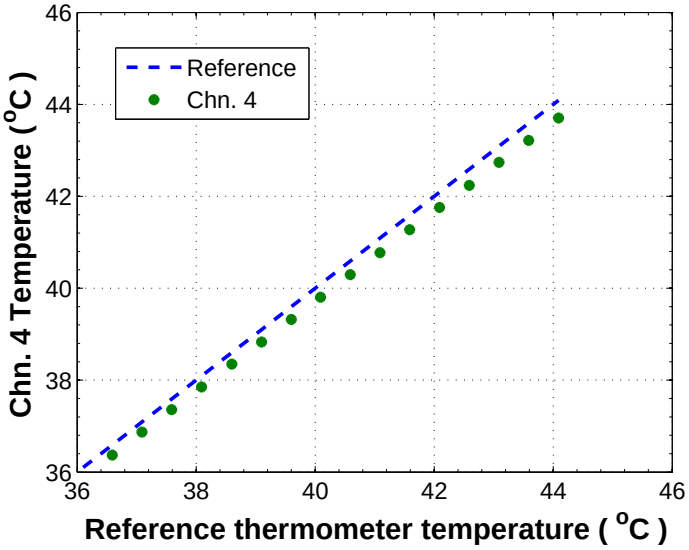

Figure A.8: Calibration curve for channel 4, sheep study 5. The channel 4 thermistor was mounted to the upper surface of the titanium enclosure. This part of the enclosure is nearest the skin of the animal, facing away from the body core.

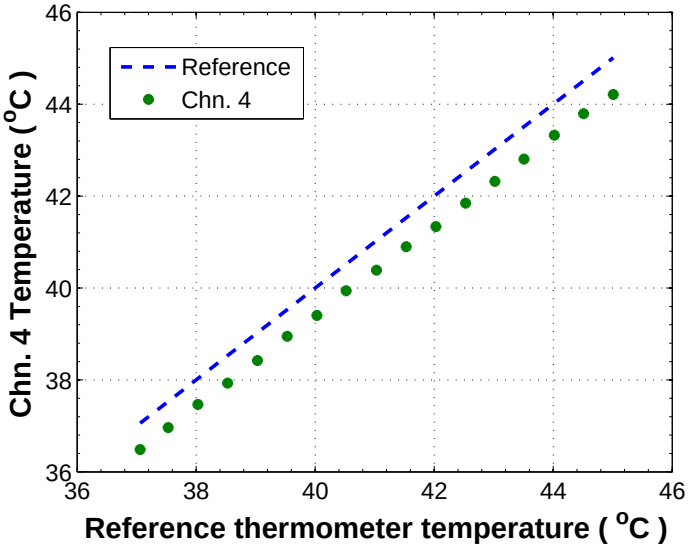

Figure A.9: Calibration curve for channel 4, sheep study 6. The channel 4 thermistor was mounted to the upper surface of the titanium enclosure. This part of the enclosure is nearest the skin of the animal, facing away from the body core.

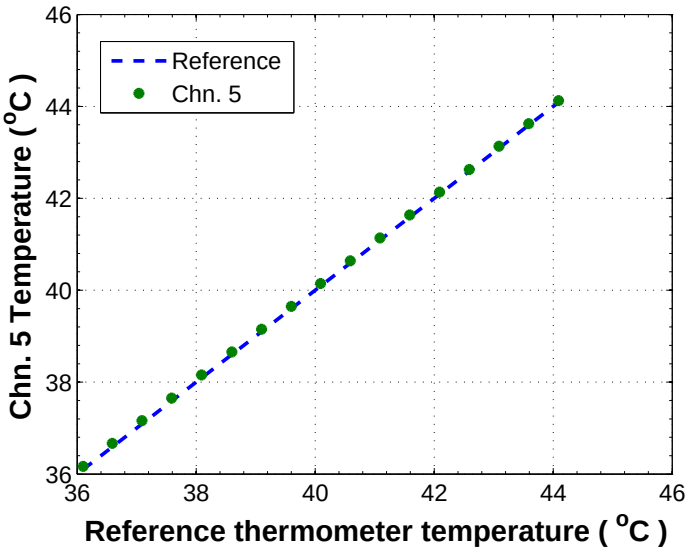

Figure A.10: Calibration curve for channel 5, sheep study 5. The channel 5 thermistor was mounted to the lower surface of the titanium enclosure. This part of the enclosure is nearest the body core of the animal, away from the skin.

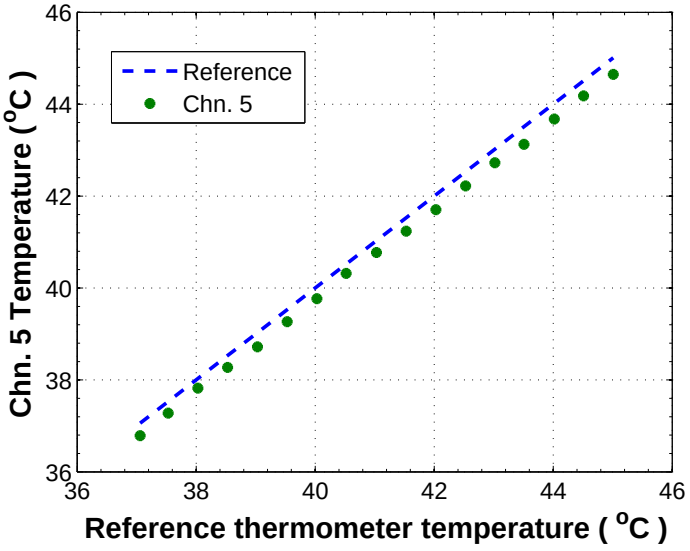

Figure A.11: Calibration curve for channel 5, sheep study 6. The channel 5 thermistor was mounted to the lower surface of the titanium enclosure. This part of the enclosure is nearest the body core of the animal, away from the skin.

Bibliography

[1] G. Schalk, J. Kubanek, K. J. Miller, N. R. Anderson, E. C. Leuthardt, J. G. Ojemannm, D. Limbrick, D. W. Moran, L. A. Gerhardt, and J. R. Wolpaw. Decoding two-dimensional movement trajectories using electrocorticographic signals in humans. *Journal of Neural Engineering*, 4(3):264–275, 2007.

[2] J. R. Wolpaw and D. J. McFarland. Control of a two-dimensional movement signal by a noninvasive brain-computer interface in humans. *Proceedings of the National Academy of Sciences of the United States of America (PNAS)*, 101(51):17849–17854, Dec. 2004.

[3] J. M. Carmena, M. A. Lebedev, R. E. Crist, J. E. O'Doherty, D. M. Santucci, D. F. Dimitrov, P. G. Patel, C. H. Henriquez, and M. A. L. Nicolelis. Learning to control a brain-machine interface for reaching and grasping by primates. *Plos Biology*, 1:1–15, Oct 2003.

[4] S. Kim, S. C. Manyam, D. J. Warren, and R. A. Normann. Electrophysiological mapping of cat primary auditory cortex with multielectrode arrays. *Annals of Biomedical Engineering*, 34(2):300–309, Feb 2006.

[5] R. E. Isaacs, D. J. Weber, and A. B. Schwartz. Work toward real-time control of a cortical neural prosthesis. *IEEE trans. on Rehabilitation Engineering*, 8(2):196–198, Jun 2000.

[6] R. R. Harrison, P. T. Watkins, R. J. Kier, R. O. Lovejoy, D. J. Black, B. Greger, and F. Solzbacher. A low-power integrated circuit for a wireless 100-electrode neural recording system. *IEEE J. Solid-State Circuits*, 42(1):123–133, Jan 2007.

[7] M. A. Lebedev and M. A. L. Nicolelis. Brain machine interfaces: past, present, and future. *Trends in Neurosciences*, 29(9):536–546, Sep. 2006.

[8] K. D. Wise, D.J. Anderson, J.F. Hetke, D.R. Kipke, and K. Najafi. Wireless implantable microsystems: High-density electronic interfaces to the nervous system. *Proc. of the IEEE*, 92(1):76–97, Jan. 2004.

[9] M. Rizk, C. A. Bossetti, T. A. Jochum, S. H. Callender, M. A. L. Nicolelis, D. A. Turner, and P. D. Wolf. A fully implantable 96-channel neural data acquisition system. *Journal of Neural Engineering*, 6, Mar. 2009.

[10] Greatbatch Inc. em able tech brief, 2007. Electronically available at: http://www.greatbatch.com/Medical/products.aspx.

[11] Quallion LLC, Dec. 2008. http://www.quallion.com/sub-tc-primary.asp.

[12] Greatbatch Inc., 2008. http://www.greatbatch.com/Medical/Secondary.aspx.

[13] Quallion LLC, 2009. http://www.quallion.com/sub-sp-main.asp.

[14] D. C. Jeutter. A transcutaneous implanted battery recharging and biotelemeter power switching system. *IEEE trans Biomedical Engineering*, BME-29(5):314–321, May 1982.

[15] P. Li and R. Bashirullah. A wireless power interface for rechargeable battery operated medical implants. *IEEEE Transactions on Circuits and Systems-II: Express Briefs*, 54(10):912–916, Oct. 2007.

[16] P. Horowitz and W. Hill. *The Art of Electronics*. Cambridge University Press, 2nd edition, 1989.

[17] W. Kester and J. Buxton. Practical design techniques for power and thermal management, section 5: Battery chargers. Analog Devices Technical Reference Book, 1998.

[18] D. Freeman and D. Heacock. Advanced charger designs address modern battery technologies. *WESCON/93*, Sept. 28-30.

[19] J. C. Schuder. Powering an artificial heart: Birth of the inductively coupled-radio frequency system in 1960. *Artificial Organs*, 26(11):909–915, 2002.

[20] J. C. Schuder, J. H. Gold, and H. E. Stephenson. An inductively coupled rf system for the transmission of 1 kw of powr through the skin. *IEEE trans. on Biomedical Engineering*, BME-18(4):265–273, Jul 1971.

[21] R. Puers and G. Vandervoorde. Recent progress on transcutaneous energy transfer for total artifical heart systems. *Aritificial Organs*, 25(5):400–405, 2001.

[22] G. Vandervoorde and R. Puers. Wireless energy transfer for stand-alone systems: a comparison between low and high power applicability. *Sensors and Actuators. A, Physical*, 92:305–311, 2001.

[23] A. Ghahary and B. H. Cho. Design of a transcutaneous energy transmission system using a series resonant converter. *IEEE Trans. on Power Electronics*, 7:261–269, Apr 1992.

[24] R. P. Phillips. A high capacity transcutaneous energy transfer system. *ASIAO Journal*, 41(3):M259–262, Jul-Sep 1995.

[25] T. Mussivand, J. A. Miller, P. J. Santerre, K. C. Rajagopalan G. Belanger, P. J. Hendry, R. G. Masters, R. Robichaud K. S. Holmes, M. Keaney, V. Walley, and W. J. Keon. Transcutaneous energy transfer system performance evaluation. *Artificial Organs*, 17(11):940–947, 1993.

[26] J. A. Miller, G. Belanger, and T. Mussivand. Development of an automated transcutaneous energy transfer system. *ASAIO Journal*, 39(3):m706–m710, Jul-Sep. 1993.

[27] W. J. Weiss, G. Rosenberg, A. J. Snyder, W. E. Pae, W. E. Richenbacher, and W. S. Pierce. In vivo performance of a transcutaneous energy transmission system with the penn state motor driven ventricular assist device. *ASAIO Trans*, 35(3):284–288, Jul-Sep 1989.

[28] W. J. Weiss, G. Rosenberg, A. J. Snyder, J. Donachy Sr, J. Reibson, O. Kawaguchi, J. S. Sapirstein, W. E. Pae, and W. S. Pierce. A completely implanted left ventricular assist device. *ASAIO Journal*, 39(3):M427–432, Jul-Sep. 1993.

[29] A. J. Snyder, G. Rosenberg, W. J Weiss, S. K. Ford, R. A. Nazarian, D. L. Hicks, J. A. Marlotte, O. Kawaguchi, G. A. Prophet, J. S. Sapirstein, M. Schwartz, and W. S. Pierce. In vivo testing of a completely implanted total artificial heart system. *ASAIO Journal*, 39(9):M177–189, jul-sep 1993.

[30] G. E. Loeb, R. A. Peck, W. H. Moore, and K. Hood. Bion system for distributed nerual prosthetic interfaces. *Medical Engineering and Physics*, 23(1):9–18, Jan. 2001.

[31] C.M. Zierhofer and E. S. Hochmair. Implementation of a telemetric-monitoring system in a cochlear implant. In *EMBS, Engineering Advances:New Opportunities for Biomedical Engineers. Proceedings of the 16th Annual International Conference of the IEEE*, volume 2, pages 910–911, Nov. 1994.

[32] C Liang, J.J Chen, C. Chung, C. Cheng, and C. Wang. An implantable bidirectional wireless transmission system for transcutaneous biological signal recording. *Physiol. Meas.*, 26(1):83–97, Feb. 2005.

[33] P. Irazoqui-Pastor, I. Mody, and J. W. Judy. Transcutaneous rf-powered neural recording devices. In *Proc. 2nd Joint EMBS/BMES Conf.*, pages 2105–2106, Oct. 2002. Houston.

[34] T. Akin, K. Najafi, and R. M. Bradley. A wireless implantable multichannel digital neural recording system for a micromachined sieve electrode. *IEEE Journal of Solid-State Circuits*, 33(1):109–118, Jan. 1998.

[35] M. Sawan, Y. Hu, and J Coulombe. Wireless smart implants dedicated to multihannel monitoring and microstimulation. *IEEE Circuits and Systems Magazine*, 5(1):21–39, 2005.

[36] G. Lazzi. Thermal effects of bioimplants. *IEEE Engineering in Medicine and Biology Magazine*, 24(5):75–81, Sep/Oct 2005.

[37] International Organization for Standardization. Implants for surgery - active implantable medical devices - part 1: General requirements for safety, marking, and for information to be provided by the manufacturer, 2000. ISO 14708-1.

[38] G. M. Saidel, C. R. Davies, E. H. Liu, and H. Harasaki. Temperature and perfusion responses of muscle and lung tissue during chronic heating in vivo. *Medical and Biological Engineering and Computing*, 39(1):126–133, Jan. 2001.

[39] C. R. Davies, F. Fukumura, K. Fukamachi, K. Muramoto, S. C. Himley, A. Massiello, J. Chen, and H. Harasaki. Adaptation of tissue to a chronic heat load. *ASIAO Journal*, 40(3):M514–517, Jul-Sep. 1994.

[40] E. H. Liu, G. M. Saidel, and H. Harasaki. Model analysis of tissue response to transient and chronic heating. *Annals of Biomedical Engineering*, 31(8):814–820, Nov. 2003.

[41] T. M. Seese, H Harasaki, G. M. Saidel, and Charles R. Davies. Characterization of tissue morphology, angiogenesis, and temperature in the adaptive response of muscle tissue to chronic heating. *Laboratory Investigation*, 78(12):1553–1562, Dec. 1998.

[42] Y. Okazaki, C. R. Davies, T. Matsuyoshi, K. Fukamachi, K. E. Wika, and H. Harasaki. Heat from an implanted power source is mainly dissipated by blood perfusion. *ASIAO Journal*, 43(5):M585–588, Sep-Oct 1997.

[43] D. B. Geselowitz, Q. T. N. Hoang, and R. P. Gaumond. The effects of metals on a transcutaneous energy transmission system. *IEEE Transactions on Biomedical Engineering*, 39(9):928–934, Sep. 1992.

[44] IEEE Standard for Safety Levels with Respect to Human Exposure to Radio Frequency Electromagnetic Fields, 3 kHz to 300 GHz, 2005. IEEE std C95.1.

[45] P. S. Ruggera, D. M. Witters, G. von Maltzahn, and H. I. Bassen. In vitro assessment of tissue heating near metallic medical implants by exposure to pulsed radio frequency diathermy. *Physics in Medicine and Biology*, 48(17):2919–2928, Sep. 2003.

[46] Q. Tang, N. Tummala, S. Kumar, and S. Gupta. Communication scheduling to minimize thermal effects of implanted biosensor networks in homogeneous tissue. *IEEE Trans. on Biomedical Engineering*, 52(7):1285–1294, Jul. 2005.

[47] E. Litvak, K.R. Foster, and M. H. Repacholi. Health and safety implications of exposure to electromagnetic fields in the frequency range 300 hz to 10 mhz. *Bioelectromagnetics*, 23(1):68–86, Jan. 2002.

[48] F. A. Duck. *Physical Properties of Tissue*. Academic Press, 1990. New York.

[49] Federal Communications Commission. Oet bulletin 56, 1999.

[50] N. O. Sokal and A. D. Sokal. Class E - a new class of high-efficiency tuned single-ended switching power amplifiers. *IEEE J. of Solid-State Circuits*, SC-10(3):168–176, Jun 1975.

[51] F. H. Raab. Idealized operation of the class E tuned power amplifier. *IEEE Transactions on Circuits and Systems*, cas-24(12):725–735, dec 1977.

[52] M. Catrysse, B. Hermans, and R. Puers. An inductive power system with integrated bi-directional data-transmission. *Sensors and Actuators A*, 115:221–229, Sept 2004.

[53] K. Van Schuylenbergh. *Optimisation of Inductive Powering of Small Biotelemetry Implants*. PhD thesis, Katholieke Universiteit Leuven, 1998.

[54] C. M. Zierhofer and E.S. Hochmair. High-efficiency coupling-insensitive transcutaneous power and data transmission via an inductive link. *IEEE Trans. on Biomedical Engineering*, 37(7):716–722, Jul 1990.

[55] G. A. Kendir, W. Liu, G. Wang, M. Sivaprakasam, R. Bashirullah, M. S. Humayun, and J. D. Weiland. An optimal design methodology for inductive power link with class E amplifier. *IEEE Transactions on Circuits and Systems*, 52(5):857–866, May 2005.

[56] G. Wang, W. Liu, M. Sivaprakasam, and G. A. Kendir. Design and analysis of an adaptive transcutaneous power telemetry for biomedical implants. *IEEE Transactions on Circuits and Systems*, 52(10):2109–2117, Oct 2005.

[57] B. Lenaerts and R. Puers. An inductive power link for a wireless endoscope. *Biosensors and Bioelectronics*, 22(7):1390–1395, Feb 2007.

[58] S. Atluri and M. Ghovanloo. Design of a wideband power efficient inductive wireless link for implantable biomedical devices using multiple carriers. In *Proc. of the 2nd International IEEE EMBS, Conference on Neural Engineering*, pages 533–537, mar. 2005. Arlington.

[59] D. C. Galbraith, M. Soma, and R. L. White. A wide-band efficient inductive transdermal power and data link with couplig insensitive gain. *IEEE Trans on Biomedical Engineering*, 34(4):265–275, Apr. 1987.

[60] M. Soma, D. C. Galbraith, and R. L. White. Radio-frequency coils in implantable devices: misalignment analysis and design procedure. *IEEE Trans on Biomedical Engineering*, 34(4):276–282, Apr. 1987.

[61] G. B. Joung and B. H. Cho. An energy transmission system for an artificial heart using leakage inductance compensation of transcutaneous transformer. *IEEE Trans. on Power Electronics*, 13:1013–1022, Nov. 1998.

[62] H. Matsuki, Y. Yamakata, and N. Chubachi. Transcutaneous dc-dc converter for totally implantable artificial heart using synchronous rectifier. *IEEE trans. on Magnetics*, 32(5):5118–5120, 1996.

[63] M. Rizk, I. Obeid, S. H. Callender, and P. D. Wolf. A single-chip signal processing and telemetry engine for an implantable 96-channel neural data acquisition system. *Journal of Neural Engineering*, 4(3):309–321, Jul. 2007.

[64] D. A. Grant and J. Gowar. *Power MOSFETs: Theory and Applications*. Wiley, 1989. New York.

[65] National Semiconductor. Introduction to power supplies. Appliction Note AN-556, Sept 2002.

[66] E. R. Hnatek. *Design of Solid-State Power Supplies*. Van Nostrand Reinhold, 2nd edition, 1981. New York.

[67] M. Ghovanloo and K. Najafi. Fully integrated wideband high-current rectifiers for inductively powered devices. *IEEE Journal of Solid-State Circuits*, 39(11):1976–1984, Nov. 2004.

[68] M. Ghovanloo and Najafi K. A modular 32-site wireless neural stimulation microsystem. *IEEE Journal of Solid-State Circuits*, 39(12):2457–2466, Dec. 2004.

[69] M. H. Rashid. *Power Electronics: Circuits, Devices, and Applications*. Prentice Hall, 1998. New Jersey.

[70] G. C. Chryssis. *High-Frequency Switching Power Supplies: Theory and Design*. McGraw-Hill, 2nd edition, 1989. New York.

[71] C. M. Zierhofer and E.S. Hochmair. Geometric approach for coupling enhancment of magnetically coupled coils. *IEEE Trans. on Biomedical Engineering*, 43(7):708–714, Jul 1996.

[72] J. M. Ahn, D. W. Kang, H. C. Kim, and B. G. Min. In vivo performance evaluaion of a transcutaneous energy and information transmission system for the total artificial heart. *American Society for Artificial Internal Organs Journal*, 39(3):M208–M212, 1993.

[73] H. L. Chan, K. W. E. Cheng, and D. Sutanto. A simplified neumann's formula for calculation of inductance of spiral coil. In *IEE, Power Electronics and Variable Speed Drives*, number 475, pages 69–73, Sep. 2000.

[74] S. Babic and C. Akyel. Improvement in calculation of the self- and mutual inductance of thin- wall solenoids and disk coils. *IEEE Trans on Magnetics*, 36(4):1970–1975, Jul. 2000.

[75] W. G. Hurley and M. C. Duffy. Calculation of self and mutual impedances in planar magnetic structures. *IEEE Trans. on Magnetics*, 31(4):2416–2422, Jul. 1995.

[76] F. W. Grover. *Inductance Calculations*. Dover Publications, Inc., 1946. New York.

[77] W. J. Sarjeant, I. W. Clelland, and R. A. Price. Capacitive components for poer electronics. *Proceedings of the IEEE*, 89(6):846–855, Jun. 2001.

[78] I. W. Clelland and R. A. Price. Polymer film capacitors deliver proven stability. *Power Electronics Technology*, pages 16–24, May 2005.

[79] C. Fernandez, O. Garcia, R. Prieto, J. A. Cobos, S. Gabriels, and G. V. D. Borght. Design issues of a coreless transformer for a contact-less application. In *17th Annual IEEE Applied Power Electronics Conference and Exposition (APEC)*, volume 1, pages 426–432, Mar. 2002.

[80] J. A. Sabate, V. Vlatkovic, R. B. Ridley, F. C. Lee, and B. H. Cho. Design considerations for high-voltage high-power full-bridge zero-voltage-switched pwm converters. In *5th Annual IEEE Applied Power Electronics Conference and Exposition (APEC)*, pages 275–284, Mar. 1990.

[81] D. B. Dalal. A 500 khz multi-output converter with zero voltage switching. In *5th Annual IEEE Applied Power Electronics Conference and Exposition (APEC)*, pages 265–274, Mar. 1990.

[82] Federal Communications Commission. Oet bulletin 65, 1997.

[83] D. H. Werner. An exact integration procedure for vector potentials of thin loop antennas. *IEEE Transactions on Antennas and Propagation*, 44(2):157–165, Feb. 1996.

[84] W. R. Smythe. *Static and Dynamic electricity*. McGraw-Hill, 3rd edition, 1968. New York.

[85] C. A. Balanis. *Antenna Theory: Analysis and Design*. Wiley, 3rd. edition, 2005. New York.

[86] P. L. Overfelt. Near fields of the constant current thin circular loop antenna of arbitrary radius. *IEEE Transactions on Antennas and Propagation*, 44(2):166–171, Feb. 1996.

[87] C. Gabriel, S. Gabriel, and E. Corthout. The dielectric properties of biological tissues: I. literature survey. *Phycis in Medicine and Biology*, 41(11):2231–2249, Nov. 1996.

[88] S. Gabriel, R. W. Lau, and C. Gabriel. The dielectric properties of biological tissues: Ii. measurements in the frequency range 10 hz to 20 ghz. *Phycis in Medicine and Biology*, 41(11):2251–2269, Nov. 1996.

[89] S. Gabriel, R. W. Lau, and C. Gabriel. The dielectric properties of biological tissues: Iii. parametric models for the dielectric spectrum of tissues. *Phycis in Medicine and Biology*, 41(11):2271–2293, Nov. 1996.

[90] C. Gabriel and S. Gabriel. *Compilation of the Dielectric Properties of Body Tissues at RF and Microwave Frequencies*. http://niremf.ifac.cnr.it/docs/DIELECTRIC/Title.html.

[91] John G. Webster, editor. *Medical Instrumentation*. Wiley, 2nd edition, 1995. New York.

[92] P. R. N. Childs. *Practical Temperature Measurements*. Butterworth-Heinemann, 2001. Boston.

[93] D. S. Campbell and J.A. Hayes. *Capacitive and Resistive Electronic Components*, volume 8 of *Electrocomponent Science Monographs*. Gordon and Breach Science Publishers, 1994.

[94] Thermometrics Inc. *PTC Thermistors*. Available online at: http://www.thermometrics.com/htmldocs/proserv.htm.

[95] Thermometrics, Inc. *NTC Thermistors*. Available online at: http://www.thermometrics.com/htmldocs/proserv.htm.

[96] John G. Webster, editor. *Medical Instrumentation*. Wiley, 3nd edition, 1998. New York.

[97] S. Biyikli, M. F. Modest, and R. Tarr. Measurements of thermal properties for human femora. *Journal of Biomedical Materials Research*, 20(9):1335–1345, Nov.-Dec. 1986.

[98] R. Clattenburg, J. Cohen, S. Conner, and N. Cook. Thermal properties of cancellous bone. *Journal of Biomedical Materials Research*, 9:169–182, Mar 1975.

[99] R. D. Miller, editor. *Miller's Anesthesia*. Elsevier Churchill Livingstone, 6th edition, 2005. Philadelphia.

[100] W. H. Ko, S. P. Liang, and C. D. F. Fung. Design of radio-frequency powered coils for implant instruments. *Medical & Biological Engineering & Computing*, 15:634–640, Nov 1977.

Biography

Chad Bossetti was born in December, 1975, in Columbus, Ohio. He received the Bachelor of Science degree in Electrical and Computer Engineering from the University of Colorado, Colorado Springs. He graduated with special honors in 2002. He completed his Ph.D. at Duke University in March, 2009. His research interests include transcutaneous energy transfer, field potential modeling in tissue, and implanted neural recording and stimulation systems.

Publications

Peer-Reviewed Journal Publications

M. Rizk, C.A. Bossetti, T.A. Jochum, S.H. Callender, M.A.L. Nicolelis, D.A. Turner, P.D. Wolf, "A fully implantable 96-channel neural data acquisition system." *Journal of Neural Engineering*, vol. 6, Jun. 2009. accepted for publication.

C.A. Bossetti, M.J. Birdno, W.M. Grill, "Analysis of the quasi-static approximation for calculating potentials generated by neural stimulation." *Journal of Neural Engineering*, vol. 5, no. 1, pp. 44-53, Mar. 2008.

C.A. Bossetti, J.M. Carmena, M.A.L. Nicolelis, P.D. Wolf, "Transmission Latencies in a Telemetry-Linked, Brain-Machine Interface." *IEEE Transactions on Biomedical Engineering*, vol. 51, no. 6, pp. 919-924, Jun. 2004.

Conference Papers/Abstracts

M.J. Birdno, C.A. Bossetti, W.M. Grill, "Validity of the quasi-static assumption for calculating potentials generated in neural stimulation." Neural Interfaces Workshop, National Institute of Neurological Disorders and Stroke, Bethesda, MD, Aug 2006.

C.A. Bossetti, T.A. Jochum, S.H. Callender, P.D. Wolf, "A transcutaneous energy transfer system for brain-machine interface applications." Biomedical Engineering Society, Baltimore, MD, Oct 2005.

P.D. Wolf, M.A.L. Nicolelis, C.A. Bossetti, S.H. Callender, M. Rizk, T.A. Jochum, "Design and Implementation of the Electronics for a 96 Channel Implanted Brain-Machine Interface." Neural Interfaces Workshop. Sep. 2005. Bethesda, MD.

J. Morizio, D.S. Won, I. Obeid, C.A. Bossetti, M.A.L. Nicolelis, P.D. Wolf, "16-Channel neural pre-conditioner device," 1st Int IEEE BMES Conf on Neural Engineering. Capri Island, Italy. Mar 2003.